



HAL
open science

Compact binaries : models of populations, multi-messenger detection and cosmology

Duncan Meacher

► **To cite this version:**

Duncan Meacher. Compact binaries : models of populations, multi-messenger detection and cosmology. Other. Université Nice Sophia Antipolis, 2015. English. NNT : 2015NICE4058 . tel-01243679

HAL Id: tel-01243679

<https://theses.hal.science/tel-01243679>

Submitted on 15 Dec 2015

HAL is a multi-disciplinary open access archive for the deposit and dissemination of scientific research documents, whether they are published or not. The documents may come from teaching and research institutions in France or abroad, or from public or private research centers.

L'archive ouverte pluridisciplinaire **HAL**, est destinée au dépôt et à la diffusion de documents scientifiques de niveau recherche, publiés ou non, émanant des établissements d'enseignement et de recherche français ou étrangers, des laboratoires publics ou privés.

UNIVERSITE DE NICE-SOPHIA ANTIPOLIS
UFR SCIENCES
ÉCOLE DOCTORALE DES SCIENCES FONDAMENTALES
ET APPLIQUÉES

THESE

pour obtenir le titre de
Docteur en Sciences
de l'UNIVERSITE de Nice-Sophia Antipolis

Discipline: Relativistic Astrophysics

présentée et soutenue par
AUTEUR: Duncan MEACHER

**Compact Binaries: Models of
Populations, Multi-Messenger Detection
and Cosmology**

Thèse dirigée par: Tania REGIMBAU
soutenue le 8th September 2015 à l'Observatoire de la Côte d'Azur

Jury:

Michel Boër
Nelson Christensen
Albert Lazzarini
Samaya Nissanke
Tania Regimbau
Dorota Rosinska
B. S. Sathyaprakash
Chris Van Den Broeck

Fonction:

Examineur
Examineur
Rapporteur
Examineur
Directeur de thèse
Examineur
Examineur
Rapporteur

UNIVERSITE OF NICE-SOPHIA ANTIPOLIS

UFR SCIENCES
DOCTORAL SCHOOL OF BASIC AND APPLIED
SCIENCES

THESIS

to obtain the title of
Doctor of Science
of the UNIVERSITE of Nice-Sophia Antipolis

Discipline: Relativistic Astrophysics

presented and supported by
AUTHOR: Duncan MEACHER

Compact Binaries: Models of Populations, Multi-Messenger Detection and Cosmology

Thesis supervisor: Tania REGIMBAU
presented 8th September 2015 at the Observatoire de la Côte d'Azur

Defence committee:

Michel Boër
Nelson Christensen
Albert Lazzarini
Samaya Nissanke
Tania Regimbau
Dorota Rosinska
B. S. Sathyaprakash
Chris Van Den Broeck

Position:

Examiner
Examiner
Referee
Examiner
Thesis Supervisor
Examiner
Examiner
Referee

“There is something profoundly cynical, my friends, in the notion of paradise after death. The lure is evasion. The promise is excusative. One need not accept responsibility for the world as it is, and by extension, one need do nothing about it. To strive for change, for true goodness in this mortal world, one must acknowledge and accept, within one’s own soul, that this mortal reality has purpose in itself, that its greatest value is not for us, but for our children and their children. To view life as but a quick passage along a foul, tortured path – made foul and tortured by our own indifference – is to excuse all manner of misery and depravity, and to exact cruel punishment upon the innocent lives to come.

I defy this notion of paradise beyond the gates of bone. If the soul truly survives the passage, then it behooves us – each of us, my friends – to nurture a faith in similitude: what awaits us is a reflection of what we leave behind, and in the squandering of our mortal existence, we surrender the opportunity to learn the ways of goodness, the practice of sympathy, empathy, compassion and healing – all passed by in our rush to arrive at a place of glory and beauty, a place we did not earn, and most certainly do not deserve.”

Steven Erikson, *The Malazan Book of the Fallen*

UNIVERSITY OF NICE - SOPHIA-ANTIPOLIS

Abstract

UFR Sciences

Doctoral School of Basic and Applied Sciences

Doctor of Science

Compact Binaries: Models of Populations, Multi-Messenger Detection and Cosmology

by Duncan MEACHER

Here I present my thesis investigating gravitational-wave data analysis in the following two areas. The first is to test the readiness of the LIGO-Virgo collaborations to the advanced detector era, which will begin in the summer of 2015, to make a detection of an astrophysical stochastic gravitational-wave background. The second is to continue an investigation into the science potential of a conceived, third generation gravitational-wave detector, the Einstein Telescope, in terms of astrophysics and cosmology. Both of these are conducted with the use of mock data and science challenges which consists of the production of expected gravitational-wave detector data, containing a large number of sources, that are simulated using realistic distributions. For the advanced gravitational-wave detectors I find that expected stochastic gravitational-wave signal, originating from a discrete set of astrophysical sources, should not differ from that of an isotropic Gaussian signal by both analytical derivation and through the analysis of mock data sets. An astrophysical gravitational-wave background signal should be detectable by the advanced detectors within the first few years of operations, given a large enough rate of compact binary coalescence events. For the Einstein Telescope I was able to perform a full mock data and science challenge where the data was first generated and then analysed with a new, low-latency matched filtering pipeline called `gstlal` to test the use of different low frequency cut-offs and to detect a population of binary neutron stars. I also present the results from an analysis of the mock data set with an isotropic cross-correlation pipeline to make a measurement of the astrophysical gravitational-wave background. Due to the sensitivity of the Einstein Telescope, the assumed isotropy of the background signal is broken and needs to be corrected for by considering the analytical derivation mentioned above. Finally I present work on estimations of the expected rate of coincident detections between gravitational waves and short gamma ray bursts with advanced and future generation detectors and use the results to develop a method for estimating the size of the beaming angle of sGRBs.

Acknowledgements

There are many people who I would like to thank for their continued help and encouragement during the course of my post-graduate studies.

I would firstly like to thank my thesis supervisor, Tania Regimbau, for her valued guidance and support throughout all my studies. She has allowed and encouraged me to seek out my own research interests whilst still helping with her expertise when needed. I hope to be able to continue working with her for many years to come.

Secondly I would like to thank all my unofficial supervisors, B. S. Sathyaprakash, Eric Thrane, Nelson Christensen, Samaya Nissanke, Walter Del Pozzo, Chad Hanna, and Kipp Cannon, who have all treated me as one of their own students for some of my many projects that I have undertaken. I have enjoyed working with each of you and value the knowledge and experience I gained in many different areas.

I want to thank all my collaborators from various papers, Michael Coughlin, Sean Morris, Shivraj Kandhasamy, Vuk Mandic, Joe D. Romano, John Veitch, Salvatore Vitale, Karelle Siellez, Bruce Gendre, and Michel Boër, for the help you have given. Whether that has been from contributing to the research and papers, useful discussions, or proofreading the manuscripts, it has all been invaluable assistance.

I would also like to thank other people for useful discussions, Thomas Adams, Thomas Dent, Steven Fairhurst, Maxime Fays, Kari Hodge, Paul Hopkins, Sebastian Khan, Io Kleiser, Tjonnie Li, Ilya Mandel, Valeriu Predoi, Michael Pürrer, Patrick Sutton, Chris Van Den Broeck, Li-Wei Wei, Alan Weinstein, Andrew Williamson, and Aaron Zimmerman. I have enjoyed each of the discussions we had on many different topics.

I thank Catherine Nary Man, director of ARTEMIS laboratory and Farrokh Vakili, director of Côte d'Azur Observatory, as well as to the secretaries of ARTEMIS, Seynabou Ndiaye and David Andrieux for their help and assistance during the course of my studies.

I also thank Caltech and the LIGO laboratory and Cardiff university for financial support in order to be able to go and work at their institutes. Also to Bruce Allen and the Albert Einstein Institute in Hannover, supported by the Max-Planck-Gesellschaft, for use of the Atlas high-performance computing cluster, with which I have logged over 500,000 CPU hours, and Carsten Aulbert for technical advice and assistance.

Also to Howard Shore, for your masterful composition of the *Lord of the Rings* soundtrack, which has kept me working through many hours of coding and writing.

Finally I want to Marion, who's love, support, and understanding in this last year has helped me through, especially after long hours and weekend spent in the office. Also to my friends and family around the world, who I don't get to see or visit as often as I'd like.

Duncan Meacher acknowledges the PhD financial support from the Observatoire de la Côte d'Azur and the PACA region.

Contents

Abstract	ii
Acknowledgements	iii
Contents	iv
List of Figures	vii
List of Tables	ix
1 Introduction	1
1.1 Motivation	2
1.2 Thesis Organisation	3
2 Background Information	4
2.1 Gravitational Waves	4
2.2 Sources of GWs	5
2.2.1 Compact binary coalescence	5
2.2.2 Burst	6
2.2.3 Stochastic	7
2.2.4 Continuous	7
2.3 GW Detectors	8
2.4 Data Analysis	9
2.4.1 Matched Filtering	10
2.4.2 Cross-correlation	11
2.5 Summary and Conclusion	12
3 Statistical Properties of Astrophysical Gravitational-Wave Backgrounds	14
3.1 Introduction	14
3.2 Formalism	15
3.2.1 Cross-correlation searches for a stochastic background	15
3.2.2 Average over realisations of a stochastic background	18
3.2.3 Individual realisations of a stochastic background for compact binary coalescence	20
3.3 Numerical testing	22
3.3.1 Simulation	22
3.3.2 Bias	24
3.4 Conclusions	27

4	A Mock Data and Science Challenge for Detecting an Astrophysical Stochastic Gravitational-Wave Background with Advanced LIGO and Advanced Virgo	28
4.1	Introduction	28
4.2	Mock Data	29
4.2.1	Mock Data Generation	30
4.2.1.1	Simulation of GW CBC signals	30
4.2.1.2	Simulation of Gaussian noise	34
4.2.1.3	Re-coloured noise	34
4.2.2	Mock Data Sets	35
4.2.2.1	Main data sets	35
4.2.2.2	Observing scenario	36
4.2.3	Astrophysical stochastic background from CBC	37
4.3	SGWB Search	39
4.4	Parameter Estimation	41
4.4.1	SGWB Models	42
4.5	Results	42
4.5.1	Gaussian	44
4.5.2	Re-coloured	44
4.5.3	Observing Scenario	45
4.5.4	Parameter Estimation	46
4.6	Conclusion	46
5	Second Einstein Telescope Mock Data and Science Challenge: Compact Binary Coalescence Data Analysis	49
5.1	Introduction	49
5.2	Mock Data	51
5.2.1	Simulation of the Noise	51
5.2.2	Simulation of the GW signals from BNS	52
5.3	Analysis	54
5.3.1	Analysis stages	55
5.3.2	Searches	57
5.4	Results	57
5.4.1	gstlal analysis: Impact of the lower frequency cut-off on detection efficiency	58
5.4.2	Detection efficiency	59
5.4.3	Rate estimation	61
5.4.4	Impact of lower frequency cut-off on parameter estimation	61
5.4.4.1	Coalescence time	62
5.4.4.2	Masses	62
5.5	Future Development	65
5.6	Conclusion	65
6	Second Einstein Telescope Mock Data and Science Challenge: Detection of the GW Stochastic Background from Compact Binary Coalescences	67
6.1	Introduction	67
6.2	The second ET mock data	69
6.2.1	Simulation of the Noise	69
6.2.2	Simulation of the GW signal from CBC	69
6.3	Spectral properties	71
6.4	Stochastic Analysis	73
6.5	Conclusion	76
7	Revisiting coincidence rate between Gravitational Wave detection and short Gamma-Ray Burst for the Advanced and third generation	77

7.1	Sec:C9Introduction	77
7.2	Monte-Carlo simulations	79
7.2.1	Simulation of a population of BNS or NS-BH	79
7.2.2	GW selection effects	80
7.2.3	EM selection effects	81
	7.2.3.1 The beaming angle	81
	7.2.3.2 Instrumental effects	82
7.3	Detection efficiency	83
7.3.1	GW efficiency	83
7.3.2	Coincidence efficiency: the case of a perfect GRB detector	83
7.3.3	Case of a realistic GRB detector	84
7.4	Rate	85
7.4.1	Detection rates	87
7.5	Constraints on the beaming angle	88
7.6	Conclusion	89
8	Conclusion	101
A	Einstein Telescope pre-site selection detector locations technical document	103
A.1	Introduction	103
A.2	Detector locations	103
A.2.1	Results	106
A.3	Null stream	106
	Bibliography	109

List of Figures

2.1	Inspiral waveform	6
2.2	Burst waveform	7
2.3	Stochastic signal	8
2.4	Continuous waveform	8
2.5	Diagram of interferometer	10
2.6	Detector sensitivity curves	12
3.1	Discrete overlap reduction function	23
3.2	Realisations of a discrete ORF	25
3.3	Fractional bias from discrete ORF	26
4.1	Redshift probability distribution	31
4.2	Advanced detector sensitivity curves	31
4.3	Signal time series output	38
4.4	Astrophysical energy density spectrum. SNR build up	40
4.5	Gaussian and re-coloured noise data set 4 results	45
4.6	Observing scenario results	46
4.7	Parameter estimation results	47
5.1	Detector sensitivity cures. Source redshift distribution	52
5.2	Injected mass distributions	55
5.3	Impact of the lower frequency cut-off BNS triggers/detections	60
5.4	Detection efficiency/Rate estimation	62
5.5	Error in coalescence time	63
5.6	Impact of lower frequency cut-off on BNS mass measurements	64
6.1	ET sensitivity curves	70
6.2	Astrophysical energy density spectrum	72
6.3	θ efficiency	75
6.4	Contribution to SNR	76
7.1	Flowchart	92
7.2	Redshift probability distribution	93
7.3	Detector sensitivity curves	94
7.4	<i>Swift</i> sensitivity	95
7.5	GW Detection efficiency	95
7.6	Coincident detection efficiency	96
7.7	Ratio of observed sGRBs	96
7.8	<i>Swift</i> detection efficiency	97
7.9	GW/GRB detection efficiency	98
7.10	Cosmic star formation rates	99
7.11	Beaming angle estimation	100

A.1 ET detector configuration	104
A.2 ET detector locations (Cartesian coordinates)	107

List of Tables

3.1	Rate of BNS coalescence	23
4.1	List of mock data sets	37
4.2	Rate of BNS and BBH coalescence	37
4.3	Analysis results	43
4.4	Parameter estimation results	47
5.1	Search parameters	56
5.2	Search results	58
5.3	Distribution in error measurements	64
7.1	GRB detector properties	91
7.2	Coincident detection rate	91
7.3	Coincident detection rate: Perfect detectors	91
7.4	Beaming angle estimates	91
A.1	ET detector locations	106
A.2	ET <i>null stream</i> location	107

To my nephews, Jacob and Benjamin.

Chapter 1

Introduction

It began when the proverbial apple fell on Sir Isaac Newton's head, who first theorised the notion of gravity by deriving the inverse square law [1]. In his lifetime he was able to go on and fully develop the Newtonian theory of gravity, which included derivations of Kepler's three laws of planetary motion [2, 3]. This theory stated that two bodies felt a force of attraction to each other, proportional to mass of the two objects divided by the square of the distance between them. From this, one was able to model the orbital motion of all the known planets, even predicting the existence of the, then unknown, planet Neptune, from the unaccounted for motions of Uranus. Newton's theory was considered to be a valid description of gravity for over 200 years, until it was discovered that the orbit of the inner most planet, Mercury, couldn't be accounted for. For this a new theory of gravity needed to be derived.

By 1915 Albert Einstein was able to develop his theory of general relativity (GR) [4, 5]. With this he was able to precisely determine the orbital motion of Mercury [6] by introduction of the post-Newtonian expansions. The general theory of relativity replaced the idea that two bodies exert an attractive force on each by stipulating that space and time are connected as a single, four dimensional, *space-time*. When mass is present within this space-time it becomes deformed, and it is this curvature of space-time that causes the two bodies to orbit each other. One of the many improvements of GR over Newtonian theory was the inclusion of the time component. This meant that any deviation in the gradient of the space-time curvature propagated away, at a finite speed, from the source. This propagation of the deviation, or "ripples", in space-time was then described as *gravitational waves* [7].

Exactly 100 years after the discovery of general relativity, the hunt for Einstein's gravitational waves (GWs) continues. There have not yet been any direct measurements of GWs, though in 1975, R. Hulse and J. Taylor discovered the binary pulsar PSR B1913+16 [8], which was later found to have a decay in its orbital period that is perfectly described by the emission of GWs [9]. For this discovery, Hulse and Taylor won the 1993 Nobel Prize in Physics. The search for a direct detection began over 40 years after the development of GR, when J. Weber first developed the resonant (Weber) bar detector [10], though these instruments were nowhere near sensitive enough to be able to make a detection of GWs. The initial generation of gravitational-wave interferometer detectors, the U.S. LIGO (2002 - 2010) [11], the French/Italian Virgo (2007 -

2011) [12], the British/German GEO600 (1995 - present) [13], and Japanese TAMA (1995 - 2003) [14], were able to reach an unprecedented levels of sensitivity, with the best reaching a strain sensitivity of $\sim 1 \times 10^{-21}$.

The LIGO and Virgo detectors have recently undergone an upgrade into the second generation of detectors, advanced LIGO (aLIGO) [15] and Virgo (AdVirgo) [16], with the aLIGO detectors beginning operations the summer of 2015 and AdVirgo expected to join in the spring of 2016. It is hoped that the first direct detection of a GW will be made within the first few years following a series of continuous upgrades until the detectors reach their final design sensitivities, which is expected to be a order of magnitude more sensitive than the initial detectors. Much in the same way as observations in radio, infra-red, microwave, x-ray, and γ -ray wavelengths, over the last 60 years, allowed us to observe many unknown processes that were invisible at optical wavelengths, the direct detection of GWs will open up a whole new window to the universe.

A third generation gravitational-wave interferometer detector, the Einstein Telescope (ET) [17], is currently in the planning stage. This is envisioned to be an order of magnitude more sensitive than the second generation detectors, which will results in a large number of detections of GW signals from a wide variety of sources covering a large range of the star formation history and even possibly exploring GW signals of cosmological origins. This will allow us to probe into black holes, measure the equation of state or neutron stars, determine the mechanisms at the centre of core collapse supernovae, and answer many questions in physics, astrophysics and cosmology.

1.1 Motivation

The motivation for my thesis is to help test and develop the data analysis techniques that will be used to make detections of gravitational waves with the advanced and future generations of gravitational-wave detectors. This involves the use of a mock data generation program that was originally developed for the first ET mock data and science challenge [18], which is able to simulate the expected detector output time series that includes a large number of GW signals from a variety of sources, using realistic distributions. Having data that contains GW signals that cover the whole star formation history is the ideal tool to investigate the detection of an astrophysical stochastic gravitational-wave background (SGWB) as well as the individual detections of signals with the advanced detectors and the Einstein Telescope.

My thesis focuses on these two areas of data analysis, though I also investigate different areas, such as the application of GW detections to make measurements of cosmological parameters or the estimation of the rates of coincident detections between GWs and short gamma ray bursts, the progenitor of which is believed to be the coalescence of two spiralling compact objects. The aim of this is to first test our ability to be able to make detections of the respective signal, and then how best to interpret these results. The tests are important, firstly as part of the verification process for LIGO and Virgo when a SGWB is eventually observed, and secondly to prove the science potential that would be available to a third generation GW detector such as ET.

1.2 Thesis Organisation

Here I detail the structure and organisation of my thesis. In Chapter 2 I give an introduction to the general background theory of the material covered in this thesis, giving a brief overview of the theory of gravitational waves, the detectors we use to make detections, the sources of GWs, and finally the data analysis techniques used to extract the signals from the data. In Chapter 3 I present my work on an investigation on the statistical properties of astrophysical gravitational-wave backgrounds. Here we derive and show the expected variance in the stochastic gravitational-wave background signal by considering many realisations of a population of binary neutron stars. In Chapter 4 I present my work on a Mock Data and Science Challenge for Detecting an Astrophysical Stochastic Gravitational-Wave Background with Advanced LIGO and Advanced Virgo. Here we present multiple mock data sets that are used to test the current data analysis pipeline, along with the results which verify the findings of the previous chapter. In Chapter 5 I present my work on the Second Einstein Telescope Mock Data and Science Challenge: Low frequency Binary Neutron Star Data Analysis. We show the results from applying a low latency analysis pipeline to the expected signal dominant data from ET. This produces a number of detections, from which we are able to determine the detection efficiency and make an estimating on the rate of coalescent events as well as investigating the parameter recovery accuracy. In Chapter 6 I present my work on the Second Einstein Telescope Mock Data and Science Challenge: Detection of the GW Stochastic Background from Compact Binary Coalescences. We again test a data analysis pipeline with ET data, which breaks the assumption that the signal will be isotropic, and apply the finding from Chapter 3. In Chapter 7 I present my work on revisiting coincidence rate between Gravitational Wave detection and short Gamma-Ray Burst for the Advanced and third generation. Here we consider the case were we obtain a coincident electromagnetic counterpart to a GW detection and try to estimation the expected rates for second and third generation detectors. Finally, in Chapter 8 I give a conclusion to all the work that has been presented here.

Chapter 2

Background Information

2.1 Gravitational Waves

For a full review on the material covered in this chapter see the standard texts that go into great depths for both general relativity and gravitational waves [19–26]. The curvature of space-time can be explained by considering the Einstein field equation

$$G_{\alpha\beta} \equiv R_{\alpha\beta} - \frac{1}{2}g_{\alpha\beta}R + \Lambda g_{\alpha\beta} = \frac{8\pi G}{c^4}T_{\alpha\beta}, \quad (2.1)$$

where $G_{\alpha\beta}$ is the curvature tensor, G is the gravitational constant, c is the speed of light in a vacuum, $R_{\alpha\beta}$ is the Ricci tensor, $g_{\alpha\beta}$ is the metric tensor, Λ is the cosmological constant, $T_{\alpha\beta}$ is the stress–energy tensor and R is the scalar curvature. Here the left-hand side of the equation represents the spacial curvature, and the right-hand side represents the energy/matter content of space-time. Einstein’s theory of general relativity describes how space-time is distorted in the presence of mass. Gravitational waves are fluctuations or “ripples” in space-time that are predicted in Einstein’s theory of general relativity. Potentially measurable fluctuations are caused by having very large masses accelerated, like when two dense objects, such as black holes and neutron stars, are orbiting about each other in a binary system, which causes the curvature of space-time to oscillate in response to these masses. If a GW is treated as a linearised perturbation in flat space then it obeys the following wave equation

$$\left(\nabla^2 - \frac{1}{c^2}\frac{\partial^2}{\partial t^2}\right)h_{\alpha\beta} = -\frac{16\pi G}{c^4}T_{\alpha\beta}. \quad (2.2)$$

Here the wave operator acts on the perturbation, $h_{\alpha\beta}$, representing the GW, and the stress energy tensor, $T_{\alpha\beta}$, only contains information about the sources energy and mass density. It is also shown in this equation that GWs propagate through space at the speed of light. The indices, α and β , of the four dimensional tensors and vectors run from 0 to 3, where 0 represents the time component and 1,2 and 3 represent the three spacial dimensions. $h_{\alpha\beta}$ is thus defined as

$$h_{\alpha\beta} = \begin{pmatrix} 0 & 0 & 0 & 0 \\ 0 & h_+ & h_\times & 0 \\ 0 & h_\times & -h_+ & 0 \\ 0 & 0 & 0 & 0 \end{pmatrix}, \quad (2.3)$$

which results in two independent polarisations, h_+ (plus) and h_\times (cross) that are arranged at 45° to each other. The affect of a GW, travelling in the z direction, will cause the distance between two points in the $x - y$ plane to osculate, as it contracts and expands at a rate equal to the GW frequency. A GW consisting of just h_+ polarisation, aligned with the $x - y$ axis, will cause a displacement along these axis. The same GW consisting of just h_\times polarisation will have the same displacement at an angle of 45° to the axis.

2.2 Sources of GWs

There are many sources of GWs that cover a large range of frequencies and amplitudes, though only those originating from the most massive sources with relatively high frequencies ($f > 10\text{Hz}$) have a chance of being detected by terrestrial detectors. These sources are divided into four main groups, which are listed here in order of likelihood of detectability:

2.2.1 Compact binary coalescence

The coalescence of two compact objects, with masses m_1 and m_2 , such as binary neutron star (BNS), neutron star-black hole (NSBH), or binary black holes (BBH), are expected to be the most common GW signal that we will observe. These are formed when two massive stars in a binary system each undergo core collapse supernovae at the end of their main sequence lives to form either a neutron star or black hole. If the “kick” that each receives from the supernova explosion of the other isn’t enough for it to be ejected then these objects remain orbiting each other. Energy is radiated away from the system in the form of gravitational waves which results in the decrease of the separation between the two objects by

$$\frac{dE}{dt} = \frac{32G^4\nu^2M^3}{5c^5a^5}f(e), \quad (2.4)$$

where $M = m_1 + m_2$ is the total mass, $\nu = m_1m_2/M$ is the reduced mass, a is the semi-major axis, and

$$f(e) = \frac{1}{(1 - e^2)^{7/2}} \left(1 + \frac{73}{24}e^3 + \frac{37}{96}e^4 \right), \quad (2.5)$$

is a correction factor for a non circular orbit with eccentricity e .

Due to the conservation of angular momentum this decrease in the distance between them causes their angular velocity, and thus orbital frequency to increase. The rate of the change in

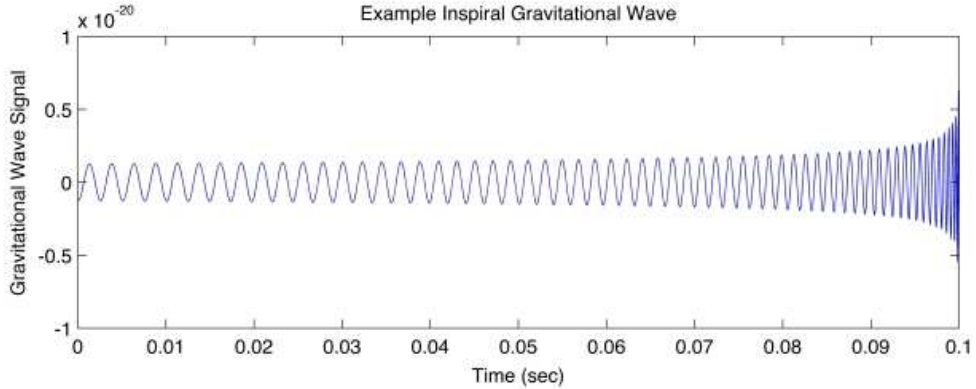


FIGURE 2.1: Example of an inspiral waveform [27]. The chirping signal, produced from the inspiral of two compact objects, is clearly seen with both the frequency and amplitude increasing until the f_{lsc0} .

frequency is $\dot{f} \propto f^{11/3}$, where the emitted GW frequency, f , is twice that of the orbital frequency. As the separation decreases, dE/dt increases, which produces a chirping waveform, see Fig. 2.1. This continues up until the point of the last stable circular orbit, given by

$$f_{\text{lsc0}} = \frac{c^3}{6^{3/2}\pi GM}, \quad (2.6)$$

at which point the two objects plunge into each other. For BNS it is enough to consider the waveform up to this point using the post-Newtonian approximation but for NSBH and BBH we also consider the merger and ringdown of the waveform which are calculated with the use of numerical relativity.

2.2.2 Burst

Burst GWs originate from short-duration sources. The progenitors for these types of signals are events that coincide with bright, high energy, electromagnetic counterparts, such as extra-galactic gamma ray bursts (GRBs), both long and short, or galactic supernova. Their waveforms are expected to be highly irregular so we are only able to search for them by using an EM detection as an indicator that there may be a GW signal present within the data. Short gamma ray bursts (sGRBs) are thought to originate from the coalescence of BNS or NSBH, which then send out two highly energetic γ -rays in opposite directions that are orthogonal to the orbital plain. If these beams are pointed towards us then we would observe it as a sGRB. These GW signals may be too weak for us to detect with the standard inspiral analysis pipeline but by knowing the sky-position we are able to perform targeted searches which allow us to increase the horizon distance. GWs being emitted from supernovae are expected to be much weaker, hence why we only consider galactic sources, and their waveforms are hard to model due to us not fully understanding all the mechanisms, so again by knowing the sky position allows us to search for coherent excess strain power in the data.

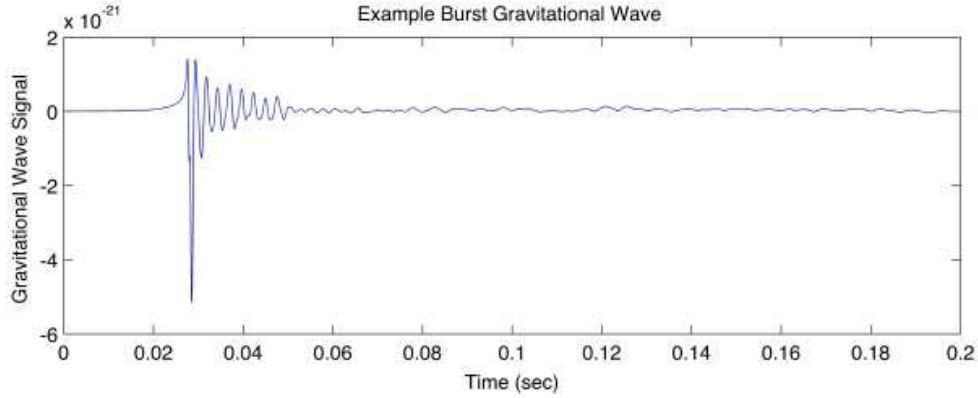


FIGURE 2.2: Example of an burst waveform [27]. We see that the waveform is both highly irregular and has a very short duration.

2.2.3 Stochastic

The stochastic gravitational wave background (SGWB) arises from the superposition of a large number of unresolvable sources [28, 29], of both astrophysical and cosmological origins. These signals, originating from the whole sky, are not individually detectable but will still be present within the detector data streams. Cosmological sources include the inflation of the early universe [30–33], phase transitions [29], or cosmic (super)strings [34–39]. There is also an expected astrophysical contribution from many sources, such as core collapse supernovae [40–43], white dwarf binaries [44], or the inspiral of more massive compact binaries consisting of neutron stars and/or black holes [45–49].

A gravitational wave background is defined in terms of its energy density spectrum, $\Omega_{\text{gw}}(f)$. This is a fractional contribution of gravitational wave energy density out of the total energy density, including contributions from mass (Ω_m) and dark energy (Ω_Λ), that is needed to close the universe [28], where

$$\Omega_{\text{gw}}(f) = \frac{1}{\rho_c} \frac{d\rho_{\text{gw}}}{d \ln f}, \quad (2.7)$$

here $d\rho_{\text{gw}}$ is the gravitational-wave energy density between the frequency range of f and $f + df$, and

$$\rho_c = \frac{3c^2 H_0^2}{8\pi G}, \quad (2.8)$$

is the critical energy density of the universe which is approximately 10^{-26} kg/m³.

2.2.4 Continuous

Continuous GWs are signals that are emitted with a constant frequency. Potential sources of these are rapidly rotating asymmetric neutron stars that have a mountain or deformity, with

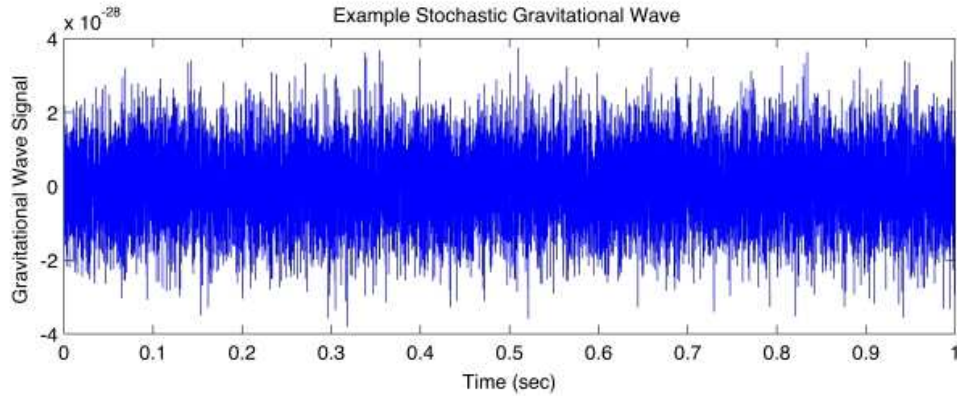


FIGURE 2.3: Example of an stochastic signal [27] that is continuous in nature.

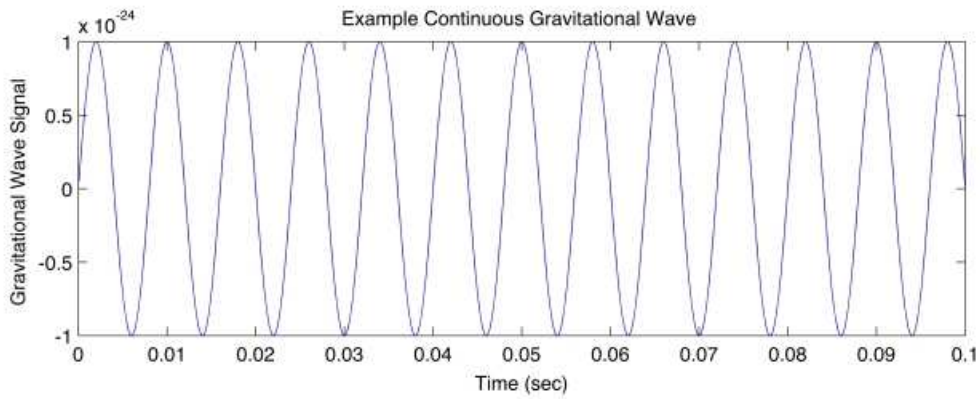


FIGURE 2.4: Example of an continuous waveform [27]. We see that the frequency and amplitude are both very regular.

ideal candidates being millisecond pulsars that we already know the sky position and rotational frequency of [50]. The GW produced by these, which are emitted at twice the rotational frequency of the pulsar, are expected to be extremely weak when compared to the other types of sources, typically of the order of

$$h \approx 6 \times 10^{-26} \left(\frac{f_{\text{gw}}}{500\text{Hz}} \right)^2 \left(\frac{10\text{kpc}}{d} \right) \left(\frac{\epsilon}{10^{-6}} \right), \quad (2.9)$$

where ϵ is the pulsar's ellipticity, a measure of the deviation away from a perfect spherical shape.

2.3 GW Detectors

The instruments that are used to try and detect gravitational waves are Michelson interferometers, a diagram of which can be seen in Fig. 2.5. These consist of a high powered laser beam that is sent down two arm cavities, orientated at 90° to each other, via a beam splitter. At the end of each arm cavity a test mass is placed coated with a highly reflective surface that redirects the beams back towards the beam splitter, where the two are recombined and sent towards a photo

detector. The length of the two arms are accurately set to be equal so that when the two beams are recombined their phases will be the same. As was shown earlier, if this is carried out while a GW passes through the detector, it will have the effect of changing the proper distance of both the arms, proportional to the amplitude of the GW signal. This oscillation in the arm length will then cause the recombined laser beam to shift in and out of phase due to the constructive and destructive interference of the two beams phases.

The amount by which the arms are displaced depends upon the amplitude h of the gravitational wave and is given by the equation

$$\frac{dL}{L} = \frac{h}{2}, \quad (2.10)$$

where L is the length of the arms and dL is the amount by which this length changes. If we consider a typical signal amplitude of $h = 1 \times 10^{-21}$, then for an arm length of 1m the amount by which it changes is $dL = 0.5 \times 10^{-21}$ m. To make this change measurable we require that the arm lengths of the interferometer be much longer, of the order kms. The LIGO and Virgo detectors have arm lengths of 4km and 3km, respectively, which results in a change of length of $\sim 1 \times 10^{-18}$ m. This can be further reduced by use of a second set of test mass mirrors, located at the base of the arm cavities, that reflect the laser beams along the arms multiple times before they are recombined at the beam splitter, affectively increasing the light path distance.

The proposed third generation detector, the Einstein Telescope, differs from the standard design by having three interferometers with arm opening angles of 60° , and arranged in a triangle formation with arm lengths of 10kms as well as being placed underground [17, 51, 52]. This configuration will also result in the creation of a *null stream*, which is produced by the sum of the three detector streams and results in the complete cancellation of any GW signals [18]. This is due to the fact that a positive displacement in the x direction of one detector will be equal to the negative displacement in the x direction in the second, and so by constructing a closed loop detector, we are able to remove coherent GW signals originating from any sky position.

2.4 Data Analysis

There are many data analysis techniques that have been developed for the detection of gravitational waves, each with a focus on specific signal, but here I will cover the standard algorithm used to search for the main type of signal that are covered in this thesis, namely the search for CBC and stochastic signals. The detector output signal, $s_i(t)$, where i indicates which detector in a network of detectors, contains background noise $n(t)$ plus a possible GW signal $h(t)$, such that

$$s_i(t) = n(t) + h(t), \quad (2.11)$$

and the Fourier transform of the detector output is given by

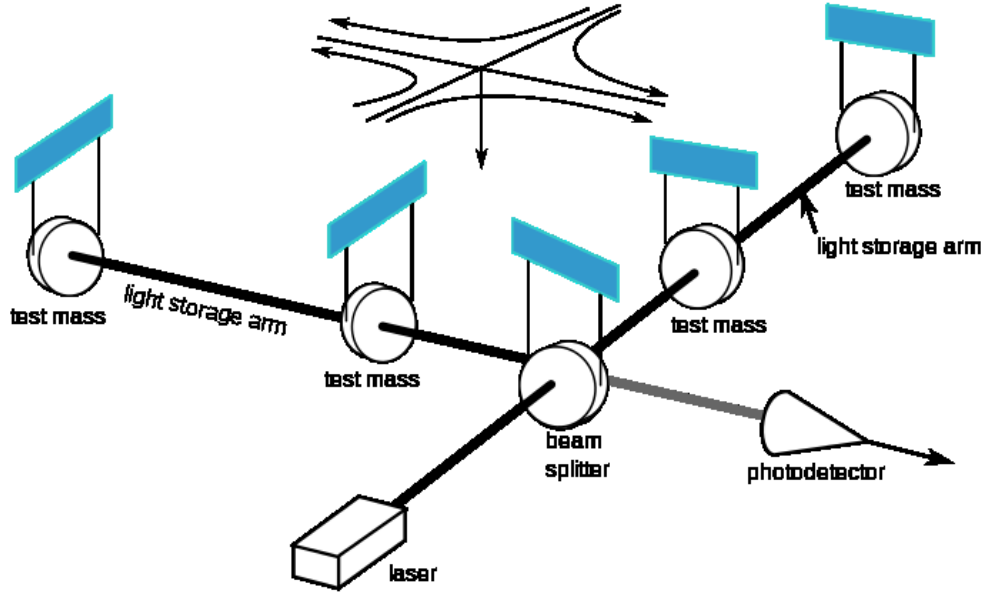


FIGURE 2.5: Example of an interferometer [27] with main components labeled.

$$\tilde{s}_i(f) = \int_{-\infty}^{\infty} s_i(t) e^{2i\pi ft} dt. \quad (2.12)$$

2.4.1 Matched Filtering

Matched filtering is a signal processing method that is used when searching for known signals that can be contained within noise, as is the case when searching for inspiraling CBC signals [23, 25, 53–57]. The known signal, h , labelled as the template, is used to extract the signal from the data. We then use this template to search against the data stream in order to try and “match” with the signal

$$\frac{1}{T_{\text{obs}}} \int_0^T s(t)h(t) dt = \frac{1}{T_{\text{obs}}} \int_0^T h^2(t) dt + \frac{1}{T_{\text{obs}}} \int_0^T n(t)h(t) dt. \quad (2.13)$$

Here the first integral on the right-hand side will always be positive, however, the second integral on the right-hand side, when taken over a long enough observation time, T_{obs} , will average out to zero.

The expected strength of a matched signal is given by

$$S = \int_{-\infty}^{\infty} \tilde{h}(f) \tilde{K}^*(f) df, \quad (2.14)$$

where

$$\tilde{K}(f) \propto \frac{\tilde{h}(f)}{S_n(f)}, \quad (2.15)$$

is an optimal filter function that maximises the signal-to-noise ration (SNR), where $S_n(f)$ is the power spectral density of the detector, examples of which are shown in Fig. 2.6. The noise is then given by

$$N^2 = \int_{-\infty}^{\infty} \frac{1}{2} S_n(f) |\tilde{K}(f)|^2 df, \quad (2.16)$$

and the resultant SNR of the matched signal is then given by

$$\text{SNR} = \left[4 \int_0^{\infty} \frac{|\tilde{h}(f)|^2}{S_n(f)} df \right]^{1/2}. \quad (2.17)$$

2.4.2 Cross-correlation

In the search for an isotropic SGWB signal we use the cross-correlation (CC) method (please see references such as [28, 58, 59] for a complete treatment). The optimal strategy to search for a Gaussian (or continuous) SGWB is to cross-correlate measurements of multiple detectors, $\tilde{s}_1(f)$ and $\tilde{s}_2(f)$. When the background is assumed to be isotropic, unpolarized and stationary, the cross correlation product is given by [28]

$$Y \simeq \int_{-\infty}^{\infty} \tilde{s}_1^*(|f|) \tilde{s}_2(|f|) \tilde{Q}(f) df, \quad (2.18)$$

and the expectation value of Y is

$$\langle Y \rangle = \frac{3H_0^2}{20\pi^2} T_{\text{obs}} \int_{-\infty}^{\infty} \frac{1}{|f|^3} \Omega_{\text{gw}}(|f|) \gamma(|f|) \tilde{Q}(f) df, \quad (2.19)$$

where

$$\tilde{Q}(f) \propto \frac{\gamma(f) \Omega_{\text{gw}}(|f|)}{|f|^3 P_1(|f|) P_2(|f|)}, \quad (2.20)$$

is the optimal filter that maximizes the SNR, $\Omega_{\text{gw}}(f)$ is the energy density in GWs as defined in Eq. (2.7), \tilde{s}_1 and \tilde{s}_2 are the Fourier transformed detector output streams from both detectors, $P_1(f)$ and $P_2(f)$ are the detector power spectral densities of the two detectors, examples of which are shown in Fig. 2.6, and $\gamma(f)$ is the normalized overlap reduction function [60], characterizing the loss of sensitivity due to the separation and the relative orientation of the detectors.

The expected variance, which is dominated by the noise, is given by

$$\sigma_Y^2 \approx \frac{T_{\text{obs}}}{4} \int_{-\infty}^{\infty} P_1(|f|) P_2(|f|) |\tilde{Q}(f)|^2 df, \quad (2.21)$$

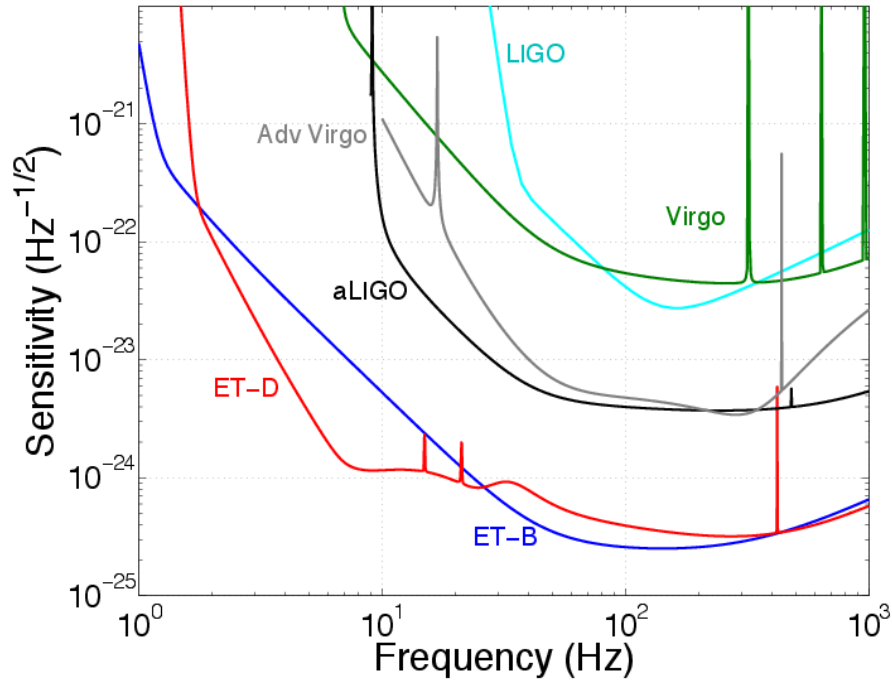


FIGURE 2.6: Projected sensitivity for second generation (advanced) detectors (here the aLIGO high-power zero detuning sensitivity [15] and Adv Virgo BNS optimized [16]) and for the initial configuration of ET, ET-B, considered in the Design Study, and the most evolved configuration ET-D [17]. The sensitivity of first generation detectors LIGO and Virgo is also shown for comparison.

and the expected (power) SNR of the CC statistic in the frequency range $f_{\min} - f_{\max}$, for an integration time T_{obs} is given by [61]

$$\text{SNR} = \sqrt{\frac{Y^2}{\sigma_Y^2}} = \frac{3H_0^2}{10\pi^2} \sqrt{T_{\text{obs}}} \left[\int_{f_{\min}}^{f_{\max}} \frac{\gamma^2(|f|) \Omega_{\text{gw}}^2(|f|)}{f^6 P_1(|f|) P_2(|f|)} df \right]^{1/2}. \quad (2.22)$$

2.5 Summary and Conclusion

The following few years promise to be a very exciting time in the field of general relativity with the upgrading of the gravitational wave detectors, LIGO and Virgo, nearing completion to their second generation. It is hoped that the first direct observation of a GW will be made within the first few years, and with that, a new window to the universe will open up to us. It will also confirm one of the last unanswered predictions made by Einstein when he developed the theory of general relativity.

Here I have briefly introduced the core concepts of gravitational waves and the methods by which we try to detect them. Gravitational waves are fluctuations or “ripples” in the fabric of space-time that propagate at the speed of light, carrying information about the system that generated them. These are produced by a wide range of processes, such as the coalescence of

compact binary objects, core collapse supernova, rapidly rotating pulsars or the remnants of the Big Bang. The amplitude of these ripples are very small, less than one part in $\sim 10^{21}$, and so measuring them is a very difficult process requiring very accurate detectors. For this we use a network of interferometers, located at different points around the Earth. These detectors, with arm lengths of several kms, are able to detect extremely small fluctuations in the proper distance between two points, caused by the passing of a GW. To be able to extract the signal from the data, very sophisticated data analysis algorithms are employed in the search for different types of signals.

I now fully explore the application of some of these data analysis algorithms in the search for gravitational waves with both the second generation, and proposed third generation, detectors.

Chapter 3

Statistical Properties of Astrophysical Gravitational-Wave Backgrounds

Phys. Rev. D, 89. 08406. (2014) [62]

D. Meacher, E. Thrane, T. Regimbau

3.1 Introduction

One of the science goals of second-generation gravitational-wave detectors such as Advanced LIGO [15] and Virgo [16] is to detect a stochastic gravitational-wave background. A stochastic background arises from the superposition of many gravitational-wave sources, each of which cannot be individually resolved [28, 29]. A stochastic background can be created in the early universe following inflation [30–33], during a phase transition [29], or from cosmic strings [34–39] to name a few scenarios. Less speculative astrophysical stochastic backgrounds are expected to arise from more vanilla objects such as compact binaries [45–49], neutron stars [63–71], core collapse supernovae [40–43], white dwarf binaries [44] and super-massive black hole binaries [72–74].

A stochastic background can be described in terms of its energy density spectrum $\Omega_{\text{gw}}(f)$, which is the fractional contribution of the energy density in gravitational waves relative to the total energy density needed to close the universe [28]:

$$\Omega_{\text{gw}}(f) = \frac{1}{\rho_c} \frac{d\rho_{\text{gw}}}{d \ln f}. \quad (3.1)$$

Here ρ_c is the critical energy density of the universe and $d\rho_{\text{gw}}$ is the gravitational-wave energy density between f and $f + df$. Typically, searches for a stochastic background estimate $\Omega_{\text{gw}}(f)$

using a cross-correlation statistic (see, e.g., [28, 58]), which we denote $\widehat{Y}(f)$. In [28], the estimator $\widehat{Y}(f)$ is derived for the case of an isotropic, unpolarised, and Gaussian background. While subsequent work has relaxed the assumption of isotropy [75, 76], it is still typically assumed that the observed background is Gaussian, (see, e.g., [58]). However, it is likely that the first detection of a stochastic background will be of a non-Gaussian background of astrophysical origin [48]. Non-Gaussian backgrounds exhibit fluctuations arising from the discrete nature of their composition; no two realisations are exactly the same.

In this paper we investigate how the non-Gaussianity of astrophysical stochastic backgrounds affects cross-correlation measurements of $\Omega_{\text{gw}}(f)$. First, we calculate $\langle \widehat{Y}(f) \rangle_{n,h}$, the expectation value of $\widehat{Y}(f)$ in the presence of a non-Gaussian background averaged over both realisations of detector noise and realisations of an astrophysical stochastic background. The answer, we show, is identical to the case of an isotropic Gaussian background. Next, we calculate $\langle \widehat{Y}(f) \rangle_n$, the expectation value of $\widehat{Y}(f)$ averaged over realisations of detector noise but considering only *a single realisation of an astrophysical background*. The answer, this time, is different than the case of an isotropic Gaussian background. By comparing these two calculations, we characterise the signature caused by the discreteness of astrophysical backgrounds. We proceed to estimate the size of this signature in upcoming observations by advanced detectors.

The remainder of the chapter is organised as follows. In section 3.2, we review the procedure for a cross-correlation search for a stochastic background (subsection 3.2.1), characterise the statistical behaviour of astrophysical backgrounds (subsections 3.2.2 and 3.2.3), and introduce a novel formalism for characterising astrophysical backgrounds. Then, in section 3.3, we present the results of a numerical investigation, which quantifies the statistical fluctuations between different realisations of the stochastic background. Finally, in section 3.4, we summarise our results and discuss the implication for future gravitational-wave observations.

3.2 Formalism

3.2.1 Cross-correlation searches for a stochastic background

We consider a cross correlation search [28] using two detectors i and j . The measured strain in detector i is given by

$$s_i(t) = h_i(t) + n_i(t), \quad (3.2)$$

where $h_i(t)$ is the gravitational-wave strain signal, $n_i(t)$ is the noise, and t is the sample time. At any given time t , there are, we assume, N_t gravitational-wave sources in the universe producing a strain signal. If the background is very non-Gaussian, N_t may be zero for many values of t . A background where $N_t \gg 1$ is quasi-Gaussian. If $N_t \geq 1$, we can write

$$h_i(t) = \sum_{k=1}^{N_t} h_{i,k}(t). \quad (3.3)$$

(If $N_t = 0$, then $h_i(t) = 0$.) Here $h_{i,k}(t)$, the observed strain from the k^{th} gravitational wave source, is implicitly a function of the sky location $\hat{\Omega}_k$ of the source. The strain signal can be written as

$$h_{i,k}(t) = h_{i,k}^A(t) F_{i,k}^A(\hat{\Omega}_k, t). \quad (3.4)$$

Here $h_{i,k}^A(t)$ is the Fourier coefficient of a plane-wave metric perturbation in the transverse traceless gauge

$$h_{ab}(t, \vec{x}) = \sum_{A=+, \times} \int_{-\infty}^{\infty} df h_A(f, \hat{\Omega}_k) e_{ab}^A(\hat{\Omega}_k) e^{-2\pi i f(t - \hat{\Omega}_k \cdot \vec{x}/c)}, \quad (3.5)$$

where $a, b = 1, 2, 3$ are indices in the transverse plane, $e_{ab}^A(\hat{\Omega})$ is the polarisation tensor, $A = +, \times$ is the polarisation, f is frequency, \vec{x} is the position vector of the observer and c is the speed of light. The $F^A(\hat{\Omega}, t)$ term in Eq. 3.4 is the detector response for direction $\hat{\Omega}$ at time t [28].

We define a strain cross-power estimator in terms of the Fourier transforms of two strain time series

$$\hat{Y}(f) \equiv Q(f) \sum_t \tilde{s}_i^*(f; t) \tilde{s}_j(f; t). \quad (3.6)$$

The sum in Eq. 3.6 is over data segments (typically 60 s long; see [58]). We use $(f; t)$ to denote a Fourier spectrum for a data segment beginning at time t , which is in contrast to the sampling time, denoted (t) . Here $Q(f)$ is a filter function chosen such that—if the stochastic background is Gaussian and isotropic—the expectation value of $\hat{Y}(f)$ is $\Omega_{\text{gw}}(f)$. Eq. 3.6 implicitly assumes that the detector noise is stationary. In the presence of non-stationary detector noise, the equation is modified to weight quiet times as more important than noisy times. For the sake of simplicity, we present our calculation using the assumption of stationary noise, though, we note that the results are independent of this assumption.

We now consider the expectation value of $\hat{Y}(f)$ averaging over realisations of detector noise: $\langle \hat{Y}(f) \rangle_n$. Here $\langle \dots \rangle_n$ denotes the ensemble average over realisations of detector noise

$$\langle \dots \rangle_n \equiv \int dn_i \int dn_j (\dots) p_n(n_i) p_n(n_j). \quad (3.7)$$

Here $p_n(n_i)$ and $p_n(n_j)$ are probability density functions describing the noise in detectors i and j . They are typically taken to be normally distributed, and indeed, this assumption is born out in practice; see, e.g., [58, 76]. Here, for the sake of compact notation, we assume that n_i and n_j have the same probability density function p_n , though, this assumption can be relaxed without affecting the results.

If the noise in each detector is uncorrelated then $\langle n_i^*(f; t)n_j(f; t) \rangle_n = 0$ and $\langle n_i^*(f; t)h_j(f; t) \rangle_n = 0$ while $\langle h_i^*(f; t)h_j(f; t) \rangle_n \neq 0$ (unless $h_i(f; t) = 0$ and/or $h_j(f; t) = 0$). Thus,

$$\begin{aligned} \langle \hat{Y}(f) \rangle_n = Q(f) \sum_t \sum_{k=1}^{N_t} \left\langle \left(h_{i,k}^+(f; t)F_{i,k}^+(t) + h_{i,k}^\times(f; t)F_{i,k}^\times(t) \right)^* \right. \\ \left. \left(h_{j,k}^+(f; t)F_{j,k}^+(t) + h_{j,k}^\times(f; t)F_{j,k}^\times(t) \right) \right\rangle_n. \end{aligned} \quad (3.8)$$

The parsing of the data into segments is merely a matter of convenience; the sums over t and $k = 1 \dots N_t$ are equivalent to a single sum from $k = 1 \dots N$ where $N \equiv \sum_t N_t$ (the total number of events that occur during the observation period). Thus,

$$\sum_t \sum_{k=1}^{N_t} h_{i,k}^A(f; t)F_{i,k}^A(t)h_{j,k}^{A'}(f; t)F_{j,k}^{A'}(t) = \sum_{k=1}^N h_i^A(f; k)F_i^A(k)h_j^{A'}(f; k)F_j^{A'}(k). \quad (3.9)$$

Here $F_i^A(k)$ and $F_j^{A'}(k)$ represent the time-averaged detector response for the k^{th} event in detectors i and j respectively. For most signals of interest for Advanced LIGO and Virgo, the detector response does not vary significantly over the time that the signal is in band, but this need not be the case for lower frequency detectors such as the proposed Einstein Telescope [18]. Note that since each event is associated with a specific direction $\hat{\Omega}_k$, $h_i^A(f; k)$ and $F_i^A(k)$ are both implicitly functions of $\hat{\Omega}_k$.

Combining Eq. 3.8 and Eq. 3.9, it follows that

$$\langle \hat{Y}(f) \rangle_n = Q(f) \sum_{k=1}^N \left\langle \left(h_i^+(f; k)F_i^+(k) + h_i^\times(f; k)F_i^\times(k) \right)^* \left(h_j^+(f; k)F_j^+(k) + h_j^\times(f; k)F_j^\times(k) \right) \right\rangle_n. \quad (3.10)$$

Since each event is associated with a specific direction, the signal for each event at detector i is related to the signal at detector j by a simple phase factor

$$h^A(f; k) \equiv h_j^A(f; k) = h_i^A(f; k)e^{2\pi i f \hat{\Omega}_k \cdot \Delta \vec{x}_k / c}, \quad (3.11)$$

where $\Delta \vec{x}_k = \vec{x}_{j,k} - \vec{x}_{i,k}$ is the separation vector between the two detectors at the time of event k . The vectors $\vec{x}_{i,k}$ and $\vec{x}_{j,k}$ are the positions of detector i and detector j respectively.

Combining Eq. 3.10 and Eq. 3.11, we obtain

$$\begin{aligned} \langle \widehat{Y}(f) \rangle_n = Q(f) \sum_{k=1}^N \left\langle e^{2\pi i f \hat{\Omega}_k \cdot \Delta \vec{x}_k / c} \left(|h^+(f; k)|^2 F_i^+(k) F_j^+(k) + |h^\times(f; k)|^2 F_i^\times(k) F_j^\times(k) + \right. \right. \\ \left. \left. h^{+*}(f; k) h^\times(f; k) F_i^+(k) F_j^\times(k) + h^{\times*}(f; k) h^+(f; k) F_i^\times(k) F_j^+(k) \right) \right\rangle_n. \end{aligned} \quad (3.12)$$

In the following subsections we explore the consequences of Eq. 3.12.

3.2.2 Average over realisations of a stochastic background

In this subsection, we use Eq. 3.12 to derive the expectation value of $\widehat{Y}(f)$ averaged over both detector noise *and* over realisations of a stochastic background:

$$\begin{aligned} \langle \widehat{Y}(f) \rangle_{n,h} \equiv \int dn_i p_n(n_i) \int dn_j p_n(n_j) \int dN p_N(N) \int \prod_{k=1}^N \prod_{A=+,\times} dh^A(f; k) \\ \int \frac{d^2 \hat{\Omega}_k}{4\pi} \int \frac{dt_k}{t_{\text{obs}}} \left(p_h(h_i^A(f; k)) \widehat{Y}(f) \right). \end{aligned} \quad (3.13)$$

Here p_N is the Poisson-distributed probability density function for the number of events occurring during one observing period (typically of duration ≈ 1 yr). The p_h term is the probability density function for the strain signal from each event at detector j (see Eq. 3.11). (In the next subsection, we focus on a stochastic background from binary neutron stars, which allows us to parametrise p_h in terms of sky location $\hat{\Omega}$, redshift z , inclination angle ι , polarisation angle ψ , and chirp mass M_c .) The source direction $\hat{\Omega}_k$ is assumed to be drawn from an isotropic distribution while the burst time t_k is assumed to be drawn from a uniform distribution on $[0, t_{\text{obs}}]$.

We assume that p_h is the same for the two polarisation states, which follows from rotational invariance. Thus, we may define average strain power spectral density per event $\mathfrak{H}(f)$

$$\langle |h^+(f; k)|^2 \rangle_{n,h} = \langle |h^\times(f; k)|^2 \rangle_{n,h} \equiv \frac{1}{2} \mathfrak{H}(f), \quad (3.14)$$

On average, the strain power spectral density observed during the full analysis is given by

$$H(f) = N \mathfrak{H}(f). \quad (3.15)$$

Strain power spectral density and energy density are simply related by:

$$H(f) = \frac{3H_0^2}{2\pi^2} \frac{\Omega_{\text{gw}}(f)}{f^3}. \quad (3.16)$$

where H_0 is the Hubble constant.

Individual sources such as compact binaries often emit elliptically polarised gravitational waves. However, if the probability distributions for the orientation and sky location of individual sources respect rotational and translational invariance, then the average polarisation of an ensemble of sources is zero:

$$\langle h^{+*}(f; k)h^\times(f, k) \rangle_{n,h} = \langle h^{\times*}(f; k)h^+(f, k) \rangle_{n,h} = 0. \quad (3.17)$$

We further assume that $H^A(f; k)$ and $\hat{\Omega}_k$ are uncorrelated.

Putting everything together, we obtain

$$\begin{aligned} \langle \hat{Y}(f) \rangle_{n,h} &= Q(f) \frac{\mathfrak{H}(f)}{2} \sum_{k=1}^N \left\langle e^{2\pi i f \hat{\Omega}_k \cdot \Delta \vec{x}_k / c} (F_i^+(k)F_j^+(k) + F_i^\times(k)F_j^\times(k)) \right\rangle_{n,h} \\ &= Q(f) \frac{H(f)}{2N} \sum_{k=1}^N \left\langle e^{2\pi i f \hat{\Omega}_k \cdot \Delta \vec{x}_k / c} (F_i^+(k)F_j^+(k) + F_i^\times(k)F_j^\times(k)) \right\rangle_{n,h} \end{aligned} \quad (3.18)$$

The only random variables left in Eq. 3.18 are sky location $\hat{\Omega}_k$ and emission time t_k since $F_i^A(k)$ and $\Delta \vec{x}_k$ are both implicit functions of t_k and $\hat{\Omega}_k$. Thus,

$$\left\langle e^{2\pi i f \hat{\Omega}_k \cdot \Delta \vec{x}_k / c} F_i^A(k)F_j^A(k) \right\rangle_{n,h} = \int \frac{dt_k}{t_{\text{obs}}} \int \frac{d\hat{\Omega}_k}{4\pi} e^{2\pi i f \hat{\Omega}_k \cdot \Delta \vec{x}_k / c} F_i^A(k)F_j^A(k). \quad (3.19)$$

The double integral over t_k and $\hat{\Omega}_k$ can be thought of as a single integral over sky position since an isotropic signal observed at time t_k produces a signal which is identical to the one produced at time t'_k . Thus,

$$\begin{aligned} \langle Y(f) \rangle_{n,h} &= Q(f) \frac{H(f)}{2N} N \int \frac{d\hat{\Omega}_k}{4\pi} e^{2\pi i f \hat{\Omega}_k \cdot \Delta \vec{x}_k / c} (F_i^+(k)F_j^+(k) + F_i^\times(k)F_j^\times(k)), \\ &= Q(f)H(f)\Gamma_{ij}(f), \end{aligned} \quad (3.20)$$

where $\Gamma_{ij}(f)$ is the overlap reduction function [28, 60, 77] :

$$\Gamma_{ij}(f) \equiv \frac{1}{8\pi} \int d\hat{\Omega} e^{2\pi i f \hat{\Omega} \cdot \Delta \vec{x}_k / c} (F_i^+(\hat{\Omega})F_j^+(\hat{\Omega}) + F_i^\times(\hat{\Omega})F_j^\times(\hat{\Omega})). \quad (3.21)$$

Here we use the normalisation convention from [77].

The overlap reduction function encodes information about the interference of gravitational-wave signal coming from different directions on the sky. Each pair of detectors ij has a different

overlap reduction function. It is also common to define a normalised overlap reduction function $\gamma(f)$ defined such that a colocated coaligned pair has $\gamma_{ij}(f = 0) = 1$. For identical interferometers with an opening angle δ ,

$$\gamma_{ij}(f) = (5/\sin^2 \delta)\Gamma_{ij}(f). \quad (3.22)$$

The expression for $\Gamma_{ij}(f)$ given in Eq. 3.22 is equivalent to the value obtained for an isotropic, unpolarised, Gaussian background [28]. This implies that, averaging over realisations of astrophysical backgrounds, a standard search for a stochastic background, assuming an isotropic, unpolarised, Gaussian background will yield an unbiased estimate for the $\hat{\Omega}(f)$, even if the actual background is non-Gaussian, so long as it is on average unpolarised, and on average isotropic. In the next subsection we investigate the statistical behaviour of individual realisations of a stochastic background.

3.2.3 Individual realisations of a stochastic background for compact binary coalescence

In this subsection, we study the expectation value of $\hat{Y}(f)$ for individual realisations of a stochastic background consisting of a finite number of binary neutron star coalescences. In the transverse traceless (TT) gauge, the strain signal Fourier coefficients can be written as

$$h_k^{+,TT}(f) = h_{0,k}(z) \frac{(1 + \cos^2 \iota_k)}{2} f^{-7/6}, \quad (3.23)$$

$$h_k^{\times,TT}(f) = h_{0,k}(z) \cos \iota_k f^{-7/6}, \quad (3.24)$$

which are related to the polarisations given in Eq. 3.4 by

$$h^+(f) = h^{+,TT}(f) \cos 2\psi + h^{\times,TT}(f) \sin 2\psi, \quad (3.25)$$

$$h^\times(f) = -h^{+,TT}(f) \sin 2\psi + h^{\times,TT}(f) \cos 2\psi, \quad (3.26)$$

where ψ is the angle by which the transverse plane is rotated. The amplitude of the signal is given by

$$h_{0,k}(z) = \sqrt{\frac{5}{24}} \frac{(GM_{c,k}(1+z_k))^{5/6}}{\pi^{2/3} c^{3/2} d_L(z_k)}. \quad (3.27)$$

Here $d_L(z)$ is the redshift-dependent luminosity distance and G is the gravitational constant.

We can now rewrite Eq. 3.12 as

$$\langle \widehat{Y}(f) \rangle_n = Q(f) \sum_{k=1}^N e^{2\pi i f \hat{\Omega}_k \cdot \Delta \vec{x}_k / c} h_{0,k}^2(z_k) f^{-7/3} \left[\frac{(1 + \cos^2 \iota_k)^2}{4} F_i'^+(k) F_j'^+(k) + \cos^2 \iota_k F_i'^{\times}(k) F_j'^{\times}(k) + \frac{(1 + \cos^2 \iota_k)}{2} \cos \iota_k (F_i'^+(k) F_j'^{\times}(k) + F_i'^{\times}(k) F_j'^+(k)) \right], \quad (3.28)$$

where

$$F_i'^+ = F_i^+ \cos 2\psi - F_i^{\times} \sin 2\psi, \quad (3.29)$$

$$F_i'^{\times} = F_i^+ \sin 2\psi + F_i^{\times} \cos 2\psi. \quad (3.30)$$

Comparing Eq. 3.20 and Eq. 3.28, we observe that it is useful to define a *discrete overlap reduction function*, denoted $\Gamma_N(f)$, which encodes the signal-cancelling behaviour of N discrete events

$$\Gamma_N(f) \equiv \frac{1}{K_N} \sum_{k=1}^N e^{2\pi i f \hat{\Omega}_k \cdot \Delta \vec{x}_k / c} h_{0,k}^2(z_k) \left[\frac{(1 + \cos^2 \iota_k)^2}{4} F_i^+(k) F_j^+(k) + \cos^2 \iota_k F_i^{\times}(k) F_j^{\times}(k) + \frac{(1 + \cos^2 \iota_k)}{2} \cos \iota_k (F_i^+(k) F_j^{\times}(k) + F_i^{\times}(k) F_j^+(k)) \right], \quad (3.31)$$

where K_N is a normalisation factor that is averaged over all events

$$K_N \equiv \sum_k h_{0,k}^2(z) \left(\frac{(1 + \cos^2 \iota_k)^2}{4} + \cos^2 \iota_k \right). \quad (3.32)$$

We note that, by assumption, the N events contributing to Γ_N are too weak to be resolved, and so $\Gamma_N(f)$ is a theoretical quantity that we do not know from measurement.

As in section 3.2.2, we can write Eq. 3.28 in the form

$$\langle \widehat{Y}(f) \rangle_n = Q(f) H_N(f) \Gamma_N(f), \quad (3.33)$$

where $H_N(f) = K_N f^{-7/3}$ is the strain power spectral density for one realisation from a finite set of astrophysical sources. (This expression for $H_N(f)$ is valid up to the gravitational-wave frequency of the last stable orbit, above which we assume $H_N(f) = 0$.) As before, we define

$$\gamma_N(f) = (5/\sin^2 \delta) \Gamma_N. \quad (3.34)$$

3.3 Numerical testing

This section is organised as follows. In subsection 3.3.1, we perform numerical simulations to qualitatively illustrate the behaviour of $\gamma_N(f)$ for different values of N . In subsection 3.3.2, we calculate the bias that occurs when we search for a non-Gaussian astrophysical background with the estimator designed for a Gaussian background. We also investigate how the results change if we include/exclude events loud enough to be detected individually.

3.3.1 Simulation

Our numerical simulation uses the following model. We consider a normally-distributed population of binary neutron stars with average mass $m_1 = m_2 = 1.33M_\odot$ and width $\sigma_m = 0.03M_\odot$. This mass distribution takes into account both observational data of double pulsar systems [78] as well as population synthesis models. We use a realistic redshift distribution which takes into account the star formation rate and delay time between the binary formation and coalescence [18, 79]. We assign random sky location using an isotropic distribution. The cosine of the inclination angle $\cos \iota$ is chosen from a uniform distribution on $[-1, 1]$. The polarisation angle ψ is chosen from a uniform distribution on $[0, 2\pi]$.

We generate many realisations of the stochastic background, each with a fixed number of events N . For each event, we calculate the matched filter signal-to-noise ratio ρ in order to determine if it is loud enough to be individually detected:

$$\rho^2 = \frac{5}{6} \frac{(GM_c(1+z))^{5/3} \mathcal{F}^2}{c^3 \pi^4/3 d_L^2(z)} \int^{f_{\text{LSO}}} df \frac{f^{-7/3}}{S_n(f)}. \quad (3.35)$$

Here $S_n(f)$ is the detector's strain noise power spectral density (taken to be the design sensitivity of Advanced LIGO), f_{LSO} is the (redshifted) gravitational-wave frequency of the last stable orbit, and

$$\mathcal{F}^2 \equiv \sum_i \left[\frac{1}{4} (1 + \cos^2 \iota)^2 (F_i'^+)^2 + \cos^2 \iota (F_i'^\times)^2 \right] \quad (3.36)$$

characterises the network response. The index i runs over three detectors: LIGO Hanford, LIGO Livingston, and Virgo. We exclude any events with $\rho \geq 8$.

For each realisation, we calculate $\gamma_N(f)$ (Eq. 3.34) for the LIGO Hanford, LIGO Livingston detector pair. (The sensitivity contribution from the Virgo-LIGO pairs is small enough to ignore.) We carry out the calculation for different values of $N = 10^2, 10^3 \dots 10^6$. In a 1 yr-long dataset, $N \approx 10^4$ corresponds to a pessimistic rate [79] (see also Table 3.1) and so the (very pessimistic) values of $N = 10^2$ and $N = 10^3$ are included for pedagogic purposes. The higher values of N ($\sim 10^4$ – 10^6) correspond to astrophysical rates ranging from pessimistic to realistic [79]. We do

TABLE 3.1: A list of binary neutron star coalescence rate densities as given in [79]. The first column labels whether a merger rate is optimistic (R_{high}), realistic ($R_{\text{realistic}}$) or pessimistic (R_{low}). The second column gives the rates of coalescing events per Mpc^3 per Myr. The third column gives the average time between successive events. The final column gives the total number of events in the universe that are expected to occur per year.

Expected Rate	$\dot{\rho}_0 (\text{Mpc}^{-3} \text{Myr}^{-1})$	Δt (s)	$N_{\text{events yr}^{-1}}$
R_{high}	10	1.25	2.5×10^7
$R_{\text{realistic}}$	1	12.5	2.5×10^6
$R_{\text{medium-low}}$	0.1	125	2.5×10^5
R_{low}	0.01	1250	2.5×10^4

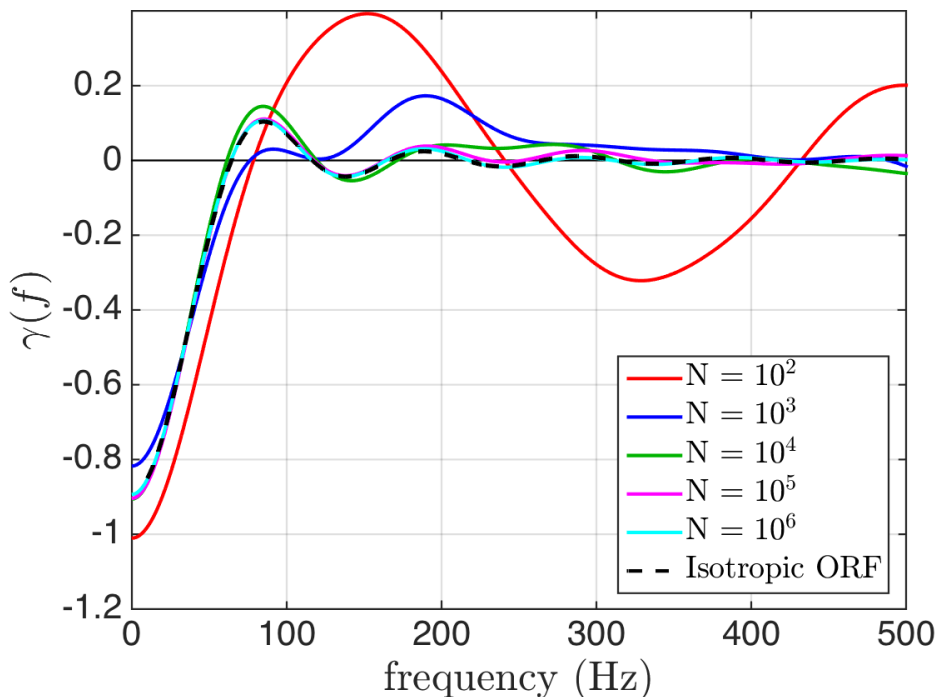


FIGURE 3.1: The discrete overlap reduction function $\gamma_N(f)$ for five different values of N . The overlap reduction function $\gamma(f)$ from a Gaussian isotropic background is shown by the black dashed line.

not include higher values of N because, as we shall see, $N = 10^6$ events in one year of science data produce a signal which is already difficult to distinguish from a Gaussian background.

In Fig. 3.1, we plot $\gamma_N(f)$ for individual realisations of the stochastic background, each with a different value of N . For comparison, the standard overlap reduction function for an unpolarised, isotropic, Gaussian background $\gamma(f)$ is shown with a black line. For small values of N , we see that $\gamma_N(f)$ can diverge significantly from $\gamma(f)$. As N increases, the overlap reduction function becomes closer to the Gaussian isotropic case. Thus, Fig. 3.1 demonstrates how the discreteness of an astrophysical stochastic background can create spectral features, which are not expected for a Gaussian background.

In Fig. 3.2a, we show ten realisations of $\gamma_N(f)$ for $N = 10^4$ (blue). As one would expect,

the mean of these ten realisations (red) is in good agreement with $\gamma(f)$ (black) as this can be considered as one realisation of $N = 10^5$ events. By comparing the red and black traces, it is possible to get a qualitative sense of the typical fluctuations due to discreteness at a fixed value of N . In Fig. 3.2b, we plot $\gamma_N(f) \pm \sigma_\gamma(f)$ where $\sigma_\gamma(f)$ is the (numerically estimated) standard deviation of $\gamma_N(f)$ due to fluctuations arising from the discreteness of the background. Finally, in Fig. 3.2c, we plot $\sigma_\gamma(f)$ to show that $\sigma_\gamma(f)$ is approximately constant in frequency. Since $\gamma_N(f)$ tends to get smaller at higher frequencies, this implies that the fractional uncertainty $\sigma_\gamma(f)/\gamma_N(f)$ tends to become larger at higher frequencies.

3.3.2 Bias

By combining results for many independent frequency bins, it is possible to significantly increase the signal-to-noise ratio of a stochastic broadband search [77]. If the spectral shape of the stochastic background $\Omega_{\text{gw}}(f)$ is known, the expectation value (averaged over realisations of noise) of the optimal broadband estimator for an astrophysical background with discrete events is given by [28]:

$$\langle \widehat{Y}_{\text{ISO}} \rangle_n = \frac{3H_0^2}{20\pi^2} t_{\text{obs}} \int df f^{-3} \Omega_{\text{gw}}(f) \gamma_N(f) Q'(f). \quad (3.37)$$

$Q'(f)$ is a filter function (not necessarily the same as $Q(f)$ for the narrowband estimator in Eq. 3.6) given by

$$Q'(f) = \lambda \frac{\gamma(f) \Omega_{\text{gw}}(f)}{f^3 S_n(f) S_n(f)}. \quad (3.38)$$

Here, λ is an overall normalisation constant and $\gamma(f)$ is the isotropic overlap reduction function. We have assumed, for the sake of simplicity, that the noise power spectral density $S_n(f)$ is the same for both detectors. For the background of binary coalescences considered here, $\Omega_{\text{gw}}(f) \propto f^{2/3}$.

Substituting $Q'(f)$ into Eq. 3.37, we obtain

$$\langle \widehat{Y}_{\text{ISO}} \rangle_n = \frac{3H_0^2}{20\pi^2} t_{\text{obs}} \int df \frac{\Omega_{\text{gw}}^2(f) \gamma_N(f) \gamma(f)}{f^6 S_n(f) S_n(f)}. \quad (3.39)$$

We can think of Eq. 3.39 as the case where we apply an isotropic Gaussian filter $Q'(f)$ to an unknown background, which is in reality non-Gaussian. If we had perfect knowledge of the N events responsible for the observed background, we could calculate a more accurate estimator, \widehat{Y}_N . By the same line of reasoning, the (noise-averaged) expectation value of \widehat{Y}_N in the presence of a known astrophysical background characterised by N events is

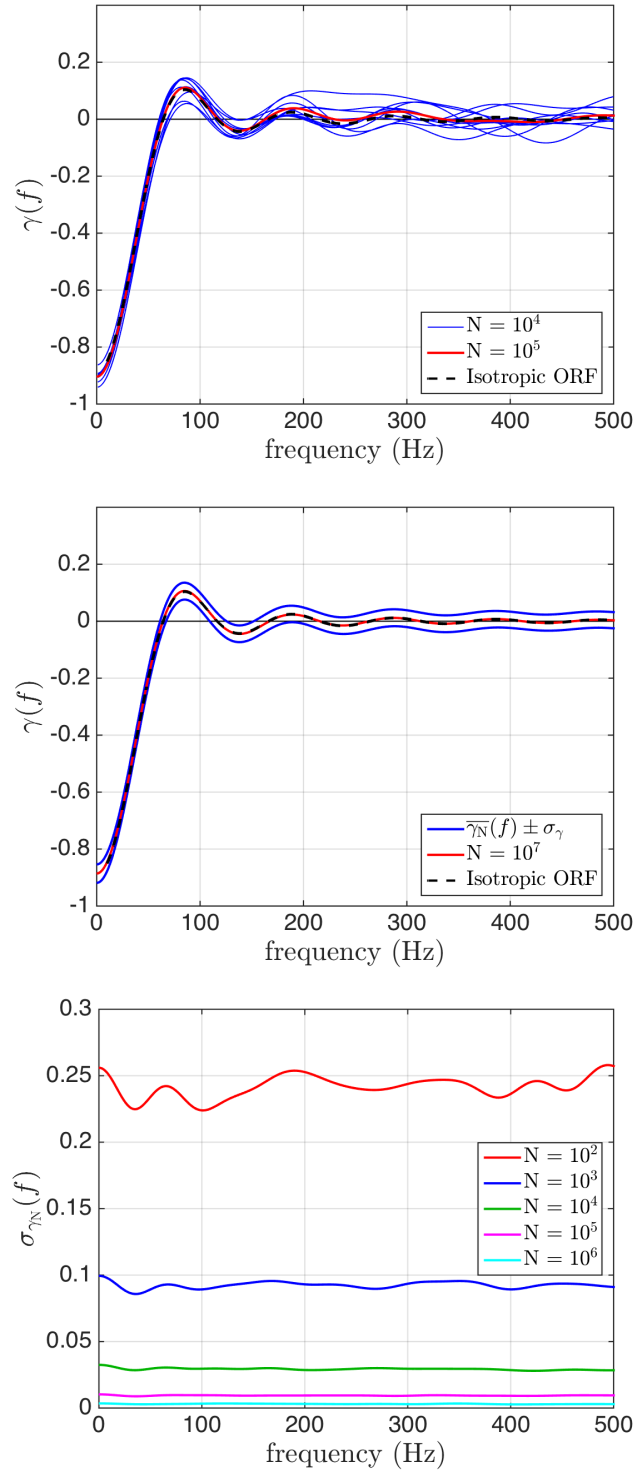


FIGURE 3.2: *Top*— Ten realisations of the discrete overlap reduction function $\gamma_N(f)$ with $N = 10^4$ events (blue). The mean of the blue curves is shown in red. The standard overlap reduction function $\gamma(f)$ is shown in dashed black. *Middle*— Using a simulation of 1000 realisations of $N = 10^4$ background sources, we calculate the standard deviation of $\gamma_N(f)$ at each frequency bin. The blue curves represent \pm one standard deviation about the mean, which is shown in red. The dashed black corresponds to $\gamma(f)$. *Bottom*— Variation in the overlap reduction function. We plot $\sigma_\gamma(f)$ —the standard deviation of the discrete overlap reduction function as a function of frequency. Each colour represents a different value of N . The magnitude of $\sigma_\gamma(f)$ is approximately constant, which implies that the fractional error grows as $\gamma_N(f)$ becomes smaller at higher frequencies.

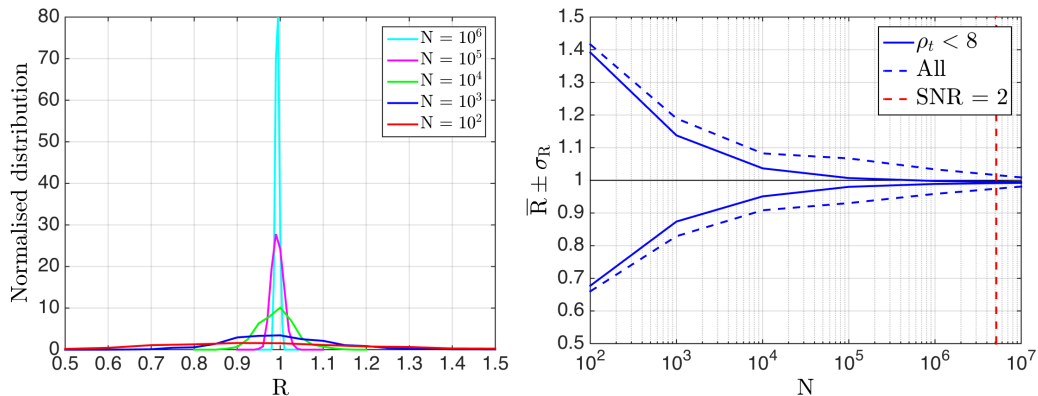


FIGURE 3.3: *Left*— Histogram of the fractional bias in a stochastic search R (see Eq. 3.41) due to the discreteness of a non-Gaussian background. Each colour corresponds to a different value of N . *Right*— The standard deviation σ_R of the left-hand-side histograms as a function of N (blue). The dashed lines include all events whereas the solid lines exclude events loud enough to resolve individually with matched filtering. The dashed red line corresponds to the number of events required to produce a stochastic signal that can be detected with $\text{SNR} = 2$ (see Eq. 3.42) using Advanced LIGO with an observational period of $t_{\text{obs}} = 1$ yr. Note that σ_R does not depend on t_{obs} whereas $\text{SNR} \propto t_{\text{obs}}^{1/2}$.

$$\langle \hat{Y}_N \rangle_n = \frac{3H_0^2}{20\pi^2} t_{\text{obs}} \int df \frac{\Omega_{\text{gw}}^2(f) \gamma_N^2(f)}{f^6 S_n(f) S_n(f)}. \quad (3.40)$$

By considering the ratio

$$R \equiv \frac{\langle \hat{Y}_N \rangle_n}{\langle \hat{Y}_{\text{ISO}} \rangle_n}, \quad (3.41)$$

we can characterise the fractional bias introduced into a stochastic search when we apply a Gaussian isotropic filter to a non-Gaussian background.

In Fig. 3.3a, we show histograms of R for different values of N . As N increases, the width of the distribution of R decreases, indicating that the fractional bias decreases as expected. In Fig. 3.3b, we plot the standard deviation of the distribution of R as a function of N . The dashed red line indicates the number of events that are required to occur within an observational period of $t_{\text{obs}} = 1$ yr in order to obtain a stochastic signal-to-noise ratio of 2. The average signal-to-noise ratio of a stochastic search is given by [28]

$$\text{SNR} \approx \frac{3H_0^2}{10\pi^2} \sqrt{t_{\text{obs}}} \left[\int df \frac{\Omega_{\text{gw}}^2(f) \gamma^2(f)}{f^6 S_n(f) S_n(f)} \right]^{1/2}. \quad (3.42)$$

Also in Fig. 3.3b, we show how the results change if we do not remove individually detectable events with $\rho \geq 8$; see the dashed blue lines. We find that the inclusion of loud events changes standard deviation of the fractional bias R by $\lesssim 8\%$ depending on the value of N .

3.4 Conclusions

Many previous studies of the stochastic gravitational-wave background have assumed a signal that is isotropic, unpolarised, and Gaussian. However, non-Gaussian backgrounds from compact binary coalescence represent one of the most exciting sources for second-generation detectors such as Advanced LIGO and Virgo. In this paper, we investigated the statistical properties of stochastic backgrounds originating from a discrete set of astrophysical sources and how they will appear in future cross-correlation searches. In the course of our investigation, we found it useful to define a novel description of astrophysical backgrounds: a discrete overlap reduction function. We find that the discreteness of astrophysical backgrounds is unlikely to produce a measurable bias in upcoming observations by second-generation detectors.

Here we focused on upcoming advanced detectors observing a population of binary neutron star sources. However, we note that the situation may be more complicated for the proposed third-generation Einstein Telescope [18]. In particular, we raise the possibility that the removal of above-threshold binary events may create a selection bias. This is because we expect face-on events, directly above the detector, will be preferentially detected compared to events with less favourable orientations and locations, which in turn, may create an apparent anisotropy. The effect may be more pronounced for the Einstein telescope (with only one detector) versus a network of 2–5 advanced detectors. Future work will characterise the magnitude of this effect for the Einstein Telescope.

Chapter 4

A Mock Data and Science Challenge for Detecting an Astrophysical Stochastic Gravitational-Wave Background with Advanced LIGO and Advanced Virgo

Phys. Rev. D, 92, 063002. (2015) [80]

D. Meacher, M. Coughlin, S. Morris, T. Regimbau, N. Christensen, S. Kandhasamy, V. Mandic,
J. D. Romano, E. Thrane

4.1 Introduction

According to various cosmological and astrophysical scenarios, we are bathed in a stochastic gravitational wave background (SGWB). Proposed theoretical cosmological models include the amplification of vacuum fluctuations during inflation[30, 31, 81], pre Big Bang models [82–84], cosmic (super)strings [36–38, 85], and phase transitions [86–88]. In addition to the cosmological background [29, 89], an astrophysical contribution [90] is expected to result from the superposition of a large number of unresolved sources, such as core collapse supernovae to neutron stars or black holes [40, 42, 43, 91], rotating neutron stars [65, 68], including magnetars [66, 67, 92, 93], phase transitions [94], or initial instabilities in young neutron stars [41, 95, 96], or compact binary mergers [47, 48, 97–99].

Many of these models are within reach of the next generation of gravitational-wave (GW) detectors such as Advanced LIGO Hanford (H) and Livingston (L) [15], which are expected to start collecting data in 2015, and Advanced Virgo (V) [16], which will begin collecting data in 2016. These detectors are expected to have a final sensitivity 10 times better than that of the initial detectors [11, 12], which will be achieved over a period of several years of continued upgrades. The detection of a cosmological background would provide very important constraints on the first instant of the Universe, up to the limits of the Planck era and the Big Bang, while the detection of an astrophysical background would provide crucial information on the physical properties of the respective astrophysical populations, the evolution of these objects with redshift, the star formation history or the metallicity [58, 75, 90, 100–102].

In order to prepare and test our ability at detecting the SGWB and interpreting valuable information from the data, we are conducting a series of mock data and science challenges (MDSC), with increasing degrees of complexity. In this first paper, we focus on a SGWB created by all the unresolvable compact binary coalescences (CBC) such as binary neutron stars (BNS), neutron star-black holes (NSBH) or binary black holes (BBH), up to a redshift $z = 10$, which may dominate within our search frequency range. Such a background may have a realistic chance of being detected after a few years of operation of the advanced detectors [48]. The observation of the SGWB will complement individual detections of a few to a few tens of CBC events per year [79] at close distances up to a few hundred Mpc.

For this study we produced multiple year-long data sets in the form of time series for the three advanced LIGO/Virgo detectors, containing both instrumental noise and the GW signal from a large number ($10^4 - 10^7$ per year) of compact binary sources out to redshift $z = 10$. This is done using a data generation package that was initially developed for the Einstein Telescope MDSC [18, 103]. The data sets are then analysed using a cross-correlation (CC) analysis pipeline in order to measure the total GW energy density, $\Omega_{\text{gw}}(f)$, of all the GW signals that make up the stochastic background [59]. We then use the results from these analyses to perform parameter estimation to try to determine some of the parameters of the injected populations, such as the average mass of all the sources, or the rate at which these binaries coalesce.

This chapter is organised into the following sections. In Section 4.2, we introduce the mock data sets and the methods by which we generate them. In Section 4.3, we briefly describe the analysis methods used to detect the stochastic signal. In Section 4.4, we discuss how we use the results from the analysis to estimate various astrophysical parameters. In Section 4.5, we present the results from various analysis runs of the different mock data sets. Finally in Section 4.6, we present our conclusions.

4.2 Mock Data

In this section, we introduce the mock data sets that we will be analysing as part of this investigation, as well as the data generation program we use to produce them. Initially we explain the various steps that are used to produce the mock data before detailing each of the data sets that will be considered as part of this MDSC. Finally we show how one can consider an astrophysical

SGWB as the superposition of many unresolvable single sources. The main data sets are split into two subsets, the first being produced with Gaussian noise, and the second produced using “glitchy” data taken from the initial LIGO S5 and initial Virgo VSR1 science runs which is re-coloured to have the sensitivity of the advanced detectors [55]. The GW signals injected into each set are the same for both the Gaussian and re-coloured noise, allowing us to make a direct comparison of how the analysis pipeline will behave in an ideal and in a more realistic case.

4.2.1 Mock Data Generation

The mock data generation package used here was originally developed for the Einstein Telescope MDSC [18] where one would expect to be able to make detections of individual sources out to $z \approx 3.8$ for BNS and even further for higher mass systems such as NSBH or BBH. Being able to realistically represent the population of sources at high redshift is essential when considering an astrophysical SGWB signal for the advanced detectors. This is because we expect very few CBC events to be directly detectable but the large number of unresolvable sources, when considering the whole universe, will all contribute to the SGWB. This is clearly seen in Fig. 4.1 where we show the redshift probability distribution, which is explained in the next section, of BNS (blue) and BBH (red) which take into account different delay times between the formation and merger of the inspiralling systems. We also plot the maximum horizon distance of the advanced detectors to directly detect individual BNS (blue dashed) and BBH (red dashed) signals [53]. We now describe how we generate and add the large number of GW signals to the detector data streams using both Gaussian and re-coloured noise.

4.2.1.1 Simulation of GW CBC signals

The Monte Carlo procedure we use to generate a population of compact binaries up to redshift of $z = 10$ is described in detail in [18, 105]. Here we summarize the main steps of the simulations.

The coalescence of a compact binary occurs after two massive stars in a binary system have collapsed to form a neutron star or a black hole¹ and have inspiralled through the emission of gravitational waves.

The coalescence rate in $\text{Mpc}^{-3} \text{ yr}^{-1}$ is given by [106–109]

$$\dot{\rho}_c(z, t_d) = \lambda \int \frac{\dot{\rho}_*(z_f)}{1 + z_f} P(t_d) dt_d. \quad (4.1)$$

In this expression, $\dot{\rho}_*$ is the star formation rate (SFR), measured in $M_\odot \text{ Mpc}^{-3} \text{ yr}^{-1}$ and the factor $1/(1 + z_f)$ accounts for time dilation due to the cosmic expansion. The redshift z describes when our compact binary merges, z_f is the redshift at which its progenitor massive binary formed, and $P(t_d)$ is the probability distribution of the delay between z and z_f , which is the sum of the time from initial binary formation to evolution into a compact binary, plus the merger time by emission of gravitational waves. The parameter λ (in M_\odot^{-1}) is the mass fraction that goes

¹We neglect the possible production of compact binaries through interactions in dense star systems.

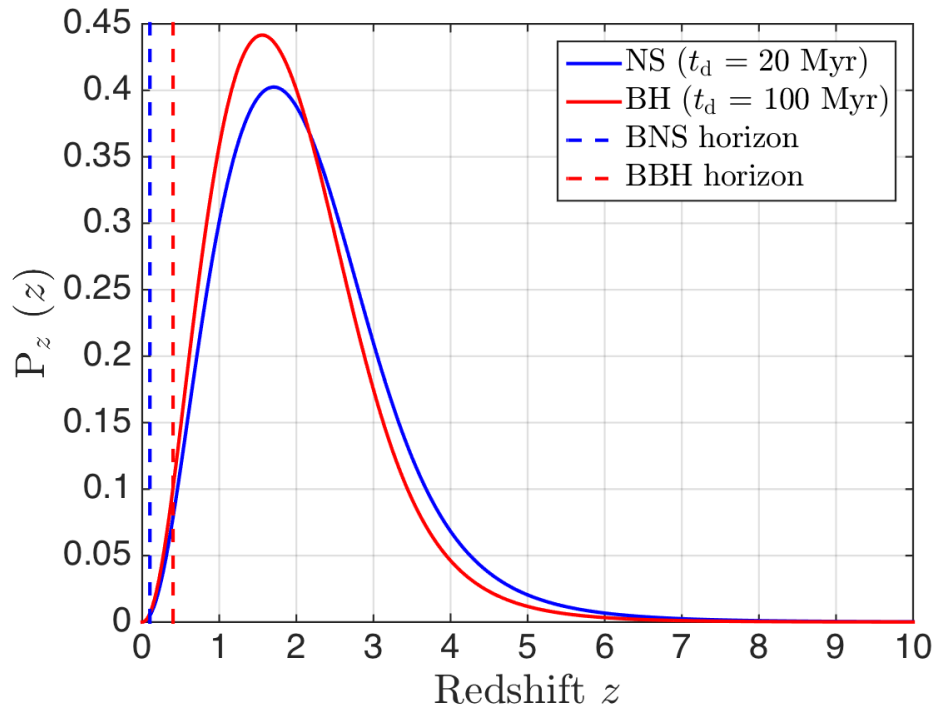


FIGURE 4.1: Source redshift probability distribution for BNS (blue) and BBH (red) where different delay times between the formation and merger of the binary system are considered. We also plot the horizon distance to BNS (dashed blue) and BBH (dashed red) for the advanced detectors with their design sensitivity which are defined as 445 Mpc ($z \sim 0.1$) and 2187 Mpc ($z \sim 0.4$) respectively [79].

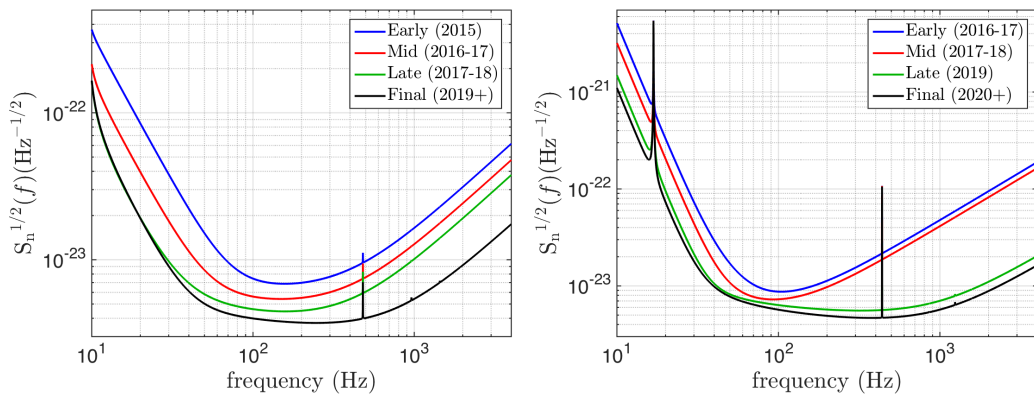


FIGURE 4.2: *Left*— Evolution of the Advanced LIGO sensitivities over the early (blue), middle (red), late (green) and design (black) phases [104]. *Right*— Evolution of the Advanced Virgo sensitivities over the early (blue), middle (red), late (green) and design (black) phases [104].

into the formation of the progenitors of compact binaries. The local coalescence rate at $z = 0$, $\dot{\rho}_c(0, t_d)$, is one of the parameters of our simulations and is denoted by ρ_0 .

The merger rate in the redshift interval $[z, z + dz]$ is obtained by multiplying $\dot{\rho}_c(z, t_d)$ with the element of comoving volume

$$\frac{dR}{dz}(z, t_d) = \dot{\rho}_c(z, t_d) \frac{dV}{dz}(z), \quad (4.2)$$

where

$$\frac{dV}{dz}(z) = 4\pi \frac{c}{H_0} \frac{r(z)^2}{E(\Omega, z)}, \quad (4.3)$$

where c is the speed of light in a vacuum, H_0 is the Hubble constant and

$$r(z) = \frac{c}{H_0} \int_0^z \frac{dz'}{E(\Omega, z')}, \quad (4.4)$$

where

$$E(\Omega, z) = \sqrt{\Omega_\Lambda + \Omega_m(1+z)^3}. \quad (4.5)$$

Here, we select the SFR given in [110] and use a standard Λ CDM cosmology with $\Omega_m = 0.3$, $\Omega_\Lambda = 0.7$ and Hubble parameter $H_0 = 70 \text{ km s}^{-1} \text{ Mpc}^{-1}$. Following [48, 100] we assume a distribution of the delay of the form $P(t_d) \propto 1/t_d$ with a minimal delay of 20 Myr for BNS and 100 Myr for BBH, as suggested by population synthesis [111–113].

We then proceed as follows for each source:

- The arrival time t_c of each GW signal is selected from a Poisson distribution. Here, the difference in arrival time, $\tau = t_c^k - t_c^{k-1}$, where k is the current event, is drawn from the exponential distribution $P(\tau) = \exp(-\tau/\bar{\tau})$ where $\bar{\tau}$ is the average time between successive events. The average waiting time between signals is calculated by taking the inverse of the coalescence rate, Eq. (4.2), integrated over all redshifts

$$\bar{\tau} = \left[\int_0^{10} \frac{dR}{dz}(z, t_d) dz \right]^{-1}. \quad (4.6)$$

- The redshift at the point of coalescence, z , is selected from a probability distribution $p(z, t_d)$ constructed by normalizing the coalescence rate in the interval $[0, 10]$ (see Fig. 4.1)

$$p(z, t_d) = \bar{\tau} \frac{dR}{dz}(z, t_d). \quad (4.7)$$

- The SGWB analysis is not sensitive to the width of the distribution of the masses, only to the average chirp mass, \mathcal{M} , of the system. This is a combination of the two component masses, m_1 and m_2 , given by

$$\mathcal{M} = \frac{(m_1 m_2)^{3/5}}{(M)^{1/5}}, \quad (4.8)$$

where $M = m_1 + m_2$ is the total mass of the system. Because of this, we choose a single value for the component masses for each of the systems being considered: $1.4M_\odot$ for neutron stars and $10M_\odot$ for black holes.

- The sky position, $\hat{\Omega}$, is selected from an isotropic distribution across the whole sky. The cosine of the inclination angle of the orbital plane to our line of sight, ι , the GW polarisation angle, ψ , and the phase angle at the time of coalescence, ϕ_0 , are all chosen from uniform distributions.
- We next calculate the theoretical signal-to-noise ratio (SNR), ρ , of the inspiral signal to determine if it is individually detectable by the standard LIGO-Virgo CBC search pipeline [53–56]. The SNR produced by the inspiral phase of the waveform for CBCs is given by

$$\rho^2 = 4 \int_{f_{\min}}^{f_{\text{isco}}} \frac{|F_+(\hat{\Omega}, \psi) \tilde{h}_+(f) + F_\times(\hat{\Omega}, \psi) \tilde{h}_\times(f)|^2}{S_n(f)} df, \quad (4.9)$$

where F_+ and F_\times are the antenna response functions to the two GW polarisations originating from sky position $\hat{\Omega}$ and with polarisation angle ψ , and \tilde{h}_+ and \tilde{h}_\times are the signal amplitudes in the frequency domain for the two polarisations. In the Newtonian regime, before the last stable circular orbit, \tilde{h}_+ and \tilde{h}_\times are given by

$$\tilde{h}_+(f) = h_z \frac{(1 + \cos^2 \iota)}{2} f^{-7/6}, \quad (4.10)$$

$$\tilde{h}_\times(f) = h_z \cos \iota f^{-7/6}, \quad (4.11)$$

where

$$h_z = \sqrt{\frac{5}{24}} \frac{(GM(1+z))^{5/6}}{\pi^{2/3} c^{3/2} d_L(z)}. \quad (4.12)$$

In the above equations G is the gravitational constant, d_L is the luminosity distance to the source at redshift z , f_{\min} is the starting frequency, which we select to be 10 Hz, S_n is the detector’s noise power spectral density (PSD) (see Fig. 4.2), and f_{isco} is the frequency of the last stable circular orbit, $f_{\text{isco}} \simeq \frac{c^3}{6^{3/2} \pi GM}$. For BNS signals it is enough to consider the waveform up until this point as the SNR contribution of the inspiral phase is dominant. However, for BBH signals we must also consider the contribution from the merger and ringdown of the waveform. The modifications to the calculations of \tilde{h}_+ and \tilde{h}_\times are given in [114]. The total SNR for the GW detector network is then given by

$$\rho^2 = \sum_A \rho_A^2, \quad (4.13)$$

where A is the sum over all detectors in the network. Any signals that pass a network threshold SNR ρ_T are then ignored by the SGWB search, where we set the network SNR threshold to 12.

- Finally, for any surviving sub-threshold events, we produce the waveforms that are then added to the detector data streams. Here, we have chosen to use the TaylorT4 time-domain waveform up to 3.5 post-Newtonian order in phase, and the most dominant post-Newtonian lowest order for amplitude, for the BNS signals. For the case of BBH signals, we choose the EOBNRv2 waveform produced from numerical relativity, which includes the merger and ringdown of the two coalescing black holes. This is up to 4th post-Newtonian order for phase and the lowest order for amplitude [115].

Once the time series data has been produced containing all the sub-threshold injections, we add either Gaussian noise or re-coloured noise data to produce the final mock data sets.

4.2.1.2 Simulation of Gaussian noise

Because each of the detectors being considered in this MDSC are well-separated in space, we assume that there will be no correlated noise between any of them; so the noise is simulated independently for each of the detectors [116, 117]. We do this by generating a mean zero, unit variance Gaussian time series which is then Fourier transformed into the frequency domain. This is then coloured using the PSD of the detector sensitivity of either aLIGO or AdVirgo (see Fig. 4.2) and is then finally Fourier transformed back into the time domain. To prevent any potential discontinuities of the data between adjacent segments of data, we taper the noise curve away to zero at frequencies below 10Hz and above 512Hz. This is then added to the time series containing the injected GW signals.

4.2.1.3 Re-coloured noise

To more accurately imitate the noise likely to be present in the advanced detectors, we also re-colour initial S5 LIGO and Virgo VSR1 data to have the sensitivity of aLIGO and AdVirgo. This has the benefit of preserving non-stationary noise artifacts while exploring the sensitivity of the pipelines to the signals. The noise spectra are estimated from the year of data and then averaged. The data is then re-coloured with a transfer function corresponding to the advanced detector power spectra divided by this averaged spectrum. The same GW signals are then added to these re-coloured time-series.

4.2.2 Mock Data Sets

To ensure that we have a detectable signal and to reduce computational costs, we have selected astrophysical models corresponding to the most optimistic rates given in [79] instead of using longer observational times to obtain the same SNR.

In total, we generate 5 data sets, of duration one year, all of which are produced with both Gaussian noise and re-coloured noise. For these data sets, we use the nominal design sensitivities of Advanced LIGO and Virgo, but in order to account for the improvement of the sensitivity, we also produce a sixth, observing scenario data set consisting of 3, 6, and 9 months and 1 and 3 years corresponding to the early, middle, late and design phases of the advanced detectors (see Fig. 4.2). This observing scenario, consisting of 5.5 years of data, should cover the full advanced detector observing period from mid 2015 until the end of 2022. Details of all the data sets are found in Table 4.1 and details on the rates and expected number of events are found in Table 4.2.

One part of the investigation is to see how having statistically different sources effects our analysis. When the rate and the duration of the GW events are large, the sources overlap each other creating a GW signal continuous in time (there is always a source present) which is Gaussian in nature due to the central limit theorem. However, for smaller rates or shorter waveforms, the time interval between successive events increases resulting in a non-continuous and non-Gaussian signal [100, 118]. Analytical calculations made in [62] and for the Einstein Telescope MDSCs [18, 103] suggest that when making a measurement of an astrophysical gravitational-wave background one just needs to consider the total number of coalescing events, with their relevant signal amplitudes, that occur within the observational period. The nature of the signals themselves will have no effect on the estimation of the SGWB. This is explained in greater detail later in Section 4.2.3. However these results have not been independently verified with the use of simulated data. We now describe each of these data sets being considered in this investigation.

4.2.2.1 Main data sets

Data set 0 is our control test for both the Gaussian and re-coloured data sets. The data streams for each of the detectors contain no coincident signals so there will be no correlated signals between any of the detectors. Thus, the results from the analysis of data set 0 should give us an accurate measurement of the expected error bars for each of the following data sets.

In data set 1, we have generated a large number of BNS signals with a merger rate of 10 coalescences per Mpc^3 per Myr that are injected into both the Gaussian and the re-coloured noise. Any individual events that surpasses a network SNR threshold value, as described in Section 4.2.1.1, are removed as it is possible for these signals to bias the results of the analysis. But given the expected number and length of the waveform when compared to the overall length of the observing time this effect is negligible, as demonstrated later in this paper. The top plot of Fig. 4.3 shows a 1000s segment of the time series produced from BNS contributing to data set 1. It is clearly seen that the GW signal is continuous at all times, so with this data set we investigate the effect that a continuous SGWB signal will have on our analysis.

Data set 2 contains the exact same sources with both Gaussian and re-coloured noise that are included in set 1 except that here we have not removed the loudest individually detectable events from the time series. This is to test by how much our results can be affected if we include the loud events in the analysis by comparing the results against that of the first data set.

In data set 3, we generate a number of BBH signals using a merger rate of 0.3 coalescences per Mpc^3 per Myr that are injected into both Gaussian and re-coloured data. With this data set we investigate the possible effects that a non-continuous (popcorn) SGWB will have on our analysis. The middle plot of Fig. 4.3 shows a 1000s segment of the time series produced from BBH contributing to data set 3. We see that, due to the shorter waveform lengths and lower coalescence rate, the GW signals are non-continuous or more “popcorn” like.

In data set 4 we have generated a number of both BNS and BBH signals, using the same rates stated above, which are injected into both Gaussian and re-coloured data. This set is to test the behaviour of the analysis and parameter estimate when analysing data from a SGWB having a contribution from more than one source. The bottom plot of Fig. 4.3 shows a 1000s segment of the time series produced from BNS and BBH signals contributing to data set 4. It is clearly seen that the GW signal is continuous at all times whilst still having louder popcorn like bursts from the BBH signals.

4.2.2.2 Observing scenario

The observing scenario data set is designed to realistically simulate the data that we would expect to obtain from the network of advanced detectors over the initial several years of operations. For this set, we generate a large number of BNS signals using a merger rate of 2 coalescence per Mpc^3 per Myr that are injected into Gaussian data. This is a lower rate than is used in set 1 as we are using a longer observational period. This Gaussian data differs from the previous data sets as we change the PSDs for each of the detectors at different stages to represent the improvements in sensitivities that are expected to be obtained in each observing run. Examples of this are shown in the left-hand plot for aLIGO, and right-hand plot for AdVirgo of Fig. 4.2. In reality we should take the final sensitivity of one phase as the initial sensitivity of the next, which would then gradually decrease to the next final sensitivity. However, here we consider the ideal case of taking the final sensitivity for the full duration of each phase. These observing runs are set out as follows [104]:

1. O1, 2015: This will consist of a 3-month observational run with both LIGO detectors (HL) with Early aLIGO sensitivity.
2. O2, 2016-17: This will consist of a 6-month observational run with all three detectors (HLV), where the HL detectors will have Mid aLIGO sensitivity and V will have Early AdVirgo sensitivity.
3. O3, 2017-18: This will consist of a 9-month observational run with all three detectors (HLV), where the HL detectors will have Late aLIGO sensitivity and V will have Mid AdVirgo sensitivity.

TABLE 4.1: Table describing the data sets that are produced as part of the MDSC. The first column is the reference number of the data set. The second column indicates if the data set is produced with just Gaussian noise or with re-coloured noise as well. The third column shows what sources are injected into the data set. The fourth column gives the rate of events used, see Table 4.2. The fifth column gives the length of the data set.

Data Set	Noise	Sources	Rate (Mpc ⁻³ Myr ⁻¹)	T _{obs}
0	Gaussian & Re-coloured	–	–	1 year
1	Gaussian & Re-coloured	BNS (sub-threshold)	10	1 year
2	Gaussian & Re-coloured	BNS (all)	10	1 year
3	Gaussian & Re-coloured	BBH (sub-threshold)	0.3	1 year
4	Gaussian & Re-coloured	BNS + BBH (sub-threshold)	10+0.3	1 year
Observing Scenario	Gaussian	BNS (sub-threshold)	2	5.5 years

TABLE 4.2: A list of compact binary coalescence rate densities as given in [79]. The first column labels whether a merger rate is optimistic (R_{high}), realistic ($R_{\text{realistic}}$) or pessimistic (R_{low}). The second column gives the rates of coalescing events. The third column gives the average time between successive events. The final column gives the total number of events out to $z = 10$ that are expected to occur per year.

	Rate (Mpc ⁻³ Myr ⁻¹)	$\bar{\tau}$ (s)	N _{events} (yr ⁻¹)
BNS			
R_{high}	10	1.35	2.3×10^7
$R_{\text{realistic}}$	1	13.5	2.3×10^6
$R_{\text{medium-low}}$	0.1	135	2.3×10^5
R_{low}	0.01	1350	2.3×10^4
BBH			
R_{high}	0.3	64.7	4.9×10^5
$R_{\text{realistic}}$	0.005	3880	8133
$R_{\text{medium-low}}$	0.001	19400	1627
R_{low}	0.0001	194000	163

- O4, 2019: This will consist of a year long observational run with all three detectors (HLV), where the HL detectors will have the final design aLIGO sensitivity and V will have Late AdVirgo sensitivity.
- O4 (*continued*), 2020-22: This will consist of a 3 year long observational run with all three detectors (HLV), where the HL detectors will have the final design aLIGO sensitivity and V will have the final design AdVirgo sensitivity.

4.2.3 Astrophysical stochastic background from CBC

The spectrum of the SGWB is usually characterized by the dimensionless parameter

$$\Omega_{\text{gw}}(f) = \frac{1}{\rho_c} \frac{d\rho_{\text{gw}}}{d \ln f}, \quad (4.14)$$

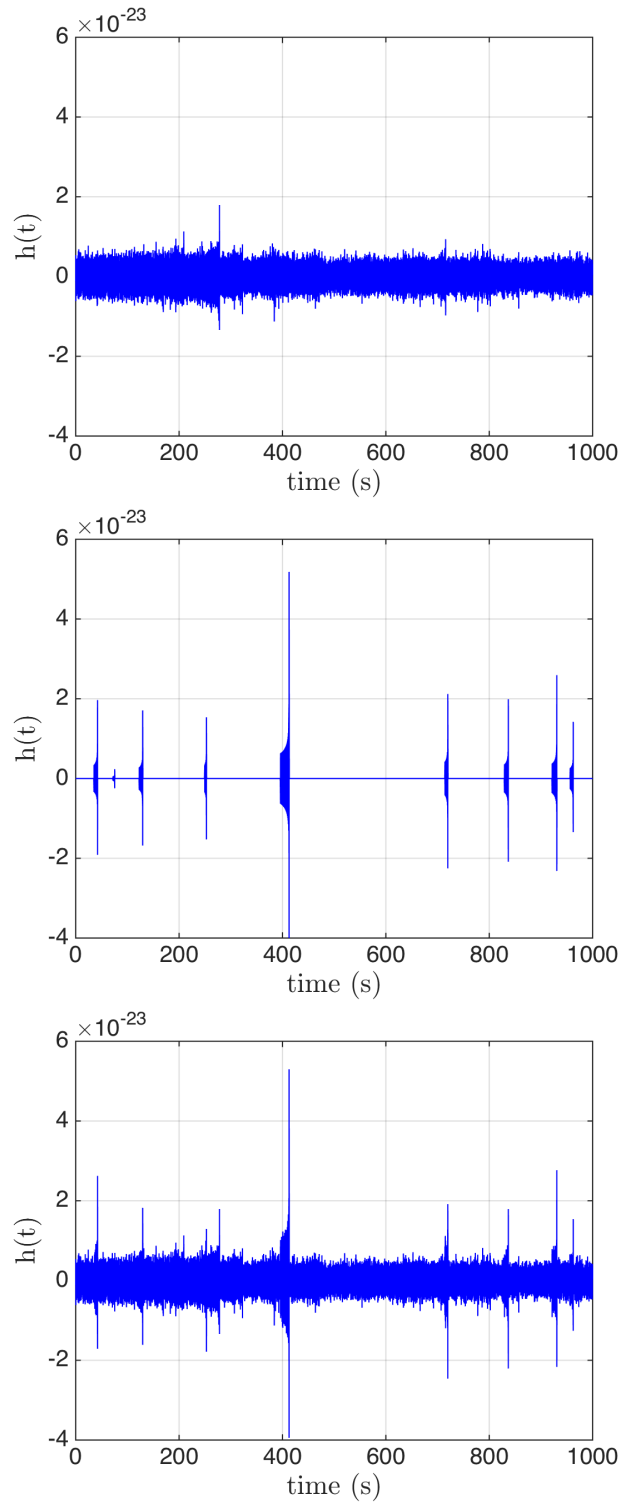


FIGURE 4.3: *Top*— A 1000s segment of the time series for BNS signals using the higher LIGO rate of $10 \text{ Mpc}^{-3} \text{ Myr}^{-1}$. This signal appears continuous. *Middle*— A 1000s segment of the time series for BBH signals of mass $10 + 10 M_{\odot}$, using the higher LIGO rate of $0.3 \text{ Mpc}^{-3} \text{ Myr}^{-1}$. This signal appears non-continuous (popcorn). *Bottom*— A 1000s segment of the time series for mixed BNS and BBH signals with higher LIGO rates and BH mass of $10M_{\odot}$. This signal appears as a popcorn background from BBH on top of a continuous background from BNS.

where ρ_{gw} is the gravitational-wave energy density, f the frequency in the observer's frame and, $\rho_c = \frac{3c^2 H_0^2}{8\pi G}$, is the critical energy density needed to close the Universe today. The GW spectrum from the population of extra-galactic compact binaries is given by the expression

$$\Omega_{\text{gw}}(f) = \frac{1}{\rho_c c} f F(f), \quad (4.15)$$

where $F(f)$ is the total flux. The total flux is the sum of the individual contributions

$$F(f) = T_{\text{obs}}^{-1} \frac{\pi c^3}{2G} f^2 \sum_{k=1}^N (\tilde{h}_{+,k}^2 + \tilde{h}_{\times,k}^2), \quad (4.16)$$

where N is the total number of coalescences in the data and k is the index of the individual coalescence. The normalization factor T_{obs}^{-1} assures that the flux has the correct dimension, $T_{\text{obs}} = 1$ yr being the length of the data sample.

In the Newtonian regime, before the last stable circular orbit, the Fourier transforms \tilde{h}_+ and \tilde{h}_\times are given by Eqs. (4.10 - 4.12). This gives for the energy density parameter [62]

$$\Omega_{\text{gw}}(f) = \frac{5\pi^{2/3} G^{5/3} c^{5/3}}{18c^3 H_0^2} f^{2/3} \sum_{k=1}^N \frac{(\mathcal{M}_k(1+z_k))^{5/3}}{d_L(z_k)^2} \left(\frac{(1+\cos^2 \iota_k)^2}{4} + \cos^2 \iota_k \right). \quad (4.17)$$

This equation is valid for BNS signals where we have considered only the inspiral phase, but for BBH signals, there is an extra contribution coming from the merger and ringdown phases. Fig. 4.4 shows $\Omega_{\text{gw}}(f)$ for the population of BNS (blue), and BBH (red) in the mock data sets described in the previous section. The plot in black corresponds to the sum of the signal from BNS and BBH. For BNS and BBH signals, $\Omega_{\text{gw}}(f)$ increases as $f^{2/3}$ from the inspiral phase (then as $f^{5/3}$ from the merger phase for BBH) before it reaches a maximum and decreases dramatically. The peaks occur at frequencies corresponding roughly to the f_{lsc} and the end of the ring-down phase at $z \sim 1.5$ where the coalescence rate is maximal. The amplitude of the background scales with both the rate of coalescing events and the average chirp mass of all the signals. It is larger for the BNS background (data set 1) than for the BBH contribution (data set 3) because, even though the chirp mass is smaller, the rate we have considered is larger.

4.3 SGWB Search

In this section, we briefly describe the cross-correlation (CC) method by which we analyse the data (please see references such as [28, 58, 59] for a complete treatment). The optimal strategy to search for a Gaussian (or continuous) SGWB is to cross-correlate measurements of multiple detectors, $\tilde{s}_1(f)$ and $\tilde{s}_2(f)$. When the background is assumed to be isotropic, unpolarized and stationary, the cross correlation product is given by [28]

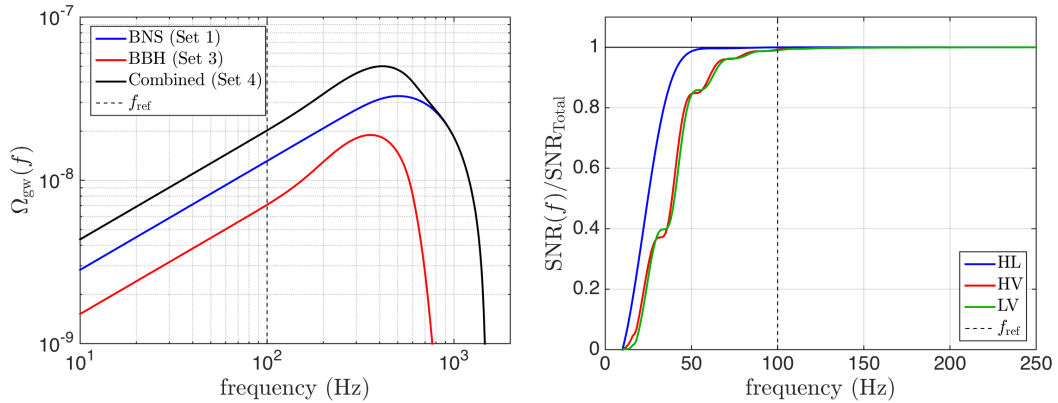


FIGURE 4.4: *Left*— Energy density $\Omega_{\text{gw}}(f)$ for the population of BNS (blue), BBH (red), and the combination of the two populations (black) as used in data sets 1, 3 and 4 respectively. The plots are calculated using the higher LIGO rates of $10 \text{ Mpc}^{-3} \text{ Myr}^{-1}$ (BNS) and $0.3 \text{ Mpc}^{-3} \text{ Myr}^{-1}$ (BBH). We also plot the reference frequency for which we report all the results in this investigation, shown by the black dashed line. *Right*— Fraction of the total theoretical SNR for the three detector pairs, HL (blue), HV (red), and LV (green). This is calculated using the frequency band $[10 - 250] \text{ Hz}$, as given by Eq. (4.22), and assuming $f^{2/3}$, which is used for the analysis. We also plot the reference frequency for which we report all the results in this investigation, shown by the black dashed line.

$$Y \simeq \int_{-\infty}^{\infty} \tilde{s}_1^*(|f|) \tilde{s}_2(|f|) \tilde{Q}(f) df, \quad (4.18)$$

and the expectation value of Y is

$$\langle Y \rangle = \frac{3H_0^2}{20\pi^2} T_{\text{obs}} \int_{-\infty}^{\infty} \frac{1}{|f|^3} \Omega_{\text{gw}}(|f|) \gamma(|f|) \tilde{Q}(f) df, \quad (4.19)$$

where

$$\tilde{Q}(f) \propto \frac{\gamma(f) \Omega_{\text{gw}}(|f|)}{|f|^3 P_1(|f|) P_2(|f|)}, \quad (4.20)$$

is the optimal filter that maximizes the SNR, $\Omega_{\text{gw}}(f)$ is the energy density in GW as defined in Eq. (4.14), \tilde{s}_1 and \tilde{s}_2 are the detector output streams from both detectors in the frequency domain, $P_1(f)$ and $P_2(f)$ are the detector power spectral densities of the two detectors and $\gamma(f)$ is the normalized overlap reduction function [60], characterizing the loss of sensitivity due to the separation and the relative orientation of the detectors. The cross correlation can take on negative (or positive) values due to fluctuations produced by noise. We are reporting the raw results, hence the occurrence of negative values. However, the presence of a sufficiently strong stochastic gravitational-wave background will produce a positive value for the energy density.

The expected variance, which is dominated by the noise, is given by

$$\sigma_Y^2 \approx \frac{T_{\text{obs}}}{4} \int_{-\infty}^{\infty} P_1(|f|) P_2(|f|) |\tilde{Q}(f)|^2 df, \quad (4.21)$$

and the expected (power) SNR of the CC statistic in the frequency range $f_{\min} - f_{\max}$, for an integration time T_{obs} is given by [61]

$$\text{SNR} = \frac{Y}{\sigma_Y} = \frac{3H_0^2}{10\pi^2} \sqrt{T_{\text{obs}}} \left[\int_{f_{\min}}^{f_{\max}} \frac{\gamma^2(|f|) \Omega_{\text{gw}}^2(|f|)}{f^6 P_1(|f|) P_2(|f|)} df \right]^{1/2}, \quad (4.22)$$

where we usually assume a filter of the form

$$\Omega_{\text{gw}}(f) = \Omega_{\alpha}(f/f_{\text{ref}})^{\alpha}, \quad (4.23)$$

where Ω_{α} is defined as $\Omega_{\text{gw}}(f)$ at the reference frequency f_{ref} .

For this MDSC, we set $f_{\min} = 10\text{Hz}$, $f_{\max} = 250\text{Hz}$, use a reference frequency of $f_{\text{ref}} = 100\text{Hz}$ and set $\alpha = 2/3$ as this is the theoretical value produced from the inspiral phase of CBCs. In the right hand plot of Fig. 4.4 we show the fractional SNR build-up as a function of frequency for different detector pairs. We see that for all three pairs we reach to nearly 100% of the total SNR by 120Hz, which is contained well within the limits we have set above for the analysis.

4.4 Parameter Estimation

Parameter estimation of signal models requires, at first, GW detection with high significance. In this analysis, we use a method for parameter estimation of a SGWB background. We seek to address the question of how well we can fit the model parameters. As a concrete example, we show the recovery of parameters from the MDSC injection sets using both a power-law, α , and CBC model. We show how to estimate parameters such as a SGWB amplitude and the CBC coalescence rate. To do so, we use a method presented in [102], that introduced a maximum likelihood technique to simultaneously estimate multiple parameters of SGWB models using CC data from pairs of GW detectors. This technique was used on recent results from LIGO to produce the first simultaneous limits on multiple parameters for power-law and CBC models of the SGWB, and to estimate the sensitivity of second-generation GW detectors to these models.

The likelihood function is defined as

$$L(\hat{Y}_i, \hat{\sigma} | \vec{\theta}) \propto \exp \left[-\frac{1}{2} \sum_i \frac{(\hat{Y}_i - \Omega_M(f_i; \vec{\theta}))^2}{\sigma_i^2} \right], \quad (4.24)$$

where $\Omega_M(f_i; \vec{\theta})$ is the template spectrum that we are trying to fit by varying the parameters θ , the sum runs over frequency bins f_i , which we set to be 0.25Hz, and \hat{Y}_i and σ_i^2 are the estimator and variance in the frequency bin i . The two methods, one a stochastic template-based analysis and the other a CC analysis, are very similar. Traditional SGWB cross-correlation searches have adopted a particular power-law model, assuming a specific spectral index value and searching over the spectral amplitude. The template-based maximum-likelihood estimator instead generically

incorporates any model for the purposes of both detection and parameter estimation. Therefore, it may be particularly useful for compact binary backgrounds.

4.4.1 SGWB Models

The amplitude and the frequency dependence of the SGWB spectrum depend on the physics of the model that generated it. For example, in the CBC model, the spectrum is determined by the coalescence rate of binary systems throughout the universe and by the distribution of their chirp masses. Past SGWB searches, performed using data from the initial LIGO and Virgo detectors [58, 59, 119], assumed a power-law model (see Eq. (4.23)) and set limits only on the amplitude Ω_{ref} for fixed values of the spectral index α and of the reference frequency f_{ref} . This is reasonable as most SGWB models predict a power-law dependence in the LIGO-Virgo frequency band.

As discussed above, compact binary coalescences are among the most promising sources of gravitational waves for ground-based gravitational-wave detectors. While detections of individual compact binaries are possible, another possibility is the detection of contributions from all CBCs in the universe to a SGWB. The model we use is the average version of Eq. (4.17) where the discrete sum over the sources is replaced by an integral over the redshift, masses, sky position, inclination angle and ψ . It was shown in [102] that it was sufficient to use only the average chirp mass \mathcal{M} to determine the spectrum. The model then consists of \mathcal{M} and the rate of coalescence events.

4.5 Results

We now present the results from our analyses of the various mock data sets. We first discuss the results from the analysis of the Gaussian noise data (data set 0), which we consider to be an ideal case. We compare these against the results from the re-coloured noise which can be considered as a more realistic case. We then detail the results from the simulation of the observing scenario. Finally we show the results from the parameter estimation.

The results of the Gaussian and re-coloured data sets, where we use the same set of injections for both, are reported in Table 4.3. The first column lists the three detector pairs as well as the combined results which is the weighted sum of the three pairs where the combined point estimate is calculated using

$$Y_{\text{combined}} = \frac{\sum_{AB} Y_{AB} \sigma_{AB}^{-2}}{\sum_{AB} \sigma_{AB}^{-2}}, \quad (4.25)$$

where AB run over the three possible detector pairs and the combined error is given by

$$\sigma_{\text{combined}}^{-2} = \sum_{AB} \sigma_{AB}^{-2}. \quad (4.26)$$

TABLE 4.3: Results from all mock data sets. The first column indicates the detector pair used in the analysis. The second column gives the estimated value of Ω_α from the Gaussian data sets. The third column gives the error on the measurement from the Gaussian data sets. The fourth column gives the SNR of the detection from the Gaussian data sets. The fifth column gives the estimated value of Ω_α from the re-coloured data sets. The sixth column gives the error on the measurement from the re-coloured data sets. These are all nearly identical across the data sets because the contributions of signal to the overall noise background are minimal (of order 0.1% when compared to the instrumental noise). This was verified by performing the same analysis on a small subset of the data but containing only signal. The final column gives the SNR of the detection from the re-coloured data sets. Here negative SNR values arise when the point estimate is negative. The table is divided by horizontal rows for the various data set with the injected value of Ω_α , as calculated by Eq. (4.17), also given.

Detector Pair	Point Estimate	Error	SNR	Point Estimate	Error	SNR
	Gaussian			Re-coloured Noise		
Set 0 (Noise only): $\Omega_\alpha = 0$						
HL	-8.093×10^{-10}	1.473×10^{-9}	-0.55	-1.119×10^{-9}	1.683×10^{-9}	-0.66
HV	-1.04×10^{-8}	1.139×10^{-8}	-0.91	-1.12×10^{-8}	1.407×10^{-8}	-0.8
LV	-1.47×10^{-9}	1.042×10^{-8}	-0.14	-1.765×10^{-9}	1.38×10^{-8}	-0.13
Combined	-9.769×10^{-10}	1.447×10^{-9}	-0.68	-1.268×10^{-9}	1.659×10^{-9}	-0.76
Set 1 (BNS): $\Omega_\alpha = 1.364 \times 10^{-8}$						
HL	1.512×10^{-8}	1.474×10^{-9}	10.26	1.455×10^{-8}	1.683×10^{-9}	8.65
HV	7.706×10^{-9}	1.139×10^{-8}	0.68	-9.858×10^{-9}	1.235×10^{-8}	-0.8
LV	5.491×10^{-9}	1.042×10^{-8}	0.53	7.451×10^{-9}	1.235×10^{-8}	0.6
Combined	1.481×10^{-8}	1.448×10^{-9}	10.23	1.399×10^{-8}	1.653×10^{-9}	8.46
Set 2 (BNS): $\Omega_\alpha = 1.411 \times 10^{-8}$						
HL	1.573×10^{-8}	1.474×10^{-9}	10.68	1.601×10^{-8}	1.69×10^{-9}	9.47
HV	7.713×10^{-9}	1.139×10^{-8}	0.68	-6.738×10^{-9}	1.24×10^{-8}	-0.54
LV	5.854×10^{-9}	1.042×10^{-8}	0.56	1.131×10^{-9}	1.24×10^{-8}	0.09
Combined	1.541×10^{-8}	1.447×10^{-9}	10.65	1.533×10^{-8}	1.659×10^{-9}	9.24
Set 3 (BBH): $\Omega_\alpha = 6.975 \times 10^{-9}$						
HL	5.175×10^{-9}	1.474×10^{-9}	3.51	4.725×10^{-9}	1.683×10^{-9}	2.81
HV	4.257×10^{-9}	1.139×10^{-8}	0.37	-6.117×10^{-9}	1.407×10^{-8}	-0.43
LV	1.763×10^{-9}	1.042×10^{-8}	0.17	3.968×10^{-9}	1.379×10^{-8}	-0.29
Combined	5.094×10^{-9}	1.447×10^{-9}	3.52	4.448×10^{-9}	1.659×10^{-9}	2.68
Set 4 (BNS+BBH): $\Omega_\alpha = 2.022 \times 10^{-8}$						
HL	2.056×10^{-8}	1.474×10^{-9}	13.94	1.991×10^{-8}	1.684×10^{-9}	11.83
HV	9.674×10^{-9}	1.139×10^{-8}	0.85	6.452×10^{-9}	1.352×10^{-8}	0.48
LV	7.211×10^{-9}	1.042×10^{-8}	0.69	1.777×10^{-8}	1.328×10^{-8}	1.34
Combined	2.012×10^{-8}	1.448×10^{-9}	13.9	1.968×10^{-8}	1.658×10^{-9}	11.87
Observing scenario: $\Omega_\alpha = 2.756 \times 10^{-9}$						
HL	3.581×10^{-9}	6.869×10^{-10}	5.21	—	—	—
HV	9.413×10^{-10}	6.207×10^{-9}	0.15	—	—	—
LV	4.235×10^{-10}	5.723×10^{-9}	0.07	—	—	—
Combined	3.505×10^{-9}	6.779×10^{-10}	5.17	—	—	—

The second, third and fourth columns give the estimated GW energy density, the error on this estimate and the SNR of the measurement for the data sets using Gaussian noise. The fifth, six and seventh columns give the corresponding results for the data sets using re-coloured noise. We use a 3σ measurement as the threshold at which to state that there is possible evidence for a SGWB signal, which is equivalent to an SNR = 3, as defined in Eq. (4.22). This equates to a false alarm probability of 0.27% and is true for both Gaussian and non-Gaussian noise because the point estimate, derived from a large sum, behaves as a Gaussian statistic [58].

4.5.1 Gaussian

The results from the analysis of all the Gaussian data sets are presented in the left-hand section of Table 4.3. The first results we highlight are from data set 0, which is our control set as it consists of just independent Gaussian noise. The measurement of Ω_α for the three detector pairs and the combined result give very low estimates and are the results of statistical fluctuations in the Gaussian data. The main result from this data set is the measurement of the error which we note is consistent with the error measurements of each of the other Gaussian noise data sets.

Data sets 1 and 2, where we only consider a population of BNS with a high merger rate, were designed to test how much bias is added to the measurements of Ω_α when we neglect to remove the loud detectable signals from the data streams² compared to when we only use sub-threshold signals. By keeping the detectable events, we also increase Ω_α , as indicated in Table 4.3. We find that in both cases we are able to measure the background estimate to within 1σ of the true value, as well as obtaining similar SNRs, both greater than 10.

With data set 3, where we consider a population of only BBH with a lower merger rate than before, we find that we are still able to find possible evidence for a SGWB with an SNR = 3.52. This also gives the largest error in the measurement of Ω_α with a measured value 1.3σ away from the true value. These results show that the estimation of Ω_α is still possible given a non-continuous GW signal (see middle plot of Fig. 4.3).

Data set 4, which is the combination of data set 1 and data set 3, gives a measured Ω_α spectrum equal to the sum of the results from data sets 1 and 3. A plot of the results for the three detector pairs, as well as the combined results, are shown in the left-hand plot of Fig. 4.5, where the measured values Ω_α are plotted in blue along with their respective error bars. Here the red dashed line shows the true value of Ω_α . We see here that we are able to recover the value of Ω_α to within 1.6% with the HL detector pair and 0.5% when we consider the combined results. This is likely due to the very high SNR of 13.9.

4.5.2 Re-coloured

The re-coloured data consists of the re-coloured initial LIGO and Virgo detector noise combined with the same data sets signal as for the Gaussian case. This analysis more closely simulates the likely output from the advanced detectors, which will suffer from various environmental noise sources contaminating the data. The results from the analysis of all the re-coloured data sets are presented in the right-hand section of Table 4.3 (next to the Gaussian results for easy comparison). As in the case of the Gaussian data set, set 0 contains only noise and serves as a baseline for the analysis. It has a combined point estimate well within 1σ of 0. The results for data sets 1 and 2 are also consistent with the Gaussian sets. The SNR for these sets are about 20% lower than that of the Gaussian set, which is due to the non-Gaussian noise transients. They are also within 1σ of the true values. Data set 3 and 4 show similar effects to data set 2,

²In this MDSC we can choose to simply not include any individually detectable signals within the data streams. In reality, removing detected signals from the data streams is very difficult as there may be some inaccuracy in measuring its true parameter used to produce the waveform which would leave some residual signal. Instead, we simply do not analyse the data that is known to contain the signal in the frequency band that we are searching.

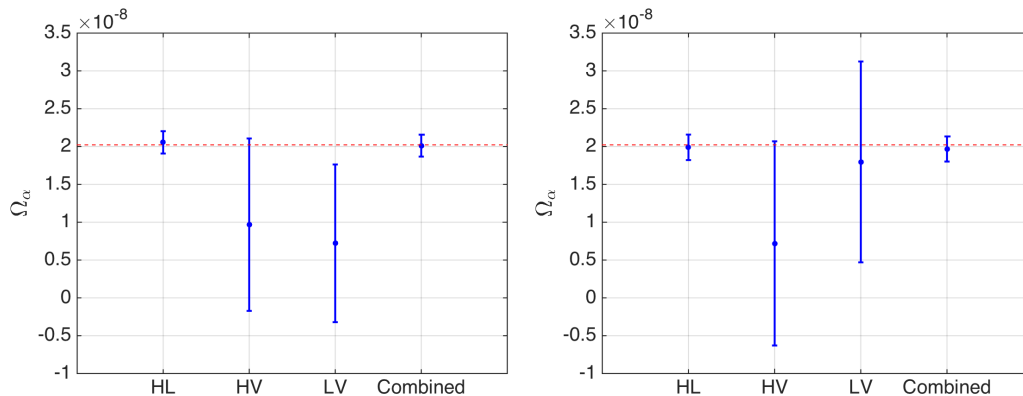


FIGURE 4.5: *Left*— Results for the year-long data set 4 with Gaussian noise where we show the measured value of Ω_α with error bars included for each of the detector pairs as well as the combined result of the weighted sum of the three detector pairs. The horizontal red dashed line shows the true injected value of $\Omega_\alpha = 2.022 \times 10^{-8}$ for this data set. *Right*— Results for the year-long set 4 with re-coloured noise where we show the measured value of Ω_α with error bars included for each of the detector pairs as well as the combined result of the weighted sum of the three detector pairs. The horizontal red dashed line shows the true injected value of $\Omega_\alpha = 2.022 \times 10^{-8}$ for this data set.

with a lower SNR than in the Gaussian case and with a recovered value of Ω_α within 1.6σ of the true values for data set 3 and within 1σ for data set 4.

4.5.3 Observing Scenario

We report the results from the observing scenario where we consider evolution of the detector sensitivities during different observational runs, the results of which are shown in Fig. 4.6. In the left-hand plot we show the measured value of Ω_α as a function of observation time with error bars included. The black dashed lines represent the start/end of each phase as detailed in Section 4.2.2 and the red dashed line represents the true injected Ω_α value while the solid black horizontal line represents $\Omega_\alpha = 0$. In the right hand plot we show the combined SNR as a function of time for the same points in the left-hand plot, as well as the theoretical SNR given by Eq. (4.22) using the blue dashed line. Here again the vertical black dashed lines show the start/end of each phase and the red dashed line indicates $\text{SNR} = 3$ which we use as the threshold value for finding possible evidence for a SGWB.

The first result to note is that over the course of the whole 5.5 years of the observing run the size of the error bars reduces significantly. By the end of the first 1.5 years of observations they have already reduced by over an order of magnitude. The second result to note is that already after the first 1.5 years of observation, we will observe disagreement with the null result at 95% confidence (2σ). The third result, which is in agreement with the theoretical model, is that we may be able to find possible evidence for a SGWB with an $\text{SNR} \geq 3$ after a period of about 3.5 years. At the end of the 5.5 year observing run, for this coalescence rate, we report that we have a total SNR of 5.15. We note that, in the right-hand plot of Fig. 4.6, the measured SNR (0.95) for the end of the second phase is well above what is predicted by the theoretical model (SNR = 0.35), although it is still within the 1σ range. This is explained by the larger than average

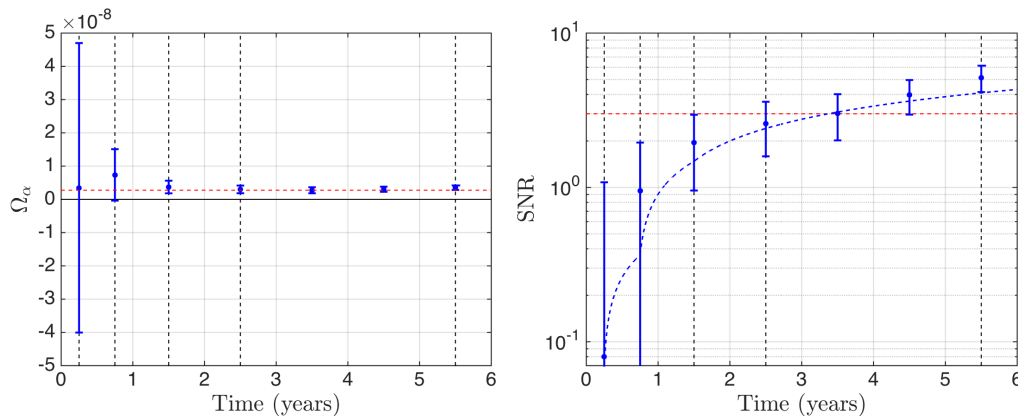


FIGURE 4.6: *Left*— Combined results for the estimated value of Ω_α as a function of time for the 5.5 long year observing scenario. The black dashed lines show the end point of each observing run, the red dashed line is the true injected value of $\Omega_\alpha = 2.756 \times 10^{-9}$, the horizontal black solid line is $\Omega_\alpha = 0$ and the blue points are the measured Ω_α values with their error bars. *Right*— Combined results for the measured SNR as a function of time for the 5.5 year long observing scenario. The black dashed lines show the end point of each observing run, the red dashed line represents $\text{SNR} = 3$, which we use as a threshold for the possible evidence of a SGWB, the blue dashed line shows the theoretical SNR as a function of time given by Eq. (4.22) and the blue points are the combined SNRs corresponding 1σ error bars.

measurement of Ω_α at the end of the second phase, as shown in the left-hand plot of Fig. 4.6, which, whilst being significantly larger than other measurements, is still within 1σ of the true value.

4.5.4 Parameter Estimation

In order to construct parameter posterior distributions, we use models for $\Omega_M(f_i; \vec{\theta})$ for various sets of waveform parameters. We use a power-law and compact binary model for $\Omega_M(f_i; \vec{\theta})$. Eq. (4.24) is evaluated repeatedly for each set of parameters and is maximized for those parameters that best fit the data. Parameter posterior distributions are constructed for parameter sets of equal likelihood. Example posteriors are shown in Fig. 4.7 for the power-law and CBC models. Table 4.4 shows results for all of the injection sets. We provide parameter estimates for the power-law model where, for CBC systems, the power-law index is $\alpha = 2/3$. We also provide parameter estimates and the true values for the CBC model. The constraints on the CBC background are relatively weak and highly dependent on the mass of the system (see the right hand plot of Fig. 4.7). Therefore, the limits we place on chirp mass and coalescence rate are in terms of bounds on the parameters. The bounds we place are consistent with the injected parameter values. We tested the case where we consider multiple CBC models, as was used to produce data set 4, and found that the posteriors are broadened by a significant amount.

4.6 Conclusion

In this SGWB MDSC for the advanced detectors, LIGO and Virgo, we have presented our methods for the productions and analysis of multiple mock data sets, as well as the results and

TABLE 4.4: Parameter estimation results for the various data sets. We provide the 99% confidence limits for both the power-law and CBC models, as well as the injected parameters. The first column indicates the data set. The second column is the estimated amplitude of Ω_α . The third column is the estimated power-law of the signal. The fourth and fifth columns gives the injected values of the amplitude and power-law. The sixth column give the estimated average chirp mass. The seventh column gives the estimated rate of events. The eighth and ninth columns gives the injected values of the average chirp mass and rate of events.

Data Set	Ω_α	α	True Ω_α	True α	\mathcal{M}	Rate	True \mathcal{M}	True Rate
Set 1	$[4.0 \times 10^{-10}, 4.0 \times 10^{-8}]$	$[-0.3, 1.6]$	1.5×10^{-8}	0.65	≤ 23	≥ 1.0	1.22	10
Set 2	$[4.0 \times 10^{-9}, 4.0 \times 10^{-8}]$	$[-0.3, 1.6]$	1.5×10^{-8}	0.65	≤ 22	≥ 0.9	1.22	10
Set 3	$[1.0 \times 10^{-12}, 3.4 \times 10^{-8}]$	$[-4, 2]$	7.6×10^{-9}	0.73	≤ 100	≥ 0.04	8.7	0.3
Set 4	$[8.7 \times 10^{-9}, 4.8 \times 10^{-8}]$	$[0, 1.4]$	2.1×10^{-8}	0.68	≤ 19	≥ 1.6	1.37	10.2

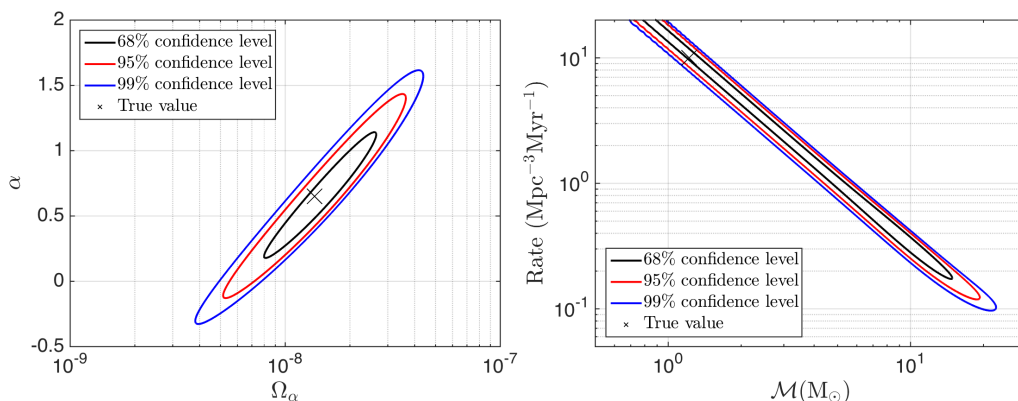


FIGURE 4.7: *Left*— The posteriors for amplitude, Ω_α , and its spectral index, α , for data set 1 with the 99% confidence level (blue), 95% confidence level (red) and 68% confidence level (black) shown. We show the true parameter values with an “X”. *Right*— The posteriors for average chirp mass, \mathcal{M} , and coalescence rate for data set 1 with the 99% confidence level (blue), 95% confidence level (red) and 68% confidence level (black) shown. We denote the correct CBC parameters by an “X”.

their scientific interpretation. We consistently find that the best results are obtained with the aLIGO detector pair (HL), compared to the aLIGO-AdVirgo pairs (HV, LV), though we still see some slight improvement when we consider the combined results from all detector pairs. This is in agreement with what we expect given the difference in sensitivities and orientations of the pairs. In the case of our three detector network, the two aLIGO detectors are the best aligned and have the smallest separation.

We have made comparisons between the use of Gaussian detector noise, which can be considered an idealistic case, and re-coloured noise data which is expected to be more realistic. We injected the same sources into both sets of noise to ensure that we are measuring the same signal. In both cases, we have been able to recover the injected value Ω_α to within 2σ using each data set.

From the analysis of the observing scenario data set we have shown that for the optimistic values of the CBC event rate the first deviation from the null result (at 95% confidence) may be observed as early as 1.5 years into the observation time. This assumes that we are able to achieve the designed sensitivities at the end of each observing phase, as outlined in Section 4.2.2,

and that the coalescence rate of CBC signals is significantly large as to make it detectable within a few years of operations at design sensitivity.

The results from data sets 1 and 3 have also shown that the theoretical prediction given in [62] holds true when applied to mock data. That is, the the statistical properties of the CBC GW signals, whether it be a continuous signal or more popcorn like, do not matter when we make a measurement of Ω_α ; all that is important is the total number of events that coalesce within the observational period and the GW energy spectrum emitted by each event.

Finally, we have shown that we are able to apply parameter estimation methods to the data in order to place confidence levels on different parameters. The detection of a stochastic signal will not be able to provide enough information by itself to place tight constraints on these parameters, but when considered in combination with detections of single events, it can become a very useful tool to explore the ensemble of sources from the whole universe [102].

The results from the estimation of the average chirp mass and coalescence rate also show that there is equal probability of having a high rate of events and low average mass as having a low rate of events and high average mass. In both cases the amplitude of the signal and the spectral index will be the same for the frequency range we search over, but in the first case the GW signals will be continuous while in the second case the GW signals will be highly non-Gaussian and popcorn like. The isotropic CC search we implement here is insensitive to two types of signals as it just considers the average strength of the signal over the observational period. In order to be able to differentiate these two signal types a non-Gaussian analysis must be developed that is able to search over both time and frequency [120].

Future MDSCs may wish to explore several areas that have not been covered here, such as, the inclusion of intermediate mass black holes (IMBH), which may have coalesced in the middle of the frequency search band, and therefore, given a high enough rate, may affect the analysis. Or, we could add a loud SGWB signal of cosmological origin that has a spectral index that differs from that of the astrophysical contribution. Another important question would be to investigate the behaviour of the CC analysis when correlated noise between different pairs of detectors is included in the mock data [116, 117] . The continuation of MDSCs will be an important part of the verification process for LIGO and Virgo when a SGWB is eventually observed.

Chapter 5

Second Einstein Telescope Mock Data and Science Challenge: Compact Binary Coalescence Data Analysis

Submitted to *Phys. Rev. D*

D. Meacher, K. Cannon, C. Hanna, T. Regimbau, B. S. Sathyaprakash

5.1 Introduction

Second generation gravitational-wave (GW) detectors, aLIGO [15] and AdVirgo [16], are planned to improve the sensitivity over first generation detectors, LIGO [11] and Virgo [12] by an order of magnitude. aLIGO has recently begun operations and AdVirgo is currently in the commissioning stage with plans to join operations in 2016. It is expected that the first direct detection of gravitational waves will be made before the end of this decade.

The Einstein Telescope (ET) is a conceived third generation gravitational-wave detector that is currently in the design stage [17] and is planned to be operational after ~ 2025 . This detector will have an improvement in sensitivity by an order of magnitude over that of the second generation detectors that will allow for the detection of a large number of GW signals from a variety of processes, out to large distances. These include, but are not limited to, events such as the formation of neutron stars or black holes from core collapse supernovae [40, 42, 43, 91], rotating neutron stars [65, 68], and the merger of compact binary systems [97, 98].

ET is expected to yield a significant number of detections and the interpretation of the results will allow us to answer questions about astrophysics, cosmology and fundamental interactions [121]. In order to prepare and test our ability to extract valuable information from the

data, we initiated a series of mock data and science challenges (MDSCs), with increasing degrees of sophistication and complexity with each subsequent challenge. These challenges consist of first simulating ET data that includes a population of sources expected to be detectable via different astrophysical models. This is then analysed with a variety of current data analysis algorithms, each searching for a specific signal type contained within the data. Unlike advanced detectors, ET data is expected to be dominated by many overlapping signals which increases the complexity of the data analysis. An important goal of the MDSC is to test the ability of different analysis algorithms in efficiently detecting signals and discriminating different signal populations. Finally we consider the interpretation of these results to investigate different areas of astrophysics and cosmology.

For the first ET MDSC [18], we produced one month of mock data containing simulated Gaussian coloured noise, produced using a plausible ET noise power spectral density (PSD), and the GW signal from a population of binary neutron stars (BNS) in the redshift range $z \in [0, 6]$. Using a modified version of the LIGO/Virgo data analysis pipeline `ihope` [53–56], which was the main matched filtering analysis pipeline during the initial detector era, we showed that it is possible to employ the use of a matched filtering algorithm to search for GW signals when there is a large amount of overlap of their waveforms. Using this pipeline we were also able to recover the observed chirp mass (\mathcal{M}_z) and observed total mass (M_z) of the injected signals with an error of less than 1% and 5% respectively¹. We also analysed the data with the standard isotropic cross-correlation statistic and measured the amplitude of an astrophysical stochastic GW background (SGWB) [28, 90, 100] created by the population of background BNS signals with an accuracy better than 5%. Finally, we were able to verify the existence of a *null stream*, created by the closed loop detector layout which results in the complete cancelling of GW signals and gives an acceptable estimate of the noise PSD of the detectors. By subtracting the null stream from the data, we showed that we could recover the typical shape of the PSD of the astrophysical SGWB.

After the success of the first challenge, we extended our data generation package to conduct a second MDSC. The second ET MDSC contains a larger selection of sources over that of the first, including BNS, neutron star-black holes (NSBH), binary black holes (BBH), intermediate mass black holes (IMBH) [122] as well as several burst sources. In the second MDSC we have taken the intrinsic mass distributions and time delays, the time between the formation and merger of the binary systems, from the population synthesis code `StarTrack` [111, 112, 123, 124], as opposed to selecting the component masses from a Gaussian distribution in the first MDSC. With this mock data set several investigations have been carried out, each investigating a different scientific aspect of the MDSC. The first of these investigations, on the measurement of a SGWB from astrophysical sources, has already been completed [103], while others are ongoing.

In this paper we investigate the application of a new low-latency matched filtering analysis pipeline, `gstlal` [125–128], which is built using `gststreamer` multimedia processing technology. The analysis will be run multiple times, searching for low mass systems, using a low frequency cut-off of 25Hz, 10Hz and 5Hz, on both the main mock data set as well as a noise only data set that is used to make estimates of the background. The 25Hz and 10Hz runs will be conducted

¹ The observed mass parameters, M_z and \mathcal{M}_z , differ from the intrinsic parameters, M and \mathcal{M} , by a factor of $(1+z)$, due to the redshifting of the GW frequencies from the expansion of the Universe, which is the equivalent of observing heavier masses. These are denoted with a subscript z , such that $\mathcal{M}_z \equiv \mathcal{M}(1+z)$.

on the full data set while the 5Hz analysis will be run on 10% of the data. This is due to the fact that starting at 5Hz, there are more templates produced for the analysis and the waveform for low mass systems will be of the order of a few hours long, both of which significantly increases the computational cost of the analysis.

Once the analyses have been run, we compare the list of detections that are reported in each of the three ET detectors against the list of injected signals. Using a small window in both coalescence time (t_c) and the observed (redshifted) chirp mass (\mathcal{M}_z) we produce a list of matched detections. We will then make a comparison of the recovered detection parameters (t_c , \mathcal{M}_z and M_z) against the true injected parameters.

The rest of this paper is divided into the following sections. In Section 5.2 we introduce the methods by which we produce the mock data used for this investigation. In Section 5.3 we discuss the analysis methods that are used as well as our reasons for choosing a new analysis pipeline. In Section 5.4 we present our results from the analysis runs that are conducted, with a focus on both event detection and parameter measurements. In Section 5.5 we highlight possible areas that can be investigated in future MDSCs. Finally in section 5.6 we discuss the results shown in the last section and make a conclusion to this investigation.

5.2 Mock Data

In this section we describe how we go about generating the ET mock data used in this investigation. Here we use the same data generation package as was used in the first ET MDSC [18], which has since been updated to simulate more sources [80, 103]. We first explain the generation of the coloured noise and then we introduce and describe each of the steps that are used to simulate the GW inspiral signals that are injected into the noise. For this we describe how the cosmological model and star formation rate (SFR) are used to determine the rate of coalescence of compact binary objects as a function of redshift and how the signal parameters are selected as well as the waveform models used in the simulation.

5.2.1 Simulation of the Noise

The current design of the Einstein Telescope is envisioned to consist of three independent V-shaped Michelson interferometers with 60 degree opening angles, arranged in a triangle configuration, and placed underground to reduce the influence of seismic noise [51, 52]. Here we make the assumption that there will be no instrumental or environmental correlated noise between the detectors so that the noise is simulated independently for each of the three ET detectors, E1, E2 and E3 [116, 117]. This is done by generating a Gaussian time series that has a mean of zero and unit variance. This time series is then Fourier transformed into the frequency domain, coloured with the noise PSD of the ET detector, and then inverse Fourier transformed back into the time domain. In order to remove any potential discontinuities between adjacent data segments, we gradually taper away the noise spectral density to zero at frequencies above 4096Hz and below 5Hz, which we set as the low frequency cut-off for the generation of the noise and GW signals.

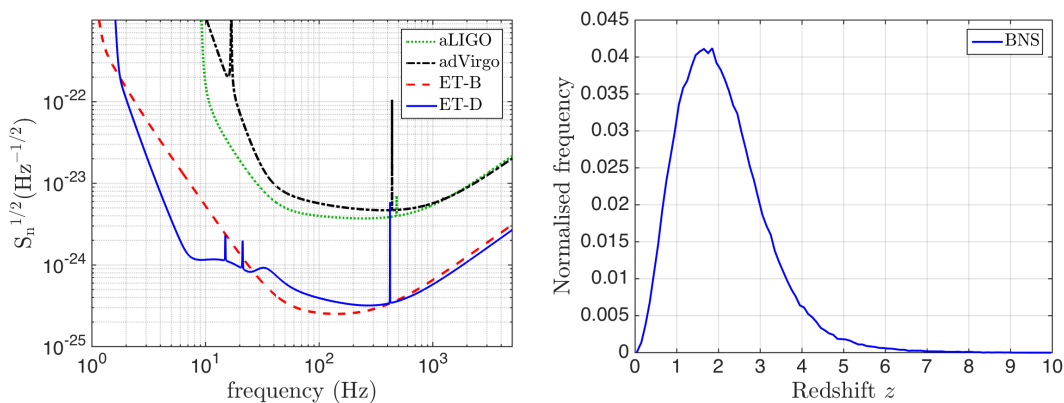


FIGURE 5.1: *Left*— Projected design noise power spectral density for advanced LIGO (dot-dot green), advanced Virgo (dot-dashed black), ET-B (dashed red) and ET-D (solid blue). *Right*— Normalised distribution of the redshift for all BNS events, using redshift bins of size $\Delta z = 0.1$, as provided by **StarTrack**.

For this MDSC, we consider the sensitivity given by ET-D rather than ET-B that was used in the first MDSC, as shown in the left-hand plot in Fig. 5.1.

5.2.2 Simulation of the GW signals from BNS

We employ the use of Monte Carlo (MC) simulation techniques for the generation of the mock data. The process that we use to generate the various parameters is very similar to that used in the first ET MDSC [18], except here we take the intrinsic mass distribution of the component masses, m_1 and m_2 , and the time delay, t_d , i.e. the interval between the formation of a binary and its eventual merger, from the stellar evolution code **StarTrack** [111, 112, 123, 124]. As was done in the first MDSC, we adopt a Λ CDM cosmological model with the Hubble parameter $H_0 = 70 \text{ km s}^{-1} \text{ Mpc}^{-1}$, $\Omega_m = 0.3$, and $\Omega_\Lambda = 0.7$ and the SFR of [110]. We first consider the merger rate for BNS per unit volume, as a function of redshift

$$\dot{\rho}_c(z, t_d) \propto \frac{\dot{\rho}_*(z_f(z, t_d))}{1 + z_f(z, t_d)}, \quad \text{with } \dot{\rho}_c(0) = \dot{\rho}_0, \quad (5.1)$$

where z is the redshift of the source at the point of coalescence, z_f is the redshift of the source at the point at which the binary formed, $\dot{\rho}_*$ is the SFR and $\dot{\rho}_0$ is the local coalescence rate. A factor of $(1 + z_f)^{-1}$ is used to convert the rate from the source's frame of reference to the observer's frame of reference.

The redshifts z and z_f are connected to each other via the delay time, t_d , which is the total time that it takes between the initial formation of the binary system, through its evolution into a compact binary and finally the merging time to the point of coalescence due to the emission of gravitational radiation using

$$t_d = \frac{1}{H_0} \int_z^{z_f} \frac{dz'}{(1 + z')E(\Omega, z')}, \quad (5.2)$$

where

$$E(\Omega, z) = \sqrt{\Omega_m(1+z)^3 + \Omega_\Lambda}. \quad (5.3)$$

The coalescence rate per redshift bin is given by

$$\frac{dR}{dz}(z, t_d) = \dot{\rho}_c(z, t_d) \frac{dV}{dz}(z), \quad (5.4)$$

where dV/dz is the comoving volume element given by

$$\frac{dV}{dz}(z) = 4\pi \frac{c}{H_0} \frac{r^2(z)}{E(\Omega, z)}, \quad (5.5)$$

where c is the speed of light in vacuum and $r(z)$, the proper distance, is given by

$$r(z) = \frac{c}{H_0} \int_0^z \frac{dz'}{E(z')}. \quad (5.6)$$

The merger rate, λ , which is the average time between events, is given by taking the inverse of the coalescence rate, Eq. (5.4), integrating over all redshifts

$$\lambda = \left[\int_0^{z_{\max}} \frac{dR}{dz}(z, t_d) dz \right]^{-1}. \quad (5.7)$$

Once we have a value for the average waiting time between events we then produce the parameters for each CBC source as follows:

- The arrival time, t_c , of injection i is selected assuming a Poisson distribution, where the difference in arrival time, $\tau = t_c^i - t_c^{i-1}$, is drawn from an exponential distribution $P(\tau) = \exp(-\tau/\lambda)$.
- The merger rate is set to $\lambda = 20 \text{ s}^{-2}$ which is comparable to the realistic rate given in [79]. This gives a total of 159,302 events which are split up into the following proportions: 80.47% BNS (128,244), 2% NSBH (3190), 12.46% BBH (19,766), provided from Table 3 in [101], and 5.07% IMBH (8102).
- The binary's component masses, m_1 and m_2 , shown in Fig. 5.2, and the time delay, t_d , are selected from a list of compact binaries generated by **StarTrack**. For the given delay time and a particular model for the cosmic SFR, we construct a redshift probability distribution, $p(z, t_d)$, by normalising the coalescence rate in the interval $z = [0, 10]$, where

²The original data sets as presented in [103] consisted of a year's worth of data that had an injection merger rate of $\lambda = 200 \text{ s}$, provided from Table 3 in [101] using the BZ model. In order to reduce the computational cost of running the analysis with a very low cut-off frequency we have reduced the amount of data by a factor of 10 while increasing the merger rate by the same factor. This means that the same injections are present within both sets while the time of arrival between successive events has decreased resulting in more overlap of the waveforms. It has already been shown in [18] that this overlap does not affect the ability of a matched filtering algorithm to detect overlapping signals.

$$p(z, t_d) = \lambda \frac{dR}{dz}(z, t_d). \quad (5.8)$$

In the right-hand plot of Fig. 5.1 we show the normalised redshift distribution for BNS, produced by using redshift bins of size $\Delta z = 0.1$.

- The sky position, $\hat{\Omega}$, the cosine of the inclination angle, ι , the polarization angle, ψ , and the phase at the coalescence, ϕ_0 , are selected from uniform distributions.
- The two GW polarisation amplitudes, $h_+(t)$ and $h_\times(t)$, and the antenna response functions to the two polarisations for each of the three ET detectors, $F_+^A(t, \hat{\Omega}, \psi)$ and $F_\times^A(t, \hat{\Omega}, \psi)$, where $A = 1, 2, 3$ is the index representing one of the three ET detectors, are then calculated. The detector responses

$$h^A(t) = F_+^A(t, \hat{\Omega}, \psi)h_+(t) + F_\times^A(t, \hat{\Omega}, \psi)h_\times(t), \quad (5.9)$$

are then added to the detector output time series for E1, E2 and E3, where the modulation of the signal due to the rotation of Earth is taken into account. In this MDSC we have chosen to use the TaylorT4 waveforms [115], which is accurate to 3.5 post-Newtonian order [129], in phase and the most dominant lowest post-Newtonian order term in amplitude, for the generation of the BNS and NSBH signals. For the BBH signals we choose the EOBNRv2 waveforms [130] that includes the merger and quasi-normal ring down phases of the signal, and it is accurate to 4th post Newtonian order in phase and lowest order in amplitude [115].

For the sake of testing and to determine the number of background detections we might expect to have, we have also produced a second, noise only data set that is produced with the same Gaussian noise as the main data set.

5.3 Analysis

The analysis method used here to search for the CBC signals is generally the same as was used in the first MDSC though we are now using a newly developed pipeline, `gstlal`. This is a coincident analysis pipeline where the data streams from each of the separate detector's are analysed individually via matched filtering with the use of a large bank of templates. The template bank is produced using a TaylorF2 waveform [131], which is generated in the frequency domain to the second post Newtonian order and terminates at the frequency of the last stable circular orbit, where $f_{\text{lsc0}} \simeq \frac{c^3}{6^{3/2}\pi GM_z}$. This waveform generator is selected as it is relatively fast to generate (compared to the TaylorT4 waveform) and reduces the computational cost of the analysis which is performed in the frequency domain. The analysis produces a list of matched *triggers* that exceed a given SNR threshold, ρ_T ; each trigger is a list that contains the SNR and the parameters of the template that produced the trigger, such as the epoch of merger and component masses of the binary. These are then checked against triggers from the other two detectors for coincidence. Any double or triple coincident triggers that result from the same

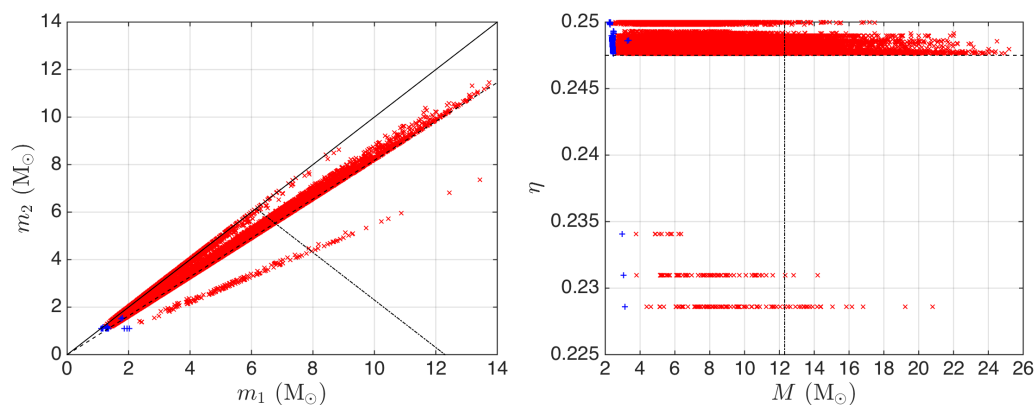


FIGURE 5.2: *Left*— Injected masses, m_1 and m_2 , where $m_1 \geq m_2$. The blue + are the intrinsic masses and the red \times are the observed (redshifted) masses, for 128244 BNS, as given by **StarTrack**. The diagonal solid black line represents equal masses with $\eta = 0.25$, where $\eta = m_1 m_2 / M^2$, the diagonal dashed line represents $\eta = 0.2475$, and the dot-dashed line represents a total mass of $12.3 M_\odot$. *Right*— Injected total mass, M , against symmetric mass ratio, η , where the blue + are the intrinsic values and the red \times are the observed (redshifted) values, for 128244 BNS, as given by **StarTrack**. The dashed horizontal line represents $\eta = 0.2475$ and the dot-dashed vertical line represents a total mass of $12.3 M_\odot$.

template are then reported as potential GW detections though in this investigation we only consider the results from triple coincident events.

5.3.1 Analysis stages

The different stages for this analysis pipeline are described here:

- Estimation of PSD: The `gstlal` analysis estimates the noise PSD as function of time during filtering. The method is a modified version of Welch’s method [132] with two main differences. First, each periodogram is derived from choosing the geometric mean of the last 7 periodograms and second, the periodograms are weighted averages that weigh the present periodogram slightly more than the past ones. The result is a PSD estimate with an effective average over a few hundred seconds with 1/16 Hz resolution.
- Generation of template bank: A bank of GW inspiral signals are produced that are used to search the data. This bank needs to cover the full mass parameter range that is being considered. Because we know the mass distributions of the signals being injected we are able to tailor the mass parameter limits that are used to generate the template banks in order to cover the full range of masses whilst keeping the number of templates produced to a minimum. A new template bank is generated for each search that is conducted, with the mass parameter ranges given in Table 5.1.
- Matched filtering: This is implemented with the LLOID (Low Latency Online Inspirational Detection) method, which uses singular value decomposition (SVD) to compress the waveform parameter space and multi-rate time domain filtering [127]. It provides the same result as standard matched filtering [133] to within $< 1\%$. The matched filtering of each SVD bank against each detector data stream produces an SNR time series $\rho(t)$.

TABLE 5.1: A list of all searches carried out in this investigation. The first column gives the identity of the search. The second column indicates if the analysis was run on the noise only or main data set. The third column gives the low frequency cut-off used for the analysis run. The fourth column gives the total length of the search in seconds. The fifth column gives the total mass range used for the search. The sixth column gives the symmetric mass ratio range used. The final column gives the total number of templates produced given the previous search parameters before the singular value decomposition is applied.

Search	Data	f_{\min} (Hz)	length (s)	M_{total} range (M_{\odot})	η range	$N_{\text{templates}}$
1	Noise + Signals	25	3072000	2.6 - 12.3	0.2475 - 0.25	3603
2	Noise + Signals	10	3072000	2.6 - 12.3	0.2475 - 0.25	25252
3	Noise + Signals	5	307200	2.6 - 12.3	0.2475 - 0.25	87054
4	Noise	25	3072000	2.6 - 12.3	0.2475 - 0.25	3647
5	Noise	10	3072000	2.6 - 12.3	0.2475 - 0.25	26173
6	Noise	5	307200	2.6 - 12.3	0.2475 - 0.25	89495

- Trigger generation: As templates are filtered against data streams, if any SNR time series passes a threshold value, ρ_T , then it is considered as a trigger. Here we set the single detector threshold to be $\text{SNR} = 4$.
- Coincidence between detectors: Triggers from different detectors are then compared against each other. Any that are coincident in time, within a 5 ms window to account for small time delays for the time of flight between detectors, and have the same masses, are considered as either double or triple coincident triggers. The SNR for a network of detectors is given by

$$\rho^2 = \sum_A \rho_A^2. \quad (5.10)$$

For triple coincident triggers this gives a minimum SNR of ~ 6.928 .

- Clustering of triggers: The list of double and triple coincident triggers is then clustered, where any coincident events that occur within a 4 second time window of a coincident events with a higher SNR are deleted. This is done as the same event will be detected by multiple templates, some with a certain degree of mismatch in the signal parameters. This results in the reporting of the best matched template.

The output of `gstlal`, containing all clustered triple coincident triggers, are then compared against the list of injections in order to “match” any potential detections. For this we apply a time and chirp mass window to each detection and if an injection is found within this two dimensional window then we determine it to be a found injection. If two Injections are found within the same two dimensional window then the injections with the smallest redshift is assumed to be the more likely event. The chirp mass is selected because, as was found in the first MDSC and as is shown later, it is better constrained than the total mass by the analysis. Here a time window of ± 100 ms and a chirp mass window of 1% of the observed chirp mass for BNS is used.

5.3.2 Searches

Compared to the standard advanced detector searches there are several differences that we implement here. The first is low frequency cut-off used to produce the signal templates. Advanced detector will only be sensitive down to $\sim 20\text{Hz}$ for the first couple of years of operations, eventually reduced to $\sim 10\text{Hz}$ when the detectors begin to operate at the design sensitivity [104]. Starting at these frequencies, low mass systems will have waveform lengths of only a few minutes to tens of minutes. When considering ET, which is sensitive down to frequencies as low as $1\text{-}3\text{Hz}$, depending on the final design configuration, signal templates can be of the order of hours to several days in length. In this investigation will focus on the application of different low frequency cut-offs where we run three searches using the same template mass range but using different f_{min} . We use a low frequency cut-off of 25Hz and 10Hz where we analyse the full mock data, and then analyse 10% of the data at 5Hz . We select one analysis run at 25Hz so that we can make a direct comparison to the results from the first MDSC and we choose to only analyse 10% of the data at 5Hz because of the high computational cost associated with this analysis. At this starting frequency with the injected masses shown in Fig. 5.2, the template waveform lengths are already several hours long. Because of this we also impose a cut-off at a redshift of $z = 0.2$, below which our search templates will not be sensitive. Instead we make the assumption that we have a detection efficiency of 100%. After this point, the signals are redshifted by a factor of $(1+z)$ by a significant fraction so that the signal wavelengths become computationally manageable. For these searches we set a minimum component mass of $1.3M_{\odot}$, minimum total mass of $2.6M_{\odot}$, a maximum component mass of $6.75M_{\odot}$ and a maximum total mass of $12.3M_{\odot}$ with a minimum symmetric mass ratio of $\eta = m_1m_2/M^2 = 0.2475$. This minimum symmetric mass ratio is chosen to be as high as possible to reduce the number of templates being generated whilst still including most of the population of BNS, as can be seen in the right-hand plot of Fig. 5.2. Already at this η_{min} we produce ~ 87000 templates when starting at 5Hz . All the search parameters are displayed in Table 5.1.

All three analysis runs are repeated on the noise only data sets in order to obtain an estimate on the number of background trigger one would expect in the main data set. From these results an SNR threshold value is set with which to make a cut on all trigger in the main data sets. For this we select the SNR equal to the 100th loudest events for the 25Hz and 10Hz runs, and the 10th loudest event for the 5Hz run. At present there is no method for determining an estimate for the false alarm probability with ET and so the 100th (10th) loudest noise event is selected as it will cover most of the population of background noise events whilst avoiding statistical fluctuations which produce louder SNR events that may skew the background estimate. The results of this are presented in Table 5.2.

5.4 Results

In this section we present the results from all the analysis runs carried out as part of this investigation, which is divided into four sub-sections. The first shows the number of detections made for each analysis run and the second details the detection efficiency. In the third we explore

TABLE 5.2: A list of the number of triggers and detections produced for different SNR threshold values used with each search. The first column gives the identity of the search. The second column gives the number of triggers produced when analysing the noise only data set. The third column give the SNR of the 100th loudest event obtained from the noise only data set. The fourth and fifth columns gives the total number of triggers and matched detections produced when no SNR threshold cut is applied. The sixth and seventh columns gives the total number of triggers and matched detections with an SNR larger than that of the 100th loudest event from the noise only data set. For the two right-hand columns the number in the brackets indicates the remaining percentage of triggers and detections compared to when the lowest SNR threshold cut is used.

Search	Noise		$\rho_T = 6.9$		$\rho_T = \text{SNR (100th loudest noise event)}$	
	N_{triggers}	SNR (100th loudest)	N_{triggers}	$N_{\text{detections}}$	N_{triggers}	$N_{\text{detections}}$
1	74323	8.655	82322	5708	5670 (6.89%)	4713 (82.57%)
2	291319	8.904	341747	9956	15590 (4.56%)	8138 (81.74%)
3	45183	8.964 ³	63709	1242	7320 (11.49%)	1095 (88.19%)

a proof of concept method for estimating the number of injected signals as a function of redshift and the fourth presents the accuracy with which we are able to recover the injection parameters.

5.4.1 *gstlal* analysis: Impact of the lower frequency cut-off on detection efficiency

The results for the different analysis runs with different low frequency cut-offs are summarized in Table 5.2. Here the first column gives the search identity, the second column gives the number of triggers that were produced when analysing the noise only data set, and the third column gives the SNR of the 100th (10th) loudest event. The fourth and fifth columns give the total number of triggers and resulting number of matched detections that are made with the smallest possible network SNR threshold of 6.9. The sixth and seventh columns again show the number of triggers and matched detections corresponding to an SNR threshold, ρ_T , equal to the 100th (10th) loudest event from the noise only data set. The number in the brackets for the two right-hand columns indicates the fractional number of triggers or matched detections that remain when a higher SNR threshold is used as compared to the case of smallest SNR threshold.

The results from these three analysis runs are shown in Fig. 5.3, where the SNR is plotted against the observed chirp mass. In each of the plots all the triple coincident triggers produced by *gstlal* when analysing the main data set are plotted in blue, with any of these triggers that are then matched to an injection being plotted in red and finally the triggers produced from the analysis of the noise only data set are plotted in green.

In the top plot we show the results from the 25Hz analysis where it is easy to distinguish a number of BNS signal detections from those of background events. There is a very clear peak of triggers with low chirp masses, implying small distances, with very high SNRs. The lower SNR events (i.e. $\text{SNR} \leq 10$) are harder to differentiate from the background events and its only by comparing them to the list of injections that we are able to identify them as true signal detections. There is a population of higher chirp mass, high SNR triggers that have not been matched to any BNS injections and clearly are not background events. These are in fact due

to the presence of GW signals from different types of CBC within the data, in this case the population of NSBH. This shows that the matched filtering method employed in this search is sensitive to CBC signal whose injection parameters lie outside of the search range. Even though these are not optimal matches, as we would expect the resulting SNR to be louder than what is shown here, they are still sufficiently loud enough to be considered as detected. In these cases one would expect the recovered parameters to differ greatly from the true parameters because of the search parameter limits used when generating these template banks. Finally we observe a large number of triggers (74,323) obtained from the noise only data set, spread across all chirp masses, with the loudest trigger having an SNR = 9.37 and the 100th loudest having an SNR = 8.566. These are all entirely caused by the random fluctuations in the Gaussian noise data and are labelled as background events.

In the middle plot we show the results from the 10Hz analysis. We first note here that there is a massive increase in the total number of triggers produced (341,747) which is related to the increase in the number of templates (25,252) produced for the 10Hz analysis runs compared to that of the 25Hz run (3603). Here we clearly see the population of BNS detections that have both higher SNRs and are detectable at higher observed chirp masses. We also note that there is a large reduction in the number of high chirp mass, high SNR unmatched detections from non-BNS signals than compared to the 25Hz analysis. From the analysis of the noise only data set, the loudest background event has an SNR = 9.53 and the 100th loudest event has an SNR = 8.904.

In the bottom plot we show the results from the 5Hz analysis. Again we clearly see the population of BNS signals and we also find the number of non-BNS triggers is very small. We should also note that the number of templates has significantly increased again (87,054 templates) over that of the 10Hz analysis but we do not see as large an increase in the number of detections due to analysing only 10% of the data. We would expect to obtain ten times as many triggers and detections as given in Table 5.2, giving an estimate of $\sim 637,000$ triggers and ~ 12400 detections from this mock data set.

Finally we highlight the loudest BNS detections in each of the analysis runs on the main data set which are produced from the same event. Starting at 25Hz it is detected with an SNR = 98.22, at 10Hz it is detected with an SNR = 122.46 and at 5Hz it is detected with an SNR = 134.97. This gives a clear example of how, when analysing from lower frequencies, we are able to build up more SNR for each signal which also helps us to increase the total number of detections we are able to make.

5.4.2 Detection efficiency

The detection efficiency, as a function of redshift, for a given analysis is given by

$$\epsilon(z) = \frac{N_{\text{det}}(z)}{N_{\text{inj}}(z)}, \quad (5.11)$$

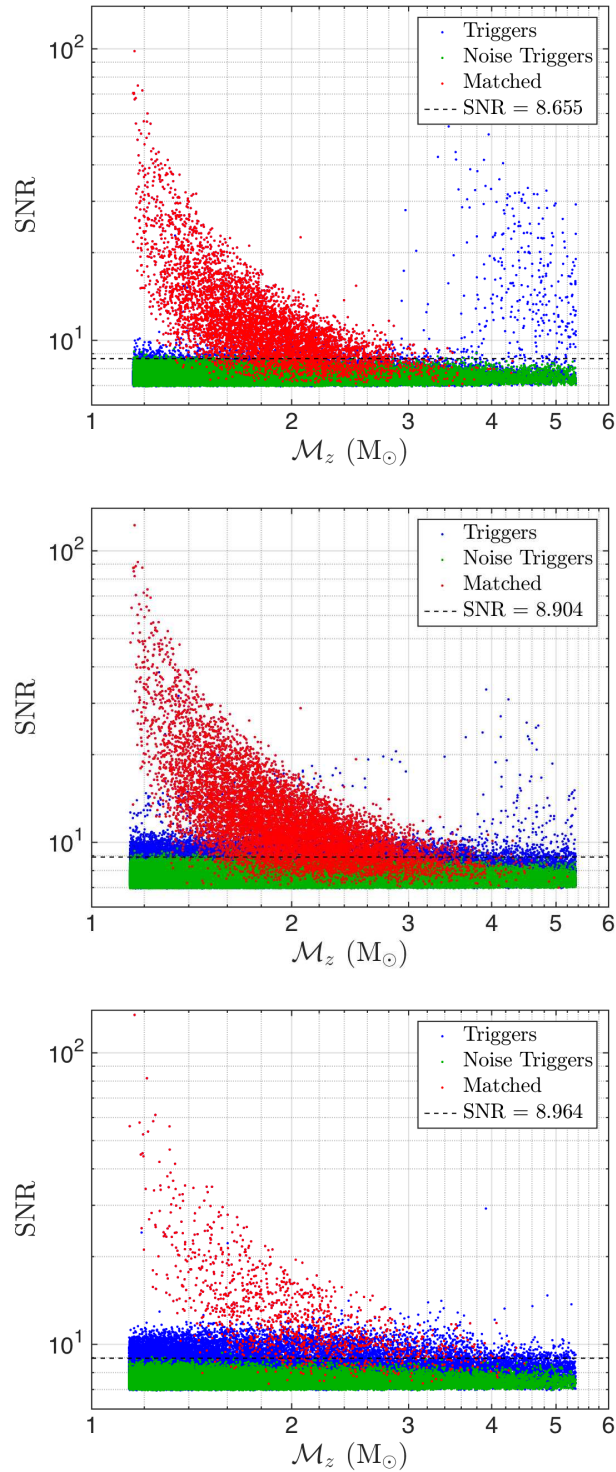


FIGURE 5.3: Scatter plots of SNR against the observed chirp mass for the three different low frequency cut-offs used in the analysis with 25Hz (top), 10Hz (middle) and 5Hz (bottom). All triggers produced from the analysis of the main data set are shown in blue, with the triggers produced from the analysis of the noise only data set shown in green. Any of the triggers from the main data set that are then matched to an injection are then plotted in red. Finally the dashed horizontal line represents an SNR equal to the 100th (10th) loudest trigger from the noise only data set.

where N_{det} is the number of detected injections per redshift bin, N_{inj} is the total number of injections per redshift bin and the variance is given by [134]

$$\sigma_{\epsilon}^2(z) = \frac{\epsilon(z)(1 - \epsilon(z))}{N_{\text{inj}}(z)}. \quad (5.12)$$

In the left-hand plot of Fig. 5.4 we show the smoothed detection efficiencies for each of the analysis runs carried, with the $\pm 1\sigma$ limits contained within the shaded region. Here we have only considered found injections that have an SNR greater than the threshold set by the 100th loudest event from the analysis of the noise only data set. We clearly see that by lowering the cut-off frequency of the analysis we are able to increase our detection efficiency across all redshift bins. This can be seen clearly by the fact that the efficiency at $z = 1$ doubles when going from 25Hz to 10Hz. It is also shown that the size of the uncertainty in the 5Hz efficiency is considerably larger than for the 25Hz or 10Hz as we are only considering 10% of the data and from Eq. (5.12) we see that this decreases with the inverse of the number of injections per redshift bin.

5.4.3 Rate estimation

In the previous subsection we make the assumption that we know the true number and distribution of all the injections in order to calculate the efficiency. If we consider the case where the number of signals in the Universe is unknown, then, by rearranging Eq. (5.11), it is possible to make an estimate of this by consideration of the number of detections as a function of redshift⁴ along with the detection efficiency, which can be determined from MC simulations with prior knowledge of the BNS mass distribution from the second generation of detectors [135]. In the right-hand plot of Fig 5.4 we show this estimate on the number of injections per redshift bin for each of the detection efficiencies calculated previously. Here the errors on the size of the efficiencies have been carried through. We clearly see that for each of the analysis runs there is an similar chance of estimating the number of events up to a redshift of $z \simeq 1.5$. Between the 25Hz (blue) and 10Hz (red) analysis runs, which were conducted on the full data set, there is a clear difference in the distance at which we are able to place an estimate on the number of injected signals, with the 25Hz extending to $z \sim 2$ and the 10Hz extending to $z \sim 3$. This is directly related to the detection efficiency presented in the previous subsection, with the size of the estimation increasing as the efficiency goes to zero. The 5Hz estimation appears to be larger than that of the 10Hz but this is a consequence of only analysing 10% of the data, which results in larger uncertainties in the efficiency and a smaller maximum redshift that an estimate can be made out too.

5.4.4 Impact of lower frequency cut-off on parameter estimation

In this subsection we present the errors we obtained in the measurement of the epoch of coalescence, and binary's chirp mass and total mass. We first look at the absolute error in the recorded

⁴We again make the assumption that we know the true redshift of the detection. In reality we would not know the detections true redshift though it is possible to derive estimates from various methods, detailed in Section 5.5.

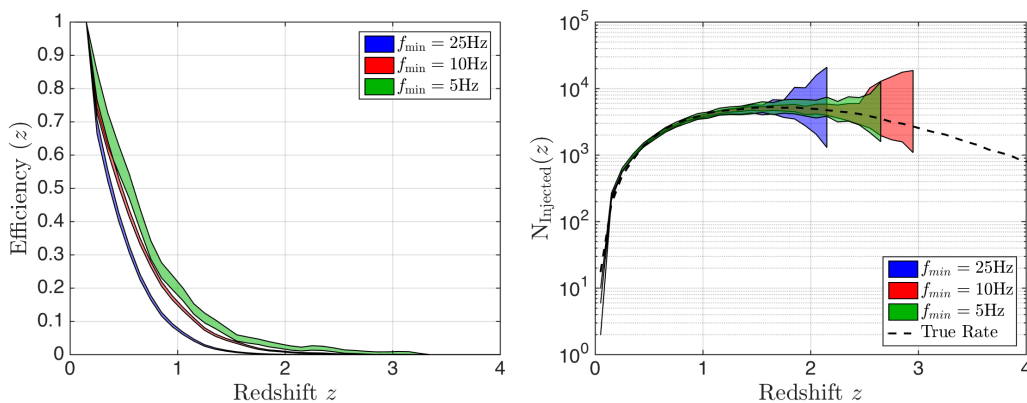


FIGURE 5.4: *Left*—Detection efficiency as a function of redshift for the 25Hz (blue), 10Hz (red) and 5Hz (green) analysis runs with the shaded areas representing the $\pm 1\sigma$ region, as given by Eq. (5.12). *Right*— Estimation of the number of injections as a function of redshift for the 25Hz (blue), 10Hz (red) and 5Hz (green) analysis runs with the shaded areas representing the $\pm 1\sigma$ region. The dashed black line represents the true number of injections, with redshift bins of size $\Delta z = 0.1$.

time of coalescence, given by $\Delta t_c = t_{c, \text{obs}} - t_{c, \text{inj}}$, followed by relative error in total mass, M_z , and chirp mass, \mathcal{M}_z ⁵. Table 5.3 lists the values of the mean and standard deviation for all the errors shown in this section.

5.4.4.1 Coalescence time

In this first MDSC, when matching triggers to injections, we considered a time window of $\pm 30\text{ms}$ while in this investigation, as stated above, we have increased this to $\pm 100\text{ms}$. In Fig. 5.5 we show a normalised plot of absolute error in measured coalescence time, t_c , of all the detections made when investigating the low frequency cut-off. We find that for all three BNS runs there is a constant bias of a few ms but nearly all detections are constrained very well to within $\pm 10\text{ms}$. This is due to the fact that both the injected waveform and the waveform used to search the data end at the same point, the f_{ISCO} . So the $\pm 30\text{ms}$ window considered for the first MDSC is suitable when considering BNS signals.

5.4.4.2 Masses

We now look at the errors in the measurements of the mass parameters. In Fig. 5.6 we show the impact of lowering the minimum search frequency.

In the top left-hand plot of Fig. 5.6 we show a normalised distribution of the relative error in measured total mass with the results from the 25Hz analysis shown in blue, the results from the 10Hz analysis shown in red and the results from the 5Hz analysis shown in green. We first note that the error has decreased by an order of magnitude when compared to the results from the first MDSC (see Fig. 7 of [18]). Also there is a constant systematic bias to generally underestimate the total mass for all three analysis runs, with a sudden drop off below 0.5%. The number of

⁵We note that in the case where we know exactly the redshift of the source, the relative error in the observed masses, M_z and \mathcal{M}_z , is mathematically identical to the relative error in the intrinsic masses, M and \mathcal{M} .

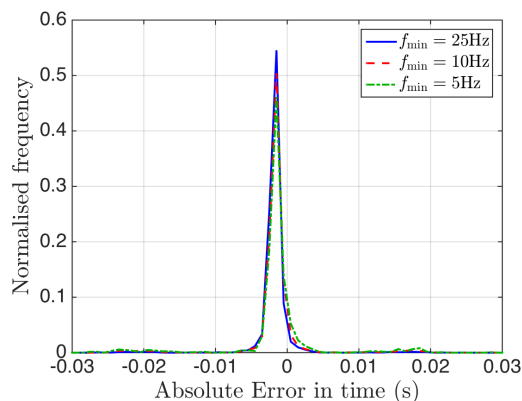


FIGURE 5.5: Normalised distribution of absolute error in recovered coalescence time for all matched detections given by `gstlal` for search 2 at 25Hz (solid blue), search 3 at 10Hz (dashed red), and search 4 at 5Hz (dot-dashed green), using time bins of size $\Delta t = 1$ ms, where different low frequency cut-offs were used.

events where the total mass is underestimated does decrease as the cut-off frequency for the analysis is lowered but this is only a small proportion. This bias was not observed in either the first MDSC or in any of our initial analysis runs where, in both cases, the component masses, m_1 and m_2 , were selected from the same distribution, which is not the case for this main mock data set.

In the top right-hand figure we plot the relative error in total mass against the observed total mass with the results from the 25Hz analysis shown in blue, the results from the 10Hz analysis shown in red and the results from the 5Hz analysis shown in green. We clearly see that sharp cut-off at the 0.5% shown in the previous plot. We also see that at lower observed masses, which correspond to closer distances, the spread of error measurements covers a range of values. At higher masses this distribution decreases leaving only the larger error measurements. This agrees with what we would expect, that our error measurements increase with distance.

In the bottom left-hand plot we show a normalised distribution of the relative error in measured chirp mass with the results from the 25Hz analysis shown in blue, the results from the 10Hz analysis shown in red and the results from the 5Hz analysis shown in green. We first note that the scale of the size of the distribution of the error has also decreased by a factor of ~ 10 when compared to the results from the first MDSC. Here we clearly see that as we decrease the cut-off frequency for the analysis we obtain a smaller distribution of the error of the chirp mass measurement. We can also see from Table 5.3 that the deviation of the mean of the distribution from zero goes from 0.01% at 25Hz to 0.001% at 5Hz which shows that we are able to recover the chirp mass to a very high degree of accuracy in this part of the analysis.

In the bottom right-hand figure we plot the relative error in chirp mass against the observed chirp mass with the results from the 25Hz analysis shown in blue, the results from the 10Hz analysis shown in red and the results from the 5Hz analysis shown in green. Here we clearly see that by decreasing the cut-off frequency we are able to better measure the chirp mass but also that the measured error on the chirp mass is related to the distance to the source.

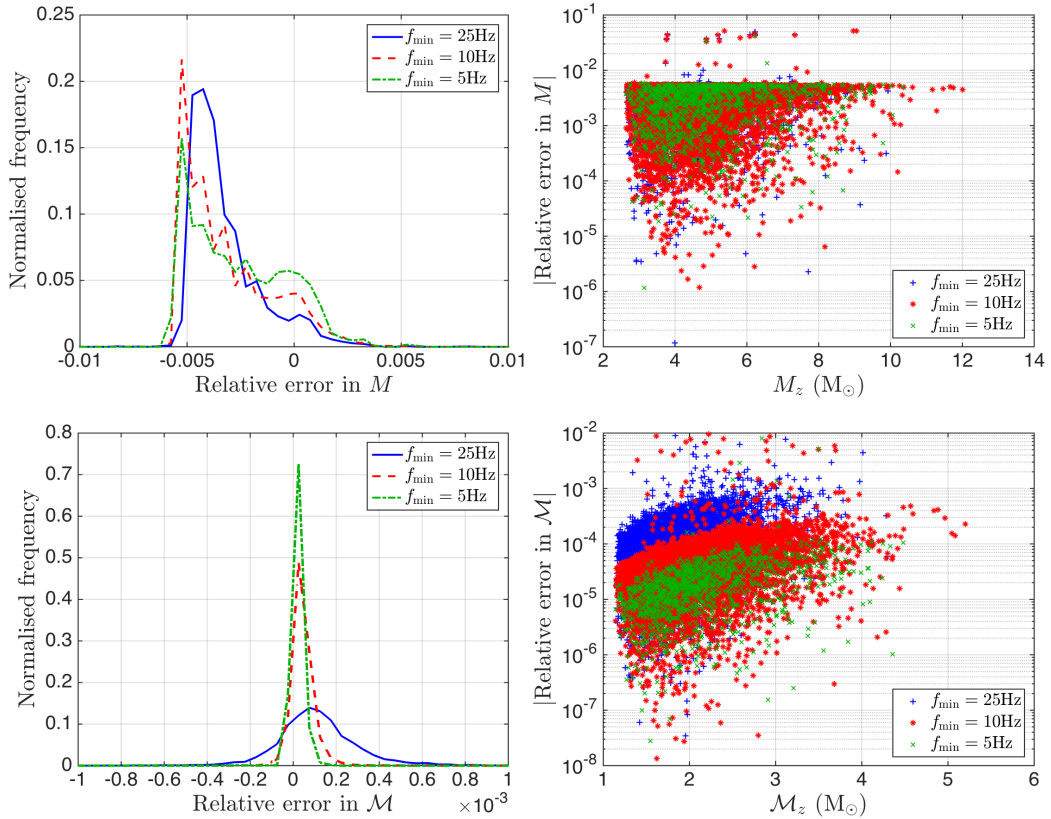


FIGURE 5.6: *Top left*— Normalised distribution of relative error in recovered total mass for search 2 at 25Hz (solid blue), search 3 at 10Hz (dashed red), and search 4 at 5Hz (dot-dashed green), using mass error bins of size $\Delta M = 5 \times 10^{-4}$. *Top right*— Scatter plot of relative error in total mass as a function of the observed total mass for search 2 at 25Hz (blue +), search 3 at 10Hz (red *), and search 4 at 5Hz (green ×). *Bottom left*— Normalised distribution of relative error in recovered chirp mass for search 2 at 25Hz (solid blue), search 3 at 10Hz (dashed red), and search 4 at 5Hz (dot-dashed green), using mass error bins of size $\Delta \mathcal{M} = 5 \times 10^{-5}$. *Bottom right*— Scatter plot of relative error in chirp mass as a function of the observed chirp mass for search 2 at 25Hz (blue +), search 3 at 10Hz (red *), and search 4 at 5Hz (green ×).

TABLE 5.3: Table showing the mean and standard distributions of the error in the measurements of injection parameters. The first column indicates which search it is. The second column gives the mean and standard distribution of the absolute error in measured coalescence time in milliseconds. The third column gives the mean and standard distribution of the relative error in the measurement of the total mass. The third column gives the mean and standard distribution of the relative error in the measurement of the chirp mass.

Search	Δt_c (ms)	Relative error M	Relative error \mathcal{M}
2 (25Hz)	-1.694 ± 3.314	$-3.301 \times 10^{-3} \pm 2.353 \times 10^{-3}$	$0.115 \times 10^{-3} \pm 0.369 \times 10^{-3}$
3 (10Hz)	-1.541 ± 5.307	$-3.213 \times 10^{-3} \pm 2.550 \times 10^{-3}$	$0.044 \times 10^{-3} \pm 0.286 \times 10^{-3}$
4 (5Hz)	-1.572 ± 5.856	$-2.674 \times 10^{-3} \pm 2.665 \times 10^{-3}$	$0.012 \times 10^{-3} \pm 0.289 \times 10^{-3}$

5.5 Future Development

Future MDSCs should aim to address increasing complexity of binary waveform models, improved detector noise models, simulating EM counterpart scenarios, and including other third generation detectors. There are still other GW sources that we can consider, consider, such as continuous waves [50] from rapidly rotating galactic neutron stars [136, 137]. The inclusion of one or more SGWBs of cosmological origins [89], such as phase transitions [86–88], cosmic (super) strings [36–38, 85, 138] or pre Big Bang models [82–84], would allow us to test whether we can distinguish between cosmological background and astrophysical backgrounds [48]. The waveform models that we choose to inject should also include additional features such as spin [139–141] and tidal affects [142–145], for BNS and NSBH, spin and precession [146, 147], for BBH and IMBH, and use a larger range of burst signal models. The inspiral waveforms should be generated down to even lower frequencies, such as 3Hz or 1Hz, to investigate if it is possible to push the low frequency cut-off used for the matched filtering past the 5Hz used here. At this frequency the low mass waveforms will be of the order of \sim hours to days long. These would allow for investigations into areas such as rate estimation, both the SFR and coalescence rate for various sources, measurement of the mass functions for NSBH and BBH, testing of general relativity, cosmological measurements, investigating different cosmological and astrophysical models and testing alternate theories of gravity.

When generating the data we should also include the two LIGO detectors with the use of the LIGO 3 Strawman PSD [148]. A smaller second data set should also be constructed with the use of re-coloured aLIGO noise (which we would expect to have at that point) into which we inject coherent signals. This will allow to study the behaviour of the null stream in the non-Gaussian case.

It is impossible to obtain a redshift measurement directly from a detection of a GW but it is possible to infer one through the use of an electromagnetic counterpart such as a sGRBs [149] or from an existing galaxy catalogue [150], or consideration of either the neutron star mass function [151], or EOS [152]. None of these methods have yet been applied within an MDSC, but some of them, such as using sGRBs, the neutron star mass function, or EOS, can easily be included within a future MDSC.

5.6 Conclusion

In this investigation we have described the generation and analysis of the data for the second Einstein Telescope mock data and science challenge with a focus on binary neutron stars. This data consisted of Gaussian noise, fitted to the expected ET-D sensitivity noise curve, into which a large number of GW signals from multiple sources are injected. The analysis was conducted with a new matched filtering pipeline that is able to analyse signals down to lower frequencies than has been considered before. Our motivation for this MDSC is to continue to explore the science potential of ET, increasing the complexity of the data analysis and science that is conducted with it.

The analysis used in this investigation has far surpassed that carried out in the first MDSC. One of the main goals for this investigation was to show that it is possible to analyse gravitational-wave inspiral signals down to a frequency of 5Hz. Starting at this frequency the lowest mass BNS systems being considered here take over two hours to coalesce. We have shown that, while being very computationally intensive/expensive, it is still possible to analyse data down to this frequency. If we consider that in the few years since the first MDSC we have been able to push the limit of the analysis comfortably from 25Hz to 10Hz and proven that 5Hz is achievable, we would like to think that in the next decade when the Einstein Telescope is hoped to be built, given Moore's law, it should be possible to push GW analysis to even lower frequency limits.

In the analysis at lower frequencies we have also shown the improvement we obtain in both detection efficiency and our ability to recover the injection parameters. By searching for signals with lower frequencies we are able build up more SNR which allows many more signals to become detectable as well as making the already detectable signals louder. The longer template waveforms also allow us to better match up with the GW signals, giving us better accuracy in the measurements of the parameters.

It has also been shown that analysing data at lower frequencies results in a higher rate of background detections being made with larger SNRs. Here we have just considered using an SNR threshold values that is equal to the 100th (10th) loudest background event from the analysis of the noise only data set, to reduce the number of background events but this has the drawback of reducing the number of true detections that are made as well. In the future it is hoped that a method will be developed that implements the null stream to reject background events, thus lowering the false alarm probability, allowing for a smaller SNR threshold to be used.

We have also shown the difference in detection efficiencies obtained when using lower cut-off frequencies. From these a proof of concept method has been shown where we attempt to estimate the number of injected signals as a function of redshift. This is a very basic method that makes several assumptions, mainly that we know the true redshifts of the detected signals. More work is required to further develop this method so that it is able to account for different parameters as well as a distribution on the redshift from the detections.

Finally we have also shown that our ability to measure mass parameters improved by an order of magnitude over that of the first MDSC in the case of BNS as a result of using a 5 Hz lower frequency cut-off instead of 25 Hz. We are able to recover the observed total mass to within 0.5% and the observed chirp mass to within 0.05%.

This work will now continue, were we investigate the parameter estimation for a small subset of the BNS detections.

Chapter 6

Second Einstein Telescope Mock Data and Science Challenge: Detection of the GW Stochastic Background from Compact Binary Coalescences

Phys. Rev. D 89. 084046. (2014) [103]

T. Regimbau, D. Meacher, M. Coughlin

6.1 Introduction

The first generation of gravitational-wave (GW) detectors such as LIGO or Virgo (2002-2013) were able to reach their design sensitivities, demonstrating the feasibility of the experiment. With the second generation, Advanced LIGO [15] and Advanced Virgo [16], expected to start collecting data in 2015, we will enter the era of the first GW detections. With a sensitivity about 10 times better than that of initial LIGO/Virgo, we expect the detection of a few or a few tens of compact binary coalescences (CBC) a year.

With the third generation European antenna Einstein Telescope (ET) [17, 51] planned to be operational in ~ 2025 , GW astronomy will definitely take a step further, with the possibility of detecting a large number of sources (up to $10^4 - 10^5$ CBC a year) from a large range of processes, such as core collapses to neutron stars or black holes [40, 42, 43, 91], rotating neutron stars [65, 68] including magnetars [66, 67, 92, 93], phase transition [94] or initial instabilities in young neutron stars [41, 95, 96] or compact binary mergers [47, 48, 97–99] (see [90] and references therein).

Besides the emission produced by the coalescence of the nearest binary systems, the superposition of a large number of unresolved sources at high redshifts will produce a background of gravitational waves [47, 48, 97–99] that may dominate over the cosmological background in the range 10–1000Hz where terrestrial detectors are the most sensitive. The detection of the cosmological background would provide very important constraints on the first instant of the Universe, up to the limits of the Planck era and the Big Bang, while the detection of the astrophysical background would provide crucial information about the star formation history, the mass range of neutron star or black hole progenitors and the rate of compact binary mergers.

The issue with ET will not be the detection but rather the estimation of the parameters and the interpretation of the results in term of astronomy, cosmology and fundamental physics. In order to get prepared and test our ability to extract valuable information from the data, we initiated a series of mock data and science challenges, with increasing degree of complexity.

For the first ET mock data and science challenge (ET MDSC1) [18], we produced one month of simulated data containing simulated gaussian colored noise and the GW signal from a simulated population of double neutron stars in the redshift range $z = 0 - 6$. Using a modified version of the LIGO/Virgo data analysis pipeline iHope [55], we were able to recover the intrinsic chirp mass and total mass distributions with an error of less than 1% and 5% respectively. We also analyzed the data with the standard isotropic cross-correlation (CC) statistic and measured the amplitude of the background with an accuracy better than 5%¹. Finally, one of our main result was to verify the existence of a null stream canceling the GW signal and giving a very precise estimate of the noise power spectral density (PSD). By subtracting the null stream from the data, we showed that we could recover the typical shape of the PSD of the GW signal.

After the success of the first challenge, we extended our data generation package and produced three new sets of data. The first one (ET MDSC2-a) contains all types of stellar compact binary coalescences, composed of two neutron stars (NS-NS), a black hole and a neutron star (BH-NS) or two black holes (BH-BH). The second data set (ET MDSC2-b) contains the population of CBC too faint to be detected individually and which creates a residual GW background. We assume here individual detections can be successfully subtracted from the data, as it has been done with success for the population of white dwarf binaries in the context of the LISA Mock Data Challenge, using Markov Chain Monte Carlo techniques [153]. The third data set (ET MDSC2-c) contains the same population of CBC as ET MDSC2-a, two supernovae and two f-modes, and also a population of intermediate-mass black hole binary coalescences and intermediate mass ratio inspiral, which could be quite numerous at low frequencies but whose existence has not been confirmed yet [122].

In this chapter we use the standard cross correlation statistic which is known to be optimal in the case of a Gaussian, isotropic stochastic background to search for the residual GW background in the second data set ET MDSC2-b. This analysis complements the search for individual CBC [80], as the majority of the sources contributing to the residual background are at redshift above the detection range. The paper will be organized as follow. In section 6.2 we present the CBC

¹Unlike initial LISA which was designed to be a single detector with three arms in a triangle configuration, ET will consist of three nested detectors (six independent arms in total) [17, 51], and one can use cross-correlation methods to extract GW stochastic backgrounds from the instrumental noise.

population model and summarize briefly the simulation procedure. In section 6.3 we discuss the spectral properties of the GW signal in the first and second data sets. In section 6.4 we present the results of the analysis. Section 6.5 contains a conclusion and suggestions for further research.

6.2 The second ET mock data

For each data set, we produced one year of data split into segments of length 2048 s. The data are sampled at 8192Hz and the minimal frequency was set to 5Hz (rather than 10Hz for ET MDSC1). The procedure to generate the simulated data is mostly the same as the one used for ET MDSC1 and is described in detail in [18]. The main steps are briefly summarized below.

6.2.1 Simulation of the Noise

The Einstein Telescope is envisioned to consist of three independent V-shaped Michelson interferometers with 60 degree opening angles, arranged in a triangle configuration, and placed underground to reduce the influence of seismic noise [51]. Assuming there is therefore no instrumental or environmental correlated noise², the noise was simulated independently for each of the three ET detectors E1, E2 and E3, by generating a Gaussian time series with a mean of zero and unit variance. This time series was then transformed into the frequency domain, colored with the noise PSD, and then inverse Fourier transformed. To alleviate the effects of any potential discontinuities across frame files, the noise curve was gradually tapered away to zero below f_{\min} , and above $f_{\text{Nyquist}}/2$. For ET MDSC2, we considered the sensitivity ET-D rather than ET-B for ET MDSC1 (see Fig. 6.1).

6.2.2 Simulation of the GW signal from CBC

The main improvement compared to the first ET-MDC is that we generated all types of binaries NS-NS, BH-NS and BH-BH, and did not select the source parameters from simple distributions but used the results of the sophisticated binary evolution code StarTrack [111, 112, 123, 124] that provides the masses of the two component m_1 and m_2 and the delay t_d from formation of the massive binary to final merger. Among their different models, we chose the nominal one [112] with solar metallicity, small kick velocity and pessimistic common envelop scenario.

To generate a population of compact binaries, we proceeded as follow for each source:

- Assuming a Poisson process, the time from the previous coalescence was drawn from an exponential distribution $P(\tau) = \exp(-\tau/\lambda)$. Taking the inverse of the merging rate integrated over all redshifts provided in Table 2 of [101], i.e. 154 929 per year for the nominal

²Even if the seismic noise will be significantly reduced in ET compared to LIGO or Virgo which are not underground, this assumption may not be realistic as the three ET detectors are nearly co-located. Techniques to identify non-gravitational-wave correlations between a pair of co-located detectors have been developed in the context of the two LIGO detectors at Hanford and could be extended to ET [154]. A more careful study of the effect of environmental noise will be included in future ET mock data and science challenges.

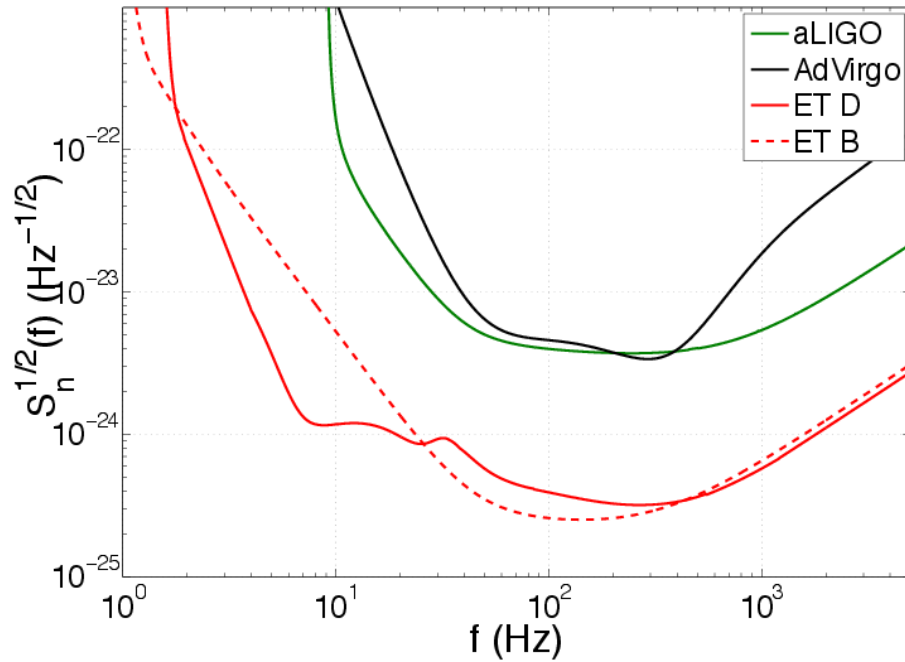


FIGURE 6.1: The sensitivity curve ET-B (dashed red line) used for the first ET MDSC and ET-D (continuous red line) used for the second ET MDSC. Advanced LIGO and Virgo noise curves are also shown for comparison.

model (model BZk), we obtained an average time interval $\lambda = 200$ s. We then selected the type of the binary using the proportion 84.78% of NS-NS, 2.09% of BH-NS and 13.13 % of BH-BH also provided in Table 2 of [101].

- The masses m_1 , m_2 , and the delay t_d were selected from a list of compact binaries generated by StarTrack. Given the delay and a model for the cosmic star formation rate, we constructed a probability distribution from which the redshift at coalescence z was randomly selected

$$p(z, t_d) \propto \frac{\dot{\rho}_*(z_f) dV}{1 + z_f} dz, \quad (6.1)$$

where z_f is the redshift of formation of the massive binary, $\dot{\rho}_*$ is the star formation rate and $\frac{dV}{dz}$ is the comoving volume element. The redshifts z_f and z are related by the delay time t_d which is the difference in lookback times between z_f and z . Following the first ET-MDC, we adopted the star formation rate of [110] and Lambda-CDM cosmology.

- The location in the sky $\hat{\Omega}$, the cosine of the orientation ι , the polarization ψ and the phase at the coalescence ϕ_0 were drawn from uniform distributions
- The two polarizations h_+ and h_\times , the antenna pattern functions of the three ET detectors F_+^j and F_\times^j ($j = 1, 2, 3$) were calculated, and then the responses $h^j(t) = F_+^j(t)h_+(t) + F_\times^j(t)h_\times(t)$ were added to the time series of E1, E2 and E3. In these simulations, we have used so-called TaylorT4 waveforms, up to 3.5 post-Newtonian order in phase and the most

dominant lowest post-Newtonian order term in amplitude for NS-NS and BH-NS, and the EOBNRv2 waveforms including merger and ring down from numerical relativity, up to 4 post-Newtonian order in phase and lowest order in amplitude for BH-BH [115].

6.3 Spectral properties

The superposition of the GW signal from sources at all redshifts and integrated over all directions of the sky create a background, whose spectrum is usually characterized by the dimensionless energy density parameter [28]

$$\Omega_{\text{gw}}(f) = \frac{1}{\rho_c} \frac{d\rho_{\text{gw}}}{d \ln f}, \quad (6.2)$$

where ρ_{gw} is the gravitational energy density and $\rho_c = \frac{3c^2 H_0^2}{8\pi G}$ is the critical energy density needed to make the Universe flat today. G is the Newtonian constant, c the speed of light and H_0 the Hubble constant. The GW spectrum from the population of extra-galactic binaries is given by the expression

$$\Omega_{\text{gw}}(f) = \frac{1}{\rho_c c} f F(f), \quad (6.3)$$

where $F(f)$ is the total flux and f is the observed frequency. The total flux (in erg Hz^{-1}) is the sum of the individual contributions

$$F(f) = T^{-1} \frac{\pi c^3}{2G} f^2 \sum_{k=1}^N (\tilde{h}_{+,k}^2 + \tilde{h}_{\times,k}^2), \quad (6.4)$$

where N is the number of coalescences in the data (the total number of CBC for ET MDSC2-a and the number of undetected sources forming the residual background for ET MDSC2-b). The normalization factor T^{-1} assures that the flux has the correct dimension, $T = 1$ yr being the length of the data sample.

In the Newtonian regime before the last stable circular orbit (LSCO) $f_{\text{lsc0}} \simeq \frac{c^3}{6^{3/2} \pi G M (1+z)}$, the Fourier transform of h_+ and h_\times are given by

$$\tilde{h}_+(f) = h_z \frac{(1 + \cos^2 \iota)}{2} f^{-7/6}, \quad (6.5)$$

$$\tilde{h}_\times(f) = h_z \cos \iota f^{-7/6}, \quad (6.6)$$

where

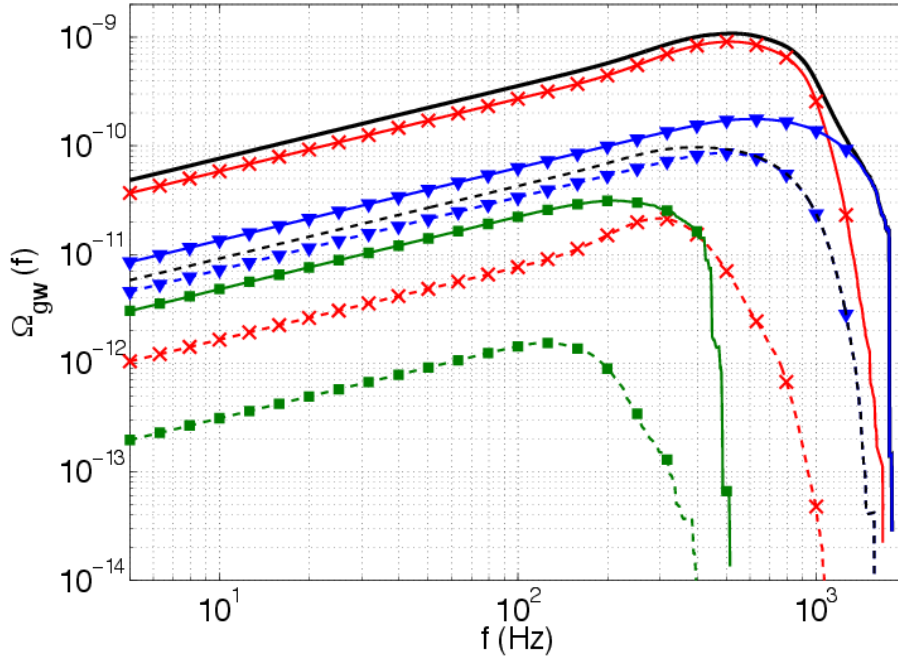


FIGURE 6.2: Ω_{gw} calculated from the list of CBC sources present in the first (continuous lines) and the second (dashed lines) data sets of ET MDC2, for NS-NS (blue triangles), NS-BH (green squares), BH-BH (red crosses) and the total (black line with no markers)

$$h_z = \sqrt{\frac{5}{24}} \frac{(GM(1+z))^{5/6}}{\pi^{2/3} c^{3/2} d_L(z)}, \quad (6.7)$$

and where $d_L(z)$ is the luminosity distance at redshift z , ι is the inclination angle, $M = m_1 + m_2$ the total mass, $\mathcal{M} = (m_1 m_2)^{3/5} M^{-1/5}$ the chirp mass. It gives for the energy density parameter

$$\Omega_{\text{gw}}(f) = \frac{5\pi^{2/3} G^{5/3} c^{5/3}}{18c^3 H_0^2} f^{2/3} \sum_{k=1}^N \frac{(1+z_k)^{5/3} (\mathcal{M}_k)^{5/3}}{d_L(z_k)^2} \left(\frac{(1+\cos^2 \iota_k)^2}{4} + \cos^2 \iota_k \right). \quad (6.8)$$

Fig. 6.2 shows Ω_{gw} calculated from the list of CBC sources present in the first (continuous lines) and the second (dashed lines) data sets of ET MDC2, for the different types of binaries and the total. All the curves present the same characteristic shape: a power law with index $2/3$ at low frequencies corresponding to the inspiral phase, a maximum and a sharp decrease. The BH-BH contribution includes also the merging and ring down phase with a larger power index, that extends after the LSCO.

For ET MDC2-a where all the sources are included, the background is dominated by the contribution from BH-BH ($\Omega_{\text{Ref}} = 2.7 \times 10^{-10}$ at $f_{\text{Ref}} = 100\text{Hz}$). The contribution from BH-NS is negligible due to the small rate ($\Omega_{\text{Ref}} = 2.2 \times 10^{-11}$). Even if NS-NS are the most numerous, they are less energetic than BH-BH, and their contribution ($\Omega_{\text{Ref}} = 6.3 \times 10^{-11}$) represents 17%

of the total background ($\Omega_{\text{Ref}} = 3.7 \times 10^{-10}$). For ET MDC2-b from which the sources detected individually have been subtracted, the total amplitude drops to $\Omega_{\text{Ref}} = 4.3 \times 10^{-11}$ and it is largely dominated by the contribution from NS-NS ($\Omega_{\text{Ref}} = 3.4 \times 10^{-11}$) which represents 79% of the total. The contribution from BH-BH, which are the loudest sources, is an order of magnitude below ($\Omega_{\text{Ref}} = 7.6 \times 10^{-12}$) and two order of magnitude below the BH-BH background in the first data set. The contribution from BH-NS is still negligible with $\Omega_{\text{Ref}} = 1.4 \times 10^{-12}$.

6.4 Stochastic Analysis

The strategy to search for a Gaussian (or continuous) background, which could be confused with the intrinsic noise of a single interferometer, is to cross-correlate measurements of pairs of detectors. When the background is assumed to be isotropic, unpolarized and stationary, the cross-correlation product of detectors i and j is given by [28]

$$Y = \int_0^\infty \tilde{s}_i^*(f) \tilde{s}_j(f) \tilde{Q}(f) df, \quad (6.9)$$

and the expected variance, which is dominated by the noise, by

$$\sigma_Y^2 \simeq \int_0^\infty P_i(f) P_j(f) |\tilde{Q}(f)|^2 df, \quad (6.10)$$

where

$$\tilde{Q}(f) \propto \frac{\gamma_{ij}(f) \Omega_{\text{gw}}(f)}{f^3 P_i(f) P_j(f)}, \quad (6.11)$$

is a filter that maximizes the signal-to-noise ratio,

$$\text{SNR} = \frac{3H_0^2}{4\pi^2} \sqrt{2T} \left[\int_0^\infty df \frac{\gamma_{ij}^2(f) \Omega_{\text{gw}}^2(f)}{f^6 P_i(f) P_j(f)} \right]^{1/2}. \quad (6.12)$$

In the above equations, P_i and P_j are the one-sided power spectral noise densities of the two detectors and γ_{ij} is the normalized isotropic overlap reduction function (ORF), characterizing the loss of sensitivity due to the separation and the relative orientation of the detectors for sources isotropically distributed in the sky [60, 155]

$$\gamma_{ij}(f) = \frac{5 \sin^2(\gamma)}{8\pi} \int d\hat{k} e^{i2\pi f \hat{k} \cdot \Delta \vec{x}_{ij}/c} (F_+^i F_+^j + F_\times^i F_\times^j), \quad (6.13)$$

where $\Delta \vec{x}_{ij}$ is the separation vector between the vertices of the two detectors and the product $\hat{k} \cdot \Delta \vec{x}_{ij}/c$ in the exponential, the time delay for a wave arriving from direction \hat{k} . The normalization ensures that $\gamma_{ij} = 1$ for co-located and co-aligned L-shaped detectors. For two V-shaped ($\alpha = \pi/3$) ET detectors separated by $\beta = 2\pi/3$ degrees and with $f\Delta t \ll 1$, $\gamma_{ij} = \sin^2(\alpha) \cos(2\beta) =$

$-3/8 = -0.375$. A recent paper [62] derived a general expression of the ORF, valid for any distribution in the parameter space of sources contributing to the background. For ET it writes :

$$\hat{\gamma}_{ij}(f) = \frac{3}{10} \frac{\sum_{n=1}^N h_{z,k}^2 F_{ij,k}}{N \left\langle h_z^2 \left(\frac{(1 + \cos^2 \iota)^2}{4} + \cos^2 \iota \right) \right\rangle}, \quad (6.14)$$

with

$$h_{z,k} = \sqrt{\frac{5}{24}} \frac{(GM_k(1+z_k))^{5/6}}{\pi^{2/3} c^{3/2} d_L(z_k)} \quad (6.15)$$

and

$$F_{ij,k} = \left[\begin{aligned} & \frac{(1 + \cos^2 \iota_k)^2}{4} F_{+,k}^i F_{+,k}^j + \cos^2 \iota_k F_{+,k}^i \times F_{\times,k}^j + \\ & \frac{(1 + \cos^2 \iota_k) \cos \iota_k}{2} \left(F_{+,k}^i F_{\times,k}^j + F_{\times,k}^i F_{+,k}^j \right) \end{aligned} \right], \quad (6.16)$$

$$\simeq \left[\frac{(1 + \cos^2 \iota_k)^2}{4} F_{+,k}^i F_{+,k}^j + \cos^2 \iota_k F_{\times,k}^i F_{\times,k}^j \right]. \quad (6.17)$$

The angle brackets $\langle \rangle$ in Eq. (6.14) indicate an average over all the sources present in the data, which means in the case of the residual background, all the CBC sources with a signal-to-noise ratio smaller than 8. For ET MDC2-b we obtain $\hat{\gamma}_{12}(f) = -0.283$, $\hat{\gamma}_{13}(f) = -0.284$ and $\hat{\gamma}_{23}(f) = -0.281$, so a factor of about 1.3 smaller than the isotropic value. When the detected sources are removed, there is a selection effect that affects the distribution of the parameters (in particular the isotropy and the uniform orientation). After the detector horizon (the maximal distance at which a source can be detected) all the sources contribute to the background, but at close redshifts, only poorly oriented or located sources contribute (see Fig. 6.3). This effect is not negligible and has to be corrected in order to avoid a systematic bias in the analysis. A priori the distribution of the sources in the parameter space is not known and neither the correction factor. However, for a narrow distribution of the masses (which is the case here since the background is largely dominated by the BNS population), it only depends on the distribution in redshift and the average chirp mass and one can easily obtain the expected value (in the limit $N \gg 1$) from the star formation rate. Doing this, we obtained a correction of ~ 1.25 , in agreement with our results for ET MDC2-b with a precision better than 4%.

We analyzed the data with the cross-correlation code developed by the LIGO stochastic group. The data were split into $N = 529067$ segments of length $T_{\text{seg}} = 60$ s, and for each segment the cross-correlation product and the theoretical variance were calculated using a template $\Omega_{\text{gw}} \sim f^{2/3}$ in the range 5 – 150Hz, where we have more than 99% of the SNR (see Fig. 6.4) [99, 101].

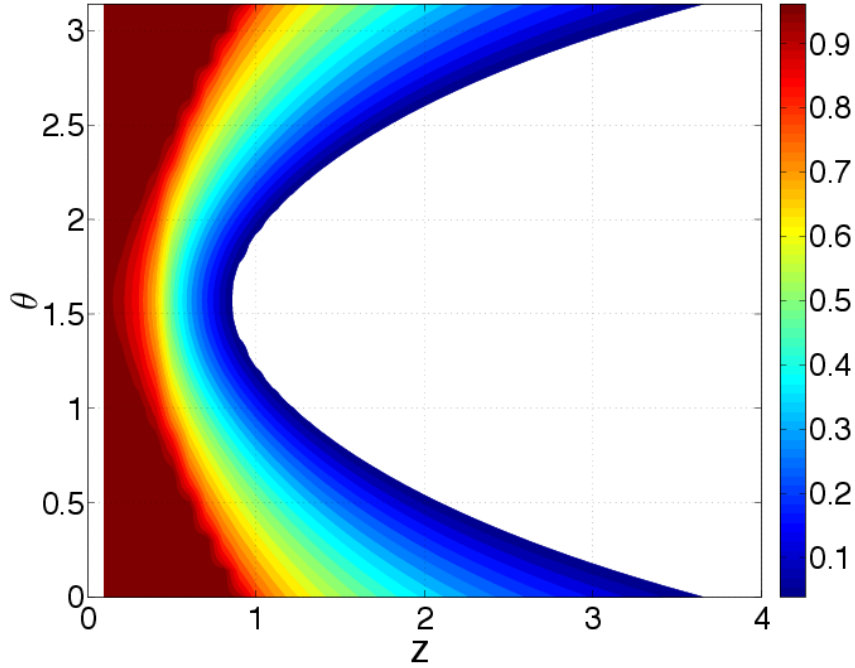


FIGURE 6.3: Detection efficiency as a function of the polar angle θ (measured from the zenith direction) for redshifts between 0 – 10, for NS-NS sources with masses $1.4+1.4 M_{\odot}$. The efficiency as a function of the inclination angle ι has a similar behavior. At a redshift $z = 0$ the efficiency is 1 for all the values of θ and ι while at the horizon distance of $z \sim 3.8$ only face-on sources located at the zenith or at the nadir are detected. The white area indicates there is no detection.

The frequency resolution of our analysis was 0.25Hz. The final point estimate at 10Hz is given by [28]

$$\hat{\Omega}_{\text{gw}} = \frac{\sum_i Y_i \sigma_{Y,i}^{-2}}{T_{\text{seg}} \sum_i \sigma_{Y,i}^{-2}}, \quad (6.18)$$

where Y_i and $\sigma_{Y,i}^2$ are the cross-correlations and variances calculated for each segment using Eq. (6.9, 6.10) respectively. The standard error on this estimate is given by

$$\sigma_{\Omega_{\text{gw}}} = T_{\text{seg}}^{-1} \left[\sum_i \sigma_{Y,i}^{-2} \right]^{-1/2}. \quad (6.19)$$

The isotropic analysis gives a point estimate of 3.21×10^{-12} for E1-E2, 3.18×10^{-12} for E1-E3, 3.22×10^{-12} for E2-E3, so an average of $\sim 3.2 \times 10^{-12}$, with error $\sigma_{\Omega_{\text{gw}}} = 4.4 \times 10^{-12}$ for the three pairs. Applying the correction factor of 1.3 derived above for the ORF, we found a point estimate at 100Hz of 4.26×10^{-12} for the pair E1-E2, 4.20×10^{-12} for E1-E3 and 4.3×10^{-12} for E2-E3. The average is $\hat{\Omega}_{\text{gw}} \sim 4.25 \times 10^{-12}$, which corresponds to the analytical expectation of $\sim 4.3 \times 10^{-12}$ with a precision of about 1%.

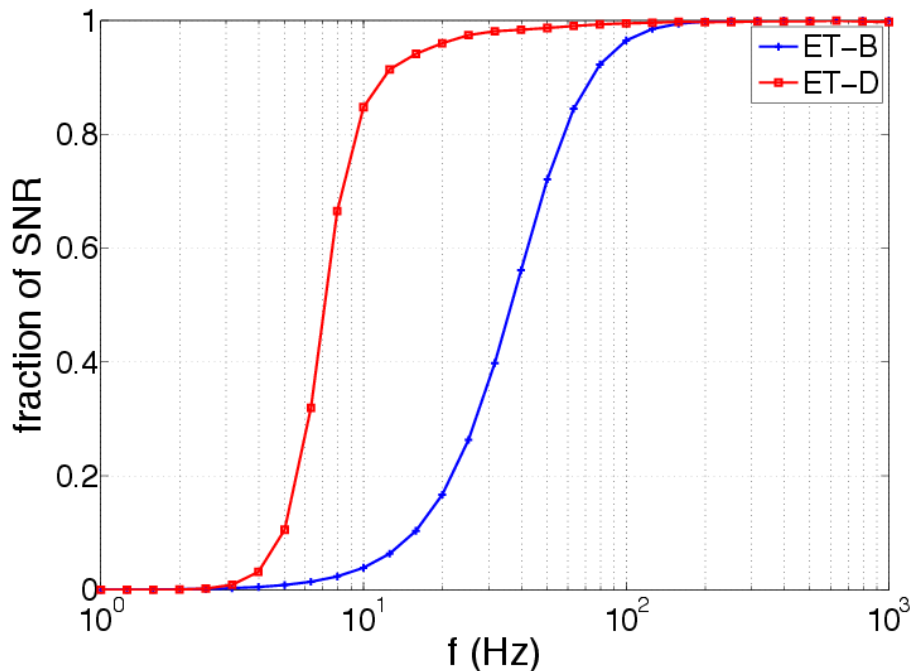


FIGURE 6.4: Contribution to the SNR of frequencies $< f$, for ET-D (ET MDC2) and ET-B (ET MDC1) [101]

6.5 Conclusion

In this paper we reported on the analysis of the second Einstein Telescope mock data and science challenge, searching for the residual GW background resulting from the superposition of all the CBC sources that are too faint to be detected individually. We used the standard cross correlation statistic which is known to be optimal in the case of a Gaussian, isotropic stochastic background. Confirming the results of the ET MDSC1 and the recent work of [62], we obtained that the non continuity or non gaussianity of the background [18, 48, 97, 101] does not significantly affect the analysis (what’s important is the total number of sources and not whether they overlap or not). But because of the GW selection effect that favored the detection of the best oriented and located sources, especially at larger redshift, the assumption of an isotropic stochastic background is not verified and the estimate given by the standard cross correlation statistic presents a systematic bias in the case of the residual background. Deriving a correction for the overlap reduction function we obtained a point estimate that agrees with the expected value with a precision $< 1\%$. The detection of the residual background would have very important consequences in cosmology and astrophysics as it would probe the high redshift population, complementing individual detections at smaller redshift. The residual background from CBC may dominate in the frequency band of ET. In future ET MDSC, we will investigate how one can use the non Gaussian signature to separate this background or foreground and recover the cosmological background.

Chapter 7

Revisiting coincidence rate between Gravitational Wave detection and short Gamma-Ray Burst for the Advanced and third generation

Astrophys J. 799. 69. (2015) [105]

T. Regimbau, K. Siellez, D. Meacher, B. Gendre, M. Boër

7.1 Sec:C9Introduction

The coalescence of compact binary systems, either neutron star - neutron star (BNS) or neutron star - black hole (NS-BH) are among the most promising sources for one of the first direct detections of gravitational waves (GWs) with the new generation of interferometers: the two Advanced-LIGO (aLIGO) [15] in Hanford and Livingston and Advanced-Virgo (AdV) [16] in Cascina. These facilities will be able to detect the late stage of the coalescence, the merger and the ring down of the binary systems located within few hundreds Mpc. The gravitational-wave signal during the adiabatic inspiral phase up to the last stable orbit and the final damped ring down of the final black hole are accurately described by post-Newtonian expansion and BH perturbation theory, while the progress of numerical relativity over the last decade has provided a deep understanding of the merger [115], giving a good level of confidence for a detection by the network of aLIGO and AdV (in the following we name the combined network consisting of the three interferometers aLIGO and AdV as ALV). With the planned third generation GW detector, Einstein Telescope (ET) [17], envisioned to consist of three independent V-shaped

Michelson interferometers with 60° opening angles, arm lengths of 10 km, arranged in a triangular configuration, and placed underground to reduce the influence of seismic noise, the maximal detection distance is expected to increase significantly over that of ALV, reaching cosmological distances ($z \simeq 4$ for BNS).

The coalescence of BNS systems is also believed to be at the origin of the short-hard gamma-ray bursts (sGRBs) [156]. In this scenario, the merger of the system produces a transient accretion disk, the gamma-ray emission being produced by the synchrotron and/or inverse Compton scattering from shocks in an ultra relativistic jet (see [157] for a review). Short GRBs might also produce a so-called kilonova through r-processes [158–161]. The standard hypothesis is that the BNS coalescence results in a black hole, though it is possible that a magnetar, or a transient magnetar, is produced as the result of the merger [162–165].

In this context the coincident detection of both GWs and electromagnetic radiation (EM) would be of paramount importance:

- The coincident detection of a GW and EM event would greatly improve the detection confidence with ALV during the early operations of the facilities.
- By using an EM detection of a sGRB as a trigger, one can perform a targeted GW search. This would allow for the detection of fainter signals, resulting in a larger horizon distance.
- On the other hand, GW alerts sent early to GRB satellites and EM telescopes could increase the chance of an EM detection, if the error on sky localization is smaller than the area covered by the satellite [127].
- Coincident detections could help solve the enigma of GRB progenitors (for instance BNS or NS-BH) but also of the central engine (the GW signature depends on the fate of the system, with the formation of either a black hole or magnetar) and give increased insight in the physics and dynamics of the system
- GRBs with measured redshift, observed also in GWs, could be used as standard sirens to constrain the Hubble constant and the dark energy equation of state [149, 166–169] or to recover the intrinsic mass distribution by breaking the observed mass-redshift degeneracy.

While long GRBs (lGRBs), assumed to originate from massive core collapse supernova have been detected out to a redshift $z = 8.3$ [165, 170], the maximal observed distance for sGRBs is considerably closer. From a comprehensive search for sGRBs in the rest-frame, [171] found a maximum distance of $z = 2.74$. However, *Swift* is not optimal for the detection of sGRBs whose spectrum is on average harder than that of lGRBs. BATSE and Fermi/GBM may have been able to detect sGRBs out to larger distance, but the larger sky localization errors associated with these experiments prevented any firm association with a given counterpart and thus redshift measurement. Hopefully the situation is improving thanks to the intermediate Palomar Transient Factory (iPTF) [172] and other proposed wide-field experiments such as the French ORMES project.

The EM emission of sGRBs (as well as that of lGRBs) is emitted in a narrow beam, though several estimates of the aperture of the jet have been reported [173]. This drastically reduces the chances to have a detection.

In order to estimate the coincident rate, one has to account for all the selection effects present in both GW and GRB observations. This is not trivial as there may be overlaps between them. For instance sGRB jets should be directed toward the observer to have a chance to be detected with GRB satellites, but source orientation also affect the strength of the GW signal. In this work, we use Monte Carlo simulations that take into account the selection effects of both GW and sGRB observations, to provide realistic estimates on the rate of coincident GW/sGRB detections with both ALV and ET.

The paper is organized as follows: in Section 7.2 we present our simulations, in Section 7.3 we derive the coincident efficiency, in Section 7.4 we estimate the coincident rate, in Section 7.5 we propose a simple method to measure the average value of the sGRB beaming angle, and finally, in Section 7.6 we summarize our main conclusions.

7.2 Monte-Carlo simulations

In order to investigate the expected rates of coincident detections of both GWs and sGRBs we perform Monte Carlo simulations using distributions in the expected parameter values. Fig. 7.1 shows a detailed flow chart of all the source parameters that are used in this work and how they relate to each other. We focus here on the population of primordial binaries (pairs of massive stars that survived two core-collapses to form compact systems) and neglect the population of dynamical binaries that may have been formed by captures in dense stellar environment and are not expected to contribute significantly to the total rate [79, 174, 175]¹.

7.2.1 Simulation of a population of BNS or NS-BH

Short GRBs are thought to be associated in majority with the coalescence of two neutron stars but it has been suggested that the merger of a neutron star and a black hole could also produce a beam of gamma-ray emission. Since this scenario cannot be excluded, we consider in this paper separately the two possible sources as the progenitors of sGRBs, binary neutron stars and neutron star-black holes. For each population, we first begin by drawing the source parameters, following a procedure similar to that described in [18, 103].

- The redshift is drawn from a probability distribution $p(z)$ (see in Fig. 7.2) constructed by normalizing (in the interval 0 – 10) the coalescence rate $\frac{dR}{dz}(z)$, as detailed in Section 7.4.
- Each event is given a sky position in equatorial coordinates (declination and right ascension) that is drawn from a isotropic distribution. The polarization angle, ψ , is selected from a

¹However, since they have longer evolution time and thus are more numerous at small redshift than primordial binaries, this population may represent the majority of currently observed sGRBs [176].

uniform distribution from $[0, 2\pi]$. The cosine of the inclination angle, $\cos \iota$, is also drawn from a uniform distribution in the range of $[-1, 1]$.

- The time interval between two successive events is given by the probability distribution $P(\tau) = \exp(-\tau/\lambda)$, assuming coalescences in the observer frame is a Poisson process. The average waiting time λ is computed from the inverse of the merger rate integrated over all redshifts. Equivalently, we can consider that the coalescence time in the observer frame t_c is a uniform distribution in the interval $[0, 2\pi]$ so as to represent one revolution of the Earth about its axis.
- For the initial set of simulations we consider a delta function for the distribution of the masses with $m_{NS} = 1.4M_\odot$ and $m_{BH} = 10M_\odot$. We will later consider the case of more realistic mass distributions.
- In order to model the properties of sGRBs, we also set the beaming angle (taken here as the half opening angle of the jet). We first investigate fixed angles covering a large range of values in the interval $[5^\circ - 30^\circ]$. As for the masses, we will consider use of a distribution of angles at a later stage.
- The intrinsic peak luminosity L_p (in erg s^{-1}) is drawn from the standard broken power law distribution first proposed by [177]

$$\Phi(L_p) \propto \begin{cases} (L_p/L_*)^\alpha & \text{if } L_*/\Delta_1 < L_p < L_*, \\ (L_p/L_*)^\beta & \text{if } L_* < L_p < \Delta_2 L_*, \end{cases} \quad (7.1)$$

with $\alpha = -0.6$, $\beta = -2$. We adopt the value of $L_* = 10^{51} \text{ erg s}^{-1}$, corresponding to model ii of [178–180] for primordial binaries, to which we have applied a factor of $\sim 1/2$ correction to convert L_* in the band $50 - 300 \text{ keV}$ to the band $15 - 150 \text{ keV}$ used in this paper (see Section 7.2.3). This is in agreement with the recent work of [176]². We also consider a conservative value of $L_* = 5 \times 10^{50} \text{ erg s}^{-1}$ (the lower bound of model ii of [178]), which accounts for a possible extra bias arising if, among the observed sample of sGRBs, those with redshift measurement are the most luminous. We choose $\Delta_1 = 100$ and $\Delta_2 = 10$, in order to cover more than 99% of the luminosities. Notice that taking $\Delta_1 = 30$ as suggested by [178] has a very small effect and does not affect the final results. We neglect in this work any possible evolution of the luminosity with redshift [181, 182].

- The log of the intrinsic duration of the burst, $\log T_i$, is drawn from a Gaussian distribution of mean $\mu_{\log T_i} = -0.458$ and standard deviation $\sigma_{\log T_i} = 0.502$, derived by fitting the sample of [183]. We neglect here any possible correlation between the peak luminosity and the duration.

7.2.2 GW selection effects

For each coalescence we must first determine if its resultant GW emission is detectable. For this purpose we calculate the event's coherent signal-to-noise ratio (SNR), for the detector network,

²actually there is a factor ~ 20 difference in the results of [176] since they used a larger energy band ($1 - 10000 \text{ keV}$)

in the ideal case of Gaussian noise (see [184] for a more sophisticated scenario including the possibility of false alarms).

The SNR detected by matched filtering with an optimum filter, in a detector labelled A , is

$$\rho_A^2 = 4 \int_0^\infty \frac{|\tilde{h}_+ F_{+,A} + \tilde{h}_\times F_{\times,A}|^2}{S_{n,A}(f)} df, \quad (7.2)$$

where f is the frequency of the gravitational wave in the observer frame, \tilde{h}_+ and \tilde{h}_\times the Fourier transforms of the GW strain amplitudes of polarisations $+$ and \times , $F_{+,A}$ and $F_{\times,A}$ the antenna response functions to the GW polarisations, and $S_{n,A}(f)$ the one-sided noise power spectral density (PSD) of detector A (see Fig. 7.3).

For low mass systems such as BNS or NS-BH, the SNR is dominated by the inspiral part of the signal and can reduce to

$$\rho_A^2 = \frac{5}{6} \frac{(G\mathcal{M}(1+z))^{5/3} \mathcal{F}_A^2}{c^3 \pi^{4/3} d_L^2(z)} \int_{f_{\min}}^{f_{\text{isco}}(z)} \frac{f^{-7/3}}{S_{n,A}(f)} df. \quad (7.3)$$

Here \mathcal{M} is the intrinsic chirpmass, a combination of the two component masses, $d_L(z)$ is the luminosity distance, G is the gravitational constant, c is the speed of light, f_{\min} is the low frequency limit of the detector and $f_{\text{LSO}}(z) = f_{\text{LSO}}/(1+z)$ is the observed (redshifted) gravitational-wave frequency of the last stable orbit. The factor

$$\mathcal{F}_A^2 = \frac{(1 + \cos^2 \iota)^2}{4} F_{+,A}^2 + \cos^2 \iota F_{\times,A}^2, \quad (7.4)$$

characterises the detector response. Assuming uncorrelated noise, the combined SNR for the network of detector is simply the quadrature sum $\rho^2 = \sum \rho_A^2$ of individual SNRs. If ρ is larger than a set SNR threshold level ($\rho \geq \rho_T$) then we say that the event is detectable.

7.2.3 EM selection effects

7.2.3.1 The beaming angle

The first selection effect affecting the detection of sGRBs in EM is the strong focussing of the ultra-relativistic jetted emission, i.e. the beaming angle θ_B . Only the fraction $\Theta_B = (1 - \cos \theta_B)$ of sources with inclination angle

$$|\cos \iota| \leq \cos \theta_B \quad (0 \leq \iota \leq \theta_B \text{ or } \pi \leq \iota \leq \pi + \theta_B), \quad (7.5)$$

can be observed on Earth.

Because of the small number of detections of afterglow associated with sGRBs, this angle is constrained to $5^\circ - 10^\circ$ for only a handful of cases (see e.g. [185–187]). The non detection of a

jet break also provides lower limits on the jet opening angle between 5° and 25° [157, 188–190]. Based on a sample of 79 IGRBs and 13 sGRBs [186] propose a median of about 10° . Because of this uncertainty we use a wide range of values for the jet opening angle between 5° - 30° .

7.2.3.2 Instrumental effects

The other obvious selection effects are related to the instrument: the burst can be undetected due to its faintness, to the fact that it is not located in the Field Of View (FOV), or because it occurs while the instrument cannot record it. This last effect is dominated by passes through the Southern Atlantic Anomaly (SAA), which reduce the Duty Cycle (DC) to $\sim 80\%$ of the total time. In the following, we take the effects of the FOV and the DC as independent factors reducing the probability of detection, independently of the source distance and spectrum. Table 7.1 gives a summary of the characteristics of the detectors we have considered in this work.

The trigger conditions can be complex, either for Fermi or *Swift*. For Fermi, GBM triggers when two or more detectors exceed background by n sigma over t timescale in e energy band. To do so, 62 algorithms operate simultaneously with different value for the threshold above background, various timescales and energy bands. Moreover, the energy and sensitivity threshold have been modified 8 times over 4 years as reported in the 2nd Fermi-GBM GRB catalog [191]. This resulted in a 20% difference in sGRB triggers over the period. For the *Swift* satellite, based on the photon count rates, the complex trigger algorithm adopted uses hundreds of criteria to maximize the GRB observations and cover the largest range of possible burst duration. Each criterion uses different time ranges for the foreground periods and backgrounds, to find the accurate SNR. If this SNR passes the threshold, then the event will have to pass a slew of procedures to confirm its nature. Because of the relative stability of the *Swift* trigger conditions, we decided to use it as a reference for the sensitivity. A simple scaling relation can be used to relate Swift and Fermi rates.

In this work, we restrict the trigger selections to the condition

$$L_p \geq L_{\text{lim}}(z) \quad \text{with} \quad L_{\text{lim}}(z) = F_{\text{lim}} 4\pi d_L(z)^2 k(z), \quad (7.6)$$

where L_p is the peak luminosity of a source at redshift z , F_{lim} is the limiting flux for a sGRB detection, and $k(z)$ is the k-correction due to the finite observation band at a given redshift. The limiting flux depends on the spectral properties of each trigger and also on whether it is seen on-axis or off-axis. For a generic sGRB defined by its peak energy $E_p = 440$ keV and low and high energy spectrum power indices $\alpha = -0.5$, and $\beta = -3.2$, the Band law [192] gives $F_{\text{lim}} \sim 0.4$ ph s⁻¹ cm⁻² for on-axis triggers in the 1 – 1000 keV observation band. A moderate variation of E_p (up to a factor 2 – 3) does not change significantly this result. For the *Swift* detection band 15 – 150 keV, it gives $F_{\text{lim}} \sim 0.56$ ph s⁻¹ cm⁻², which translates to $F_{\text{lim}} \sim 1.5$ ph s⁻¹ cm⁻² for off-axis sources. In addition to these optimal and averaged values, we also consider a pessimistic value of 2.5 ph s⁻¹ cm⁻², corresponding to sGRBs with redshift measurement.

Fig. 7.4 shows $L_{\text{lim}}(z)$ for these three limits, along with a sample of 17 observed sGRBs with redshift measurement [183], and 1000 simulated data with the conservative peak luminosity

distribution ($L_* = 5 \times 10^{50}$), which best fit the observed sample (using $L_* = 10^{51}$ produces too many detected sGRBs at large redshift).

7.3 Detection efficiency

In the following sections, we present the various selection effects described above in terms of efficiency, i.e. the fraction of sources, relative to the total, which can be detected at a given redshift.

7.3.1 GW efficiency

Several factors affect the maximum distance to which a GW detector will be able to detect a source (the horizon).

- The relative position of the source with respect to the detector plane at the time of coalescence: a detector is most sensitive to a GW signal that propagates orthogonally to the plane of the detector, meaning that the signal will be affected by both the position in the sky and the time of arrival.
- The second factor is the inclination angle, i.e. the angle between the normal of the source orbital plane and the observer's line of sight.

Fig. 7.5 displays the efficiency of ALV and ET for the two cases BNS and NS-BH. The SNR threshold is set to $\rho_T = 12$ for ALV [193], corresponding roughly to an SNR of 8 on at least two detectors. The observation of an EM counterpart, by increasing detection confidence, may allow to reduce the SNR threshold, thus we also use a less conservative value of $\rho_T = 8$, corresponding to an SNR of about 6 on two detectors (Sutton P., private communication). For the planned ET, we use $\rho_T = 8$ as suggested by mock data challenges [18]. At a redshift $z \sim 0$, all the sources are detected, but as the distance increases, only the best located and oriented sources reach the required threshold. The horizon of the detector corresponds to the maximum distance of detection for the optimally oriented (face-on) and positioned sources, and increases as the SNR threshold decreases. The ALV horizon is about 460 Mpc for BNS and 1 Gpc for NS-BH, assuming $\rho_T = 12$, or 720 Mpc for BNS and 1.6 Gpc for NS-BH, assuming $\rho_T = 8$. The ET horizon is $z = 4$ for BNS and $z = 13.5$ for NS-BH³.

7.3.2 Coincidence efficiency: the case of a perfect GRB detector

In order to model the EM selection effects, we first consider the case of a perfect GRB detector with FOV of 4π sr, duty cycle of 100%, and infinite sensitivity, so that the only selection effect

³our horizon distance is a bit higher than the one obtained in [79], as we have taken into account the redshift (see Eq. 7.3). For a single aLIGO detector, we would obtain an horizon of 485 Mpc instead of 445 Mpc for BNS, and 1090 Mpc instead of 927 Mpc for NS-BH.

is the beaming fraction. Compared to the previous case, we also require that the inclination ι (or $\pi - \iota$) is equal or smaller than the beaming angle, i.e. one of the two opposite jets is directed towards the Earth. The resulting efficiency presented in Fig. 7.6, $\varepsilon_{cdp}(z)$, is equal to the beaming factor at $z = 0$ and shows a *plateau* until a redshift z_* . Short GRBs closer than z_* can all be detected in GWs, then the efficiency decreases steadily until the GW detector horizon. The end of the *plateau* correspond to the redshift that gives a SNR $\rho = \rho_T$ when the inclination is equal to the beaming angle and the position in the sky and the polarization are such that \mathcal{F} is minimal.

Fig. 7.7 shows the efficiency ratio between $\varepsilon_{GW}(z)$ and $\varepsilon_{cdp}(z)$. The fraction of GW/EM coincident detections corresponds to the beaming angle efficiency at $z = 0$, then increases with the distance to reach 1 close to the GW horizon, where the only sources that can be detected are the best oriented and satisfy Eq. 7.5.

Our assumption of the same averaged value of the beaming angle for the whole population of sGRBs is certainly not realistic. We considered also a set of simple distributions (uniform and Gaussian for θ_B and $\cos \theta_B$ respectively) as well as the log-Gaussian distribution of [194], derived from observations, with average value $\mu_{\log \theta_B} = 2.0794$ and standard deviation $\sigma_{\log \theta_B} = 0.69$ (θ_B in degrees). We found that the efficiency is essentially sensitive to the average value of the beaming factor $\langle \Theta_B \rangle = (1 - \langle \cos \theta_B \rangle)$ and that the width and the shape of the distribution has very little impact. The efficiency is equal to $\langle \Theta_B \rangle$ during the *plateau* and the only difference is visible at the very end, where the distribution of the beaming angle results on a smoother transition between the *plateau* and the sharp decrease of the efficiency curve.

On the other hand, NS are expected to have a very narrow mass distribution centered around $1.4 M_\odot$ but the BH mass distribution is more uncertain. Changing the mass of the system affects the redshift z_* at which the *plateau* ends as well as the horizon distance. For a delta function, the SNR is shifted toward lower values when the mass decreases, as well as z_* and the horizon. For a broader distribution (for exemple a Gaussian or a uniform distribution), there is a smooth transition between the *plateau* and the sharp decrease of the efficiency curve, starting at the critical redshift $z_*(\mathcal{M}_{\min})$ corresponding to the minimal value of the chirp mass \mathcal{M}_{\min} and ending at $z_*(\mathcal{M}_{\max})$ corresponding to the maximal value of \mathcal{M}_{\max} . The horizon is the maximal distance observed for \mathcal{M}_{\max} .

7.3.3 Case of a realistic GRB detector

We now consider the case of a realistic GRB detector with finite sensitivity, and reduced FOV and duty cycle. The FOV, the duty cycle and the flux limit of the GRB satellites being independent of the GW detection, we write the final efficiency as the product

$$\varepsilon_{cd}(z) = \varepsilon_{FOV} \times \varepsilon_{DC} \times \varepsilon_{cdp}(z) \times \varepsilon_{sat}(z), \quad (7.7)$$

where ε_{FOV} is the FOV divided by 4π sr, ε_{DC} is the duty cycle, ε_{cdp} is the efficiency for a perfect detector found in Section 7.3.2, and $\varepsilon_{sat}(z)$ is the fraction of sGRBs whose flux is larger than the limiting flux F_{lim} (see Section 7.2.3).

The efficiency of *Swift* derived from our Monte Carlo procedure is presented in Fig. 7.8 for a flux threshold of $1.5 \text{ ph s}^{-1} \text{ cm}^{-2}$, a pessimistic value of $2.5 \text{ ph s}^{-1} \text{ cm}^{-2}$, corresponding to sGRBs with redshift measurement, and an optimal value of $0.56 \text{ ph s}^{-1} \text{ cm}^{-2}$, corresponding to on-axis sources. The shape is very similar to that presented in [182] and [195] for long GRBs, with a sharp exponential decrease.

Fig. 7.9 shows the coincident efficiency, taking into account the sensitivity of *Swift*, for $\theta_B = 10^\circ$ and the three flux threshold of 0.56, 1.5 and $2.5 \text{ ph s}^{-1} \text{ cm}^{-2}$.

For ALV, the coincident sensitivity is limited rather by the GW detector horizon than the GRB flux threshold. The effect of the *Swift* sensitivity is not significant for BNS, but is noticeable for NS-BH, especially with an SNR threshold of 8, mainly by reducing the size of the *plateau*.

For ET, the efficiency of a GRB satellite like *Swift* will drop much faster than the GW efficiency, causing the suppression of the *plateau* and shifting the horizon to smaller redshift. In order to have 100% of the sources above the threshold at $z \sim 1$ (corresponding to the end of the *plateau* for BNS), and then fully exploit the potentiality of ET, F_{lim} would have to be reduced to $\sim 0.0013 \text{ ph s}^{-1} \text{ cm}^{-2}$ over the next decade if $L_* = 10^{51} \text{ erg s}^{-1}$ (a factor of 2 smaller if $L_* = 5 \times 10^{50} \text{ erg s}^{-1}$). A value of $0.2 \text{ ph s}^{-1} \text{ cm}^{-2}$ would give 80% of the sources above the threshold at $z = 1$ and $1.1 \text{ ph s}^{-1} \text{ cm}^{-2}$ 50 %.

7.4 Rate

In this paper, we assume the coalescence occurs after two massive stars in a binary system have burned all their nuclear fuel, have evolved into red giants, and the cores have collapsed, possibly after supernova explosions, forming a bound system of two compact objects (neutron stars or black holes) inspiralling each other due to the emission of GWs. Another scenario suggests that NS or BH binaries could form through dynamical captures in dense stellar environment. However, most simulations indicate that the chance for this to occur is small, due to the presence of massive black holes at the center that substitute into binaries during dynamical interactions, so that this population may not represent a significant fraction of the total coalescence rate [79]⁴.

The coalescence rate per interval of redshift

$$\frac{dR}{dz}(z) = \dot{\rho}(z) \frac{dV}{dz}, \quad (7.8)$$

⁴Notice that the dynamical origin is favored in the recent study of [176] as sGRB progenitors, which may suggest that they are more numerous than what is predicted by simulations or that dynamical binaries are not affected by the same selection effects as primordial binaries [196]

is obtained by multiplying the element of comoving volume $\frac{dV}{dz}$ and the coalescence rate per unit of volume

$$\dot{\rho}(z) \propto \int \frac{\dot{\rho}_*(z_f)}{1+z_f} P(t_d) dt_d \text{ with } \dot{\rho}(0) = \dot{\rho}_0, \quad (7.9)$$

In this equation, $\dot{\rho}_*$ is the star formation rate (SFR), $\dot{\rho}_0$ the local coalescence rate in $\text{Mpc}^{-3} \text{Myr}^{-1}$, z_f the redshift at the time of formation of the massive binary system and $P(t_d)$ the probability distribution of the delay between the formation and the coalescence. The number of massive systems that remain bounded after two supernovas (or prompt core-collapses) is uncertain, as well as the time to coalescence (the delay) which depends on complicated evolution scenario involving common envelope and mass transfer. We assume a distribution of the form $P(t_d) \propto 1/t_d$ with a minimal delay of 20 Myr for the population of BNS and 100 Myr for BH-NS, as suggested by the population synthesis software StarTrack [112], and we leave $\dot{\rho}_0$ which is given between $0.001 - 10 \text{ Mpc}^{-3} \text{ Myr}^{-1}$ by [79] as a free parameter. The co-moving volume element is given by

$$\frac{dV}{dz}(z) = 4\pi \frac{c}{H_0} \frac{r(z)^2}{E(\Omega, z)}, \quad (7.10)$$

where

$$r(z) = \frac{c}{H_0} \int_0^z \frac{dz'}{E(\Omega, z')}, \quad (7.11)$$

and

$$E(\Omega, z) = \sqrt{\Omega_\Lambda + \Omega_m(1+z)^3}. \quad (7.12)$$

In this paper, we use a standard flat cold dark matter (Λ CDM) model for the Universe, with $\Omega_m = 0.3$ and $H_0 = 70 \text{ km s}^{-1} \text{ Mpc}^{-1}$.

In order to account for the uncertainty in the star formation history, we consider seven different SFRs described in detail in [90, 100] and plotted in Figure 7.10. As a reference, we use the SFR of [110], which is derived from measurements of the galaxy luminosity function in the ultra-violet (UV) and far infra-red (FIR) wavelengths, and is normalized by the Super Kamiokande limit on the electron antineutrino flux from past core-collapse supernovas. This model is expected to be quite accurate up to $z \sim 2$, with very tight constraints at redshifts $z < 1$ (to within 30 – 50%). [197] use a different set of measurements and a different dust extinction correction. The SFR found in [197] is the same as that of [110] up to $z \sim 1$, but decreases slightly at higher redshifts. We also consider the model described by [198], which is derived from measurements of the stellar mass density. The SFR is equivalent to that in [110, 197] for $z \lesssim 0.7$, but again is lower at higher redshifts. Note that at present there is a discrepancy between the “instantaneous” SFR, measured from the emission of young stars in star forming regions, and the SFR as determined from extragalactic background light. This could have an important impact on the contribution

of at $z > 2$. Finally, we consider the analytical SFR of [199] derived from cosmological Smoothed Particle Hydrodynamics numerical simulations, the model of [200] derived from the fossil record of star formation in nearby galaxies which probably underestimate the SFR at small redshifts but may be more accurate that and is constant at high redshifts due to the contribution of elliptical galaxies, and the SFR of [201], which combined observations and simulations at higher redshift. For completeness, we also considered a previous model derived from the UV continuum and $H\alpha$, up to $z \sim 4$, where the main uncertainty comes from dust extinction, which spreads the UV luminosity into the FIR [202].

7.4.1 Detection rates

The GW detection rate is obtained by integrating over redshift the product of the coalescence rate given in Eq. 7.9 and the GW efficiency

$$R_{\text{gw}} = \int_0^{z_{\text{max}}} \varepsilon_{\text{gw}}(z) \frac{dR}{dz}(z) dz, \quad (7.13)$$

where z_{max} corresponds to the beginning of stellar activity. From our models, $z_{\text{max}} \sim 10 - 20$.

This equation is different than the approximated expression $R_{\text{gw}} = \frac{4}{3}\pi(d_{\text{max}}/2.26)^3$ [203], where d_{max} is the horizon distance and the factor 2.26 a correction needed to average over sky location and orientation. These two equations are similar when facing with the probe of a small volume, like in the current era of advanced detectors, but strongly diverge for a larger horizon, which is the key signature of ET. In such a case, including the efficiency, the star formation history and the cosmology becomes crucial.

In the same way, we calculate the GW/sGRB detection rate as

$$R_{\text{cd}} = \int_0^{z_{\text{max}}} \varepsilon_{\text{cd}}(z) \frac{dR}{dz}(z) dz. \quad (7.14)$$

Compared to the simple beaming factor correction $R_{\text{cd}} = \Theta_B R_{\text{gw}}$, this equation results in an improvement of the final coincident rate by a factor of ~ 3 in the case of a perfect sGRB detector, only limited by the beaming selection effect.

The GW coincident rates for ALV and the *Swift* detector are presented in Table 7.2, for different beaming angles. We used as a reference, the local rates of $\rho_c^2 = 0.06 \text{ Mpc}^{-3} \text{ Myr}^{-1}$ for BNS and $0.003 \text{ Mpc}^{-3} \text{ Myr}^{-1}$ for NS-BH, obtained recently by [204] for the StarTrack standard model. They correspond to GW detection rates of about 3 yr^{-1} for BNS and 2 yr^{-1} for NS-BH, assuming a threshold of 12 for the SNR. That turns out to represent a coincident detection rate for BNS and NS-BH mergers from a few every 1000 years to a few every 10 years depending on the beaming angle θ_B . These rates are 2% ($\rho_T = 12$) and 5% ($\rho_T = 8$) smaller than the rates one would obtain assuming infinite GRB satellite flux sensitivity for BNS, and 10% ($\rho_T = 12$) and 18% ($\rho_T = 8$) for BH-NS. Decreasing the SNR threshold from 12 to 8, increases the number of detections by a factor of 3. The coincident rates derived for *Swift* would improve by a factor

of ~ 10 for a detector with a large FOV like Fermi, but only by a factor of 1.4 and 2.4 for the planned FOV of SVOM and LOFT.

Our results derived from simulations of the cosmological population of BNS and NS-BH are in agreement with the rates derived from sGRBs observations by [171, 0.06 – 0.16 yr⁻¹], for our reference value of the local merger rate of $\dot{\rho}_c^o \sim 0.06 \text{ Mpc}^{-3} \text{ Myr}^{-1}$, or the lower bound of [188] ($\sim 0.1 - 10 \text{ yr}^{-1}$ after FOV and DC correction), based on bias correction of *Swift* data. They are a factor of 10 smaller than the rates found by [205, 0.2 – 1 yr⁻¹]. Comparing the different studies is difficult though, as different authors used different assumptions.

As one can see, the coincident rate is very sensitive to the beaming angle θ_B . Between a half jet opening angle of $\theta_B=5^\circ$ and $\theta_B=30^\circ$, the rate increases by a factor of about ~ 35 . Using the efficiency presented in Fig.7.9, we roughly estimated that for our reference value of the local merger rate, the beaming angle, should be between $3^\circ - 10^\circ$ in order to reproduce the actual observed rate of 8 sGRBs per year with *Swift*, which is consistent with current models of the sGRB jet. This would favor a coincident rate between ALV and *Swift* $< 0.1 \text{ yr}^{-1}$. Increasing the local merger rate would shift the allowed range for the beaming angle toward lower values so that the final coincident rate would be unchanged. However, these estimates of the beaming angle should be considered with precaution due to the uncertainties associated with the intrinsic luminosity distribution derived by population synthesis from the small sample of observed sGRBs.

For ET the GW coincident rates are presented in Table 7.3 for a detector with a FOV of $4\pi \text{ sr}$, a duty cycle of 80% and an infinite flux sensitivity. This is of course unrealistic but it gives an upper limit of the number of coincidences in 10 – 20 years. If the sensitivity of GRB satellites do not improve in the next decade compared to *Swift*, the best one can expect is the *Swift* rate of 8 detections a year. This is much better than the rates predicted for ALV, but orders of magnitude below the ET potential. As a matter of consequence, we note that the construction of ET should be accompanied by the launch of a new generation of space observatories focussed on transient events.

7.5 Constraints on the beaming angle

Coincident GW/GRB detections can help measuring, or at least putting strong constraints on the beaming angle of sGRBs [206, 207]. We propose here a very simple method to measure the average beaming factor and thus $\langle \cos \theta_B \rangle$. The number of ALV coincident triggers will be probably too small to do a parameter estimation, thus we consider only the case of ET. We note that it is likely that a further enhancement of ALV, or a new detector before ET provide an intermediate case. For simplicity, we neglect NS-BH sources.

In the redshift interval $z = 0 - 0.2$, the GW efficiency of ET is almost 1 (99.5% of the sources can be detected) and we assume the sensitivity of the satellite is good enough so that only a negligible fraction of all the sGRBs is below the flux threshold⁵. The efficiency of coincident

⁵with $F_{lim} = 0.1 - 0.2 \text{ ph s}^{-1} \text{ cm}^{-2}$, we have 99% of the sources above the threshold at a redshift of $z = 0.2$ for instance

detections is then equal to the average beaming factor (times some factor due to the duty cycle and the FOV) and we can construct the estimator of Θ_B

$$\hat{\Theta}_B = (\varepsilon_{FOV} \times \varepsilon_{DC})^{-1} \frac{N_{cd}^0}{N_{GW}^0}, \quad (7.15)$$

where N_{cd}^0 is the number of coincident detections and N_{gw}^0 the number of GW detections alone, for z in the bin $[0 - 0.2]$.

In order to test our method, we consider a population of BNS with local rate of $\dot{\rho}_c^0 = 0.1 \text{ Mpc}^{-3} \text{ Myr}^{-1}$. Using the SFR of [110], we obtain a total of $N_{GW}^0 \sim 3000$ GW over the operation lifetime of ET we assume to be 10 years. We build the histogram of $\hat{\Theta}_B$ from a sample of 10^5 simulations (Fig. 7.11) and find that $\hat{\Theta}_B$ is a non-biased estimator of Θ_B (the average value $\langle \hat{\Theta}_B \rangle$ converges to the true value) with an error that depends on the average number of coincident sources in one simulation, and thus on the SFR, the local rate, the beaming angle, the duty cycle and the FOV, and of course the time of observation. We confirm the result found in Section 7.3.2 that a distribution of the beaming angle does not affect the number of coincident detections, and thus the beaming factor estimator. However, when the distribution of θ_B is not known, we can only measure the average value of the cosine.

Table 7.4 gives the average value of $\hat{\Theta}_B$ and the standard deviation for the SFR of [110] ($\langle N_{gw}^0 \rangle \sim 3000$) for $\varepsilon_{FOV} = \varepsilon_{DC} = 1$ and fixed angles of 5° , 10° and 15° .

For different combinations of local rates, SFR, duty cycle and FOV or time of observation T , one should simply rescale the standard deviation as

$$\sigma' = \sqrt{\frac{3000}{\langle N_s \rangle'}} \sigma, \quad (7.16)$$

with

$$\langle N_s \rangle' = T \times \varepsilon_{DC} \times \varepsilon_{FOV} \times \dot{\rho}_0 \times \langle N_{gw}^0 \rangle, \quad (7.17)$$

where T is in year and $\dot{\rho}_0$ in $\text{Mpc}^{-3} \text{ Myr}^{-1}$. For example the standard deviation should be multiplied by 3 for $\varepsilon_{FOV}=0.15$ and $\varepsilon_{DC}=0.8$. We have also studied the different distributions of θ_B used in III.D and confirmed this result.

7.6 Conclusion

In this paper, we have presented Monte Carlo simulations of coincident detections between gravitational wave and electromagnetic detectors. We have assumed that sGRBs could be powered by BNS or NS-BH coalescences and we have modeled the different selection effects of both GW and EM detectors. We have calculated a coincident efficiency taking into account the fact that the source inclination affect both the GW and GRB efficiency. Besides the beaming angle and

the GRB satellite field of view, which are the most important effects, we have shown that the coincident sensitivity is limited by the GW detector horizon for the network of advanced detectors ALV, while for ET it is the GRB flux threshold that is the most important. For ALV the best GRB satellite will be the one with the largest field of view, independently of the flux sensitivity, but for ET, the most important gain will come from the improvement of the sensitivity. In order to roughly estimate the sensitivity required for such an "optimized" sGRB detector used for the follow-up of ET, we have estimated that reducing the average flux limit to $F_{\text{lim}} \sim 0.1 - 0.2$ ph s⁻¹cm⁻² over the next decade, would allow 80% of the sources at a redshift of $z \sim 1$ (corresponding to the end of the *plateau* of the coincident detection efficiency for BNS) to be above the threshold. The flux limit would have to be reduced to $F_{\text{lim}} \sim 0.02 - 0.05$ ph s⁻¹cm⁻² to obtain 80% at $z = 2$, where we have the peak of the distribution of the redshift, and where the difference between dark energy equation of states cosmological models is more visible.

Using a set of star formation rate models, we have calculated the coincident rate for different values of the beaming angle for ALV and ET. Our results predict a small number of coincident detections with ALV (less than one event per year for the *Swift* field of view of 1.4 sr and a duty cycle of 80 %), in agreement with recent studies (see for instance [171, 188, 205]). The observation of a sGRB counterpart, by increasing detection confidence, may allow for the reduction of the SNR threshold. We have shown that using a threshold of 8 rather than 12 increases the number of coincident detections by a factor of 3 for ALV. We have found a potential number of coincidences of $\sim 100 - 10000$ per year for ET assuming GRB satellites can reach the desired flux threshold and a maximum FOV of 4π , but this number will reduce to a few events per year if the FOV and the sensitivity do not improve compared to *Swift*.

Finally we have proposed an original method to estimate the mean jet opening angle of sGRBs. This method can be applied to ALV though with low sensitivity. The accuracy will improve as the sensitivity of the GW detectors enhances.

The coincident rates could slightly increase by considering the population of dynamical binaries that could have formed by captures in dense environment and that could be numerous at low redshift due to the long delay between formation and coalescence [176]. However we do not expect a big change and our findings emphasize the need of a dedicated, wide field of view, multi-wavelength follow-up of GW detections with a sensitivity increase by a factor 5 to 10 compared to current detectors.

TABLE 7.1: Summary of the properties of the different electromagnetic detectors: the duty cycle DC, the field of view FOV in steradians, and the energy band in keV.

Mission	DC (%)	FoV (sr)	Energy band (keV)
<i>Swift</i>	80	1.4	15–150
Fermi-GBM	80	9.5	8–30000
<i>SVOM</i>	80	2	4–5000
<i>LOFT</i>	80	π	2–80

 TABLE 7.2: BNS and NS-BH coincident detection rates (in units of yr^{-1}) for different values of the beaming angle, for ALV and the *Swift* GRB satellite with a FOV of 1.4 sr, a duty cycle of 80%, and a flux limit of $F_{\text{lim}} = 1.5 \text{ ph s}^{-1} \text{ cm}^{-2}$. The range of values reflects the uncertainty on the SFR. The first line correspond to a signal-to-noise ratio thresholds of 12 and the second line to 8. We used the local rates of $\dot{\rho}_c^0 = 0.06 \text{ Mpc}^{-3} \text{ Myr}^{-1}$ for BNS and $0.003 \text{ Mpc}^{-3} \text{ Myr}^{-1}$ for NS-BH, obtained recently by [204] for the StarTrack standard model. For other local rates, one should multiply the values of Table 7.2 by $\dot{\rho}_c^0/0.06$ for BNS or $\dot{\rho}_c^0/0.003$ for NS-BH. The values in the last column indicates the GW detection rate. The rates for the other satellites can be obtained by multiplying these results by $\text{FOV}/1.4 \text{ sr}$, with the FOV given in Table 7.1.

	5°	10°	15°	20°	30°	GW
BNS						
$\rho_T = 12$	0.004 – 0.005	0.01 – 0.02	0.03 – 0.04	0.06 – 0.07	0.11 – 0.13	2.5 – 3.0
$\rho_T = 8$	0.01 – 0.02	0.05 – 0.06	0.10 – 0.13	0.18 – 0.23	0.35 – 0.46	
NS-BH						
$\rho_T = 12$	0.001 – 0.002	0.006 – 0.008	0.01 – 0.02	0.02 – 0.03	0.04 – 0.06	1.5 – 2.0
$\rho_T = 8$	0.004 – 0.005	0.01 – 0.02	0.03 – 0.04	0.05 – 0.08	0.11 – 0.16	

 TABLE 7.3: Same as Table 7.2 for ET, assuming a GRB satellite with a FOV of 4π sr and infinite flux sensitivity, but accounting for the duty cycle of 80%.

	5°	10°	15°	20°	30°	GW
BNS	$(0.8 - 1.8) \times 10^2$	$(3 - 7) \times 10^2$	$(0.7 - 1.6) \times 10^3$	$(1.3 - 2.8) \times 10^3$	$(2.5 - 5.8) \times 10^3$	$(0.6 - 1.5) \times 10^4$
NS-BH	7 – 15	27 – 61	59 – 136	104 – 239	228 – 517	$(1.3 - 2.4) \times 10^3$

 TABLE 7.4: Mean and standard deviation of the beaming angle estimator $\hat{\Theta}_B$ for the SFR of Hopkins ($\langle N_{\text{gw}}^0 \rangle \sim 3000$), and assuming a GRB satellite with a FOV of 4π sr, duty cycle of 100% and infinite flux sensitivity.)

θ_B ($^\circ$)	$\langle \hat{\Theta}_B \rangle$	$\sigma_{\hat{\Theta}_B}$	error (%)
5	0.0039	0.0011	29.3
10	0.015	0.0022	14.5
20	0.060	0.00042	7.23

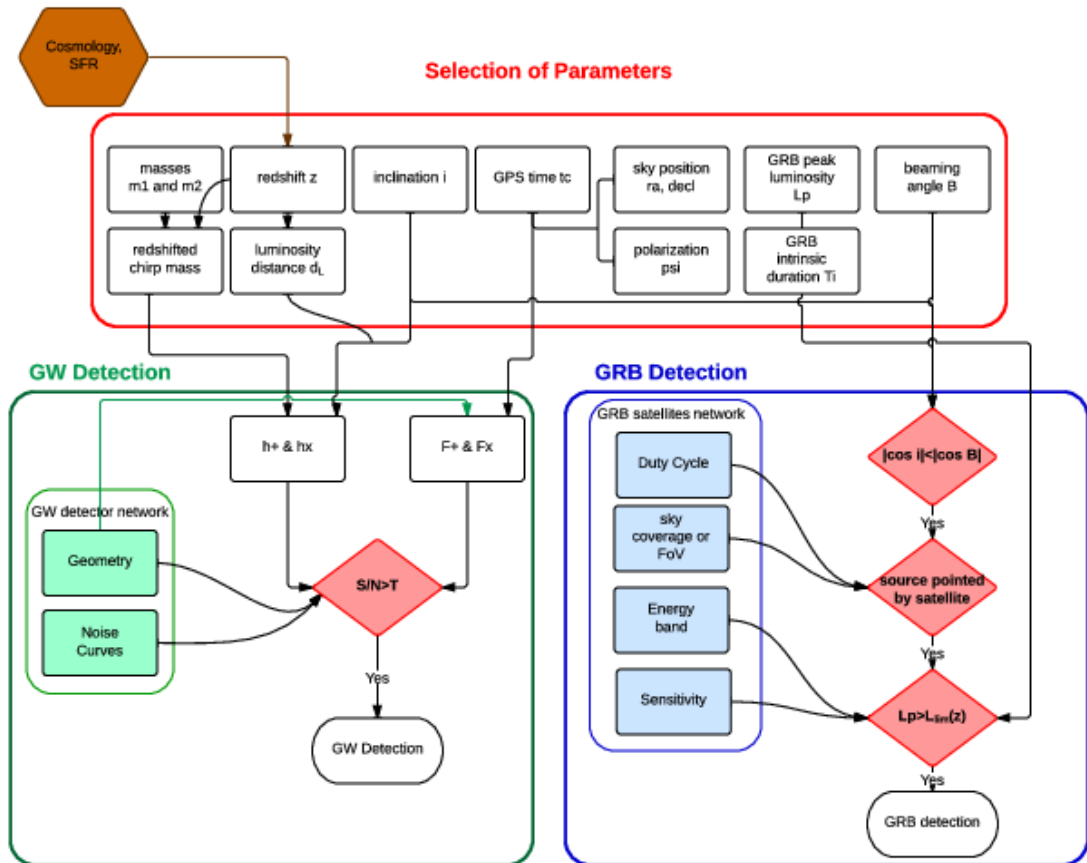


FIGURE 7.1: A flowchart showing all the different parameters used in these simulations. Here the red box indicates the source parameters shown in section 7.2.1. The green box shows the parameters that are used to determine if the event will be observed as a GW detection, see section 7.2.2, and the blue box displays the parameters that are used to determine if the event will be observed as a sGRB, see section 7.2.3. The arrows indicate how the different parameters are related to each other. Colors available on the online version only.

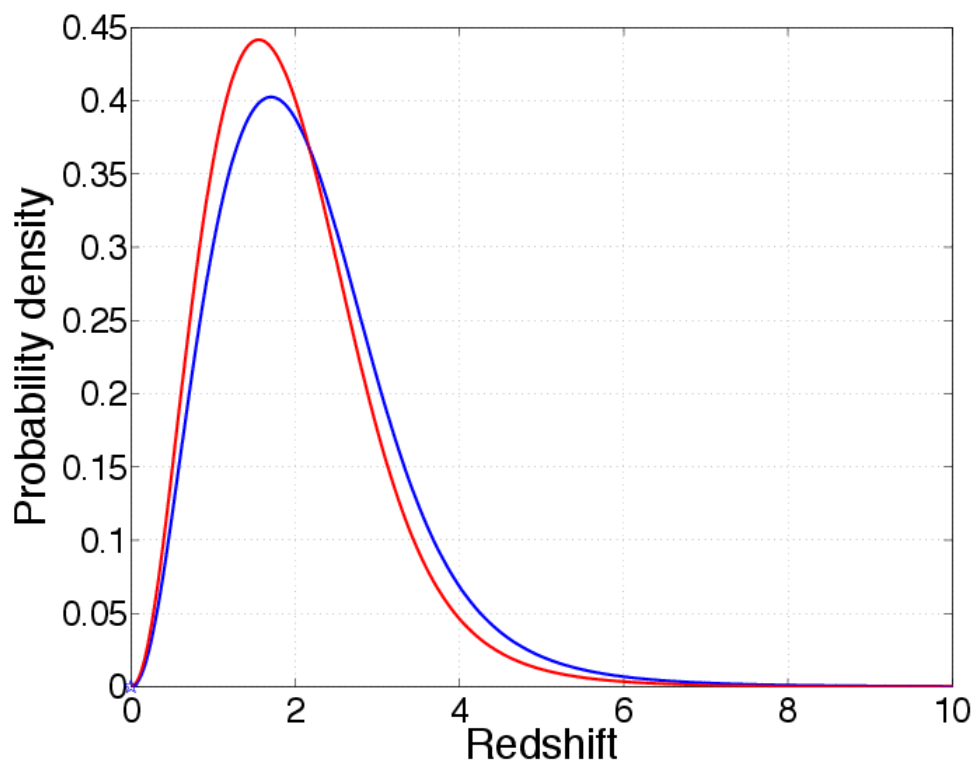


FIGURE 7.2: Probability distribution of the redshift of BNS (blue, smaller peak) and NS-BH (red, higher peak), assuming the star formation rate of [110], a distribution of the delay of the form $P(t_d) \propto 1/t_d$ with minimal delay of 20 Myr for BNS and 100 Myr for NS-BH.

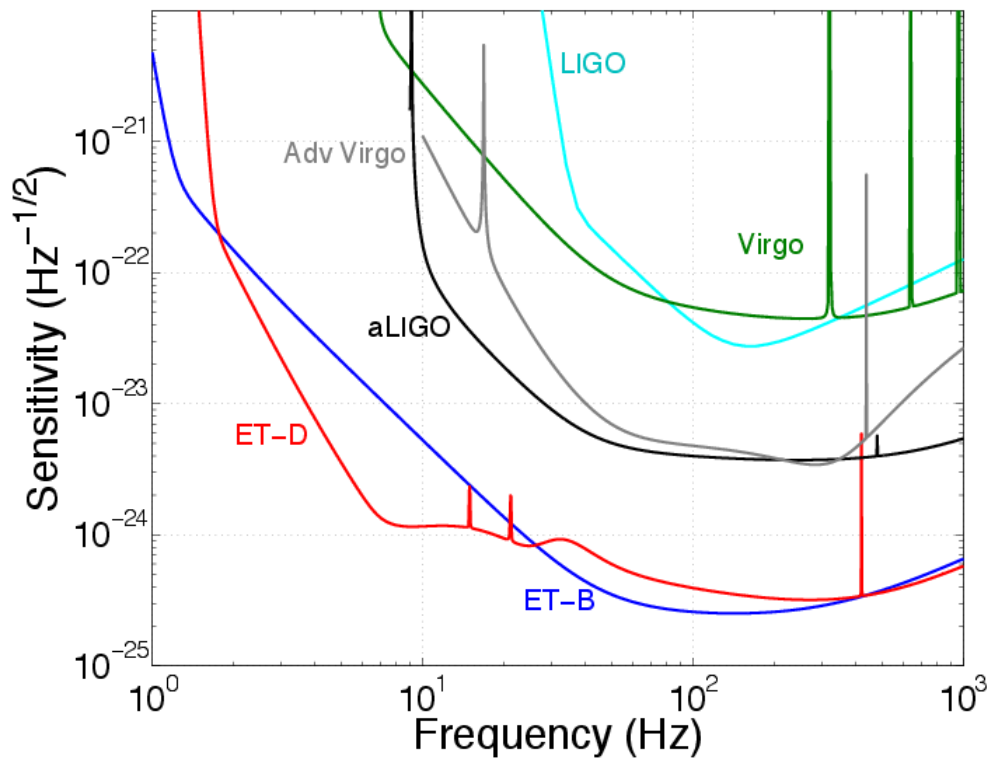


FIGURE 7.3: Projected sensitivity for second generation (advanced) detectors (here the aLIGO high-power zero detuning sensitivity [15] and Adv Virgo BNS optimized [16]) and for the initial configuration of ET, ET-B, considered in the Design Study, and the most evolved configuration ET-D [17]. The sensitivity of first generation detectors LIGO and Virgo is also shown for comparison.

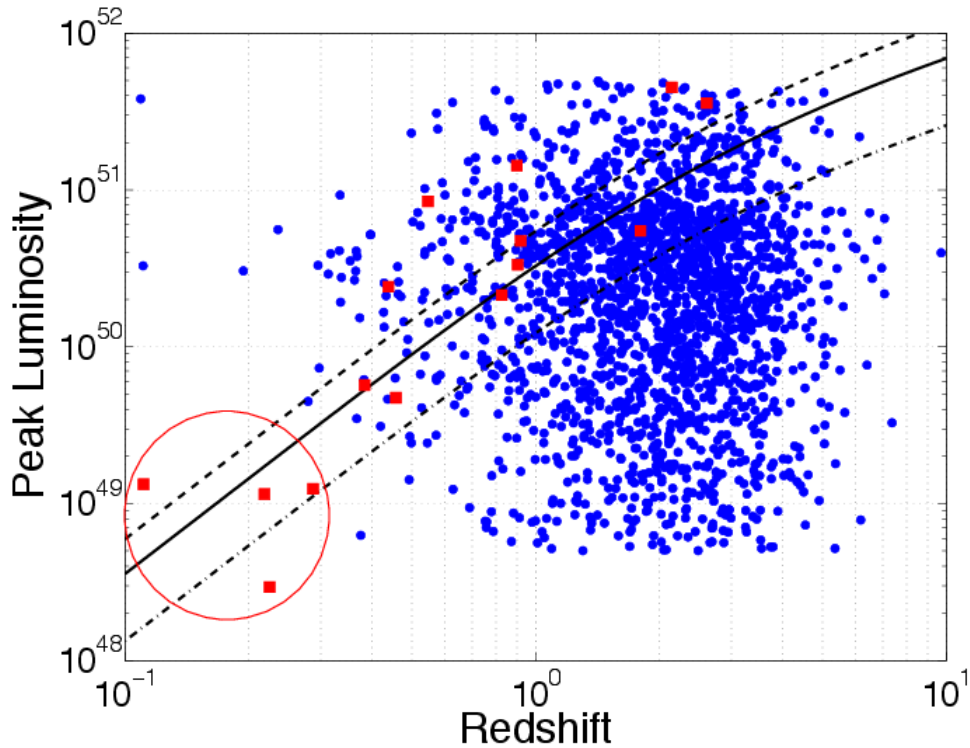


FIGURE 7.4: Sensitivity of the *Swift* satellite for a flux limit of $1.5 \text{ ph s}^{-1}\text{cm}^{-2}$ (continuous black line), $2.5 \text{ ph s}^{-1}\text{cm}^{-2}$ (dashed black line), corresponding to sGRBs with redshift measurement, and an optimal value of $0.56 \text{ ph s}^{-1}\text{cm}^{-2}$ (dash-dotted black line), corresponding to on-axis sources. The blue circles correspond to a sample of 10000 sources simulated from the Monte Carlo procedure described in 7.2. The red squares show a sample of 17 observed sGRBs [183]. The low redshift/low luminosity population, indicated by a red circle in the bottom left of the plot, is difficult to reproduce with the simulations and could be either a population of magnetars or dynamical BNS or NS-BH whose long evolution times, of the order of 3 Gyr [176], may explain why they are more numerous at low redshift. It would not explain why they would be sub-luminous though.

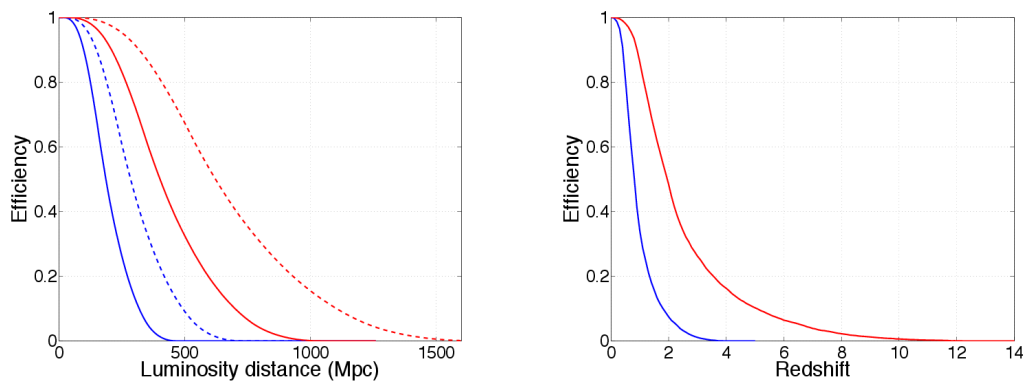


FIGURE 7.5: *Left*— GW detection efficiency as a function of luminosity distance of BNS (blue) and NS-BH (red) for the ALV network. The continuous and dashed lines correspond to signal-to-noise ratio threshold of 12 and 8 respectively. *Right*— GW detection efficiency as a function of redshift of BNS (blue) and NS-BH (red) for ET and a signal-to-noise ratio threshold of 8. We assumed masses of $1.4 M_{\odot}$ for neutron stars and $10 M_{\odot}$ for black holes.

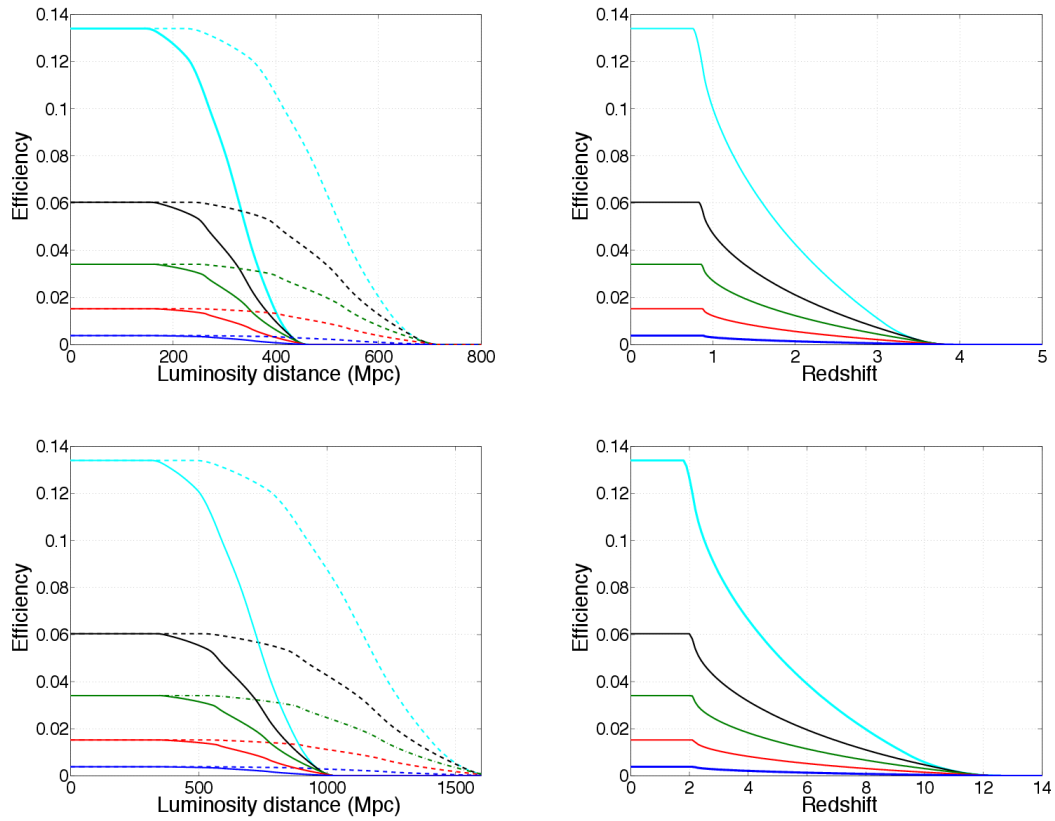


FIGURE 7.6: *Left*— GW/GRB coincident detection efficiency of BNS (top) and NS-BH (bottom), for ALV, assuming infinite sensitivity, an FOV of 4π and a duty cycle of 100% for the GRB satellite, and signal-to-noise ratio threshold of 12 (continuous lines) and 8 (dashed lines). The curves that extend to larger distances are for a threshold of 8. *Right*— GW/GRB coincident detection efficiency as a function of redshift of BNS (top) and NS-BH (bottom), for ET, infinite sensitivity, an FOV of 4π and a duty cycle of 100% for the GRB satellite, and signal-to-noise ratio threshold of 8. The different lines indicate different values of the beaming angle. From top to bottom, 30, 20, 15, 10, and 5 degrees.

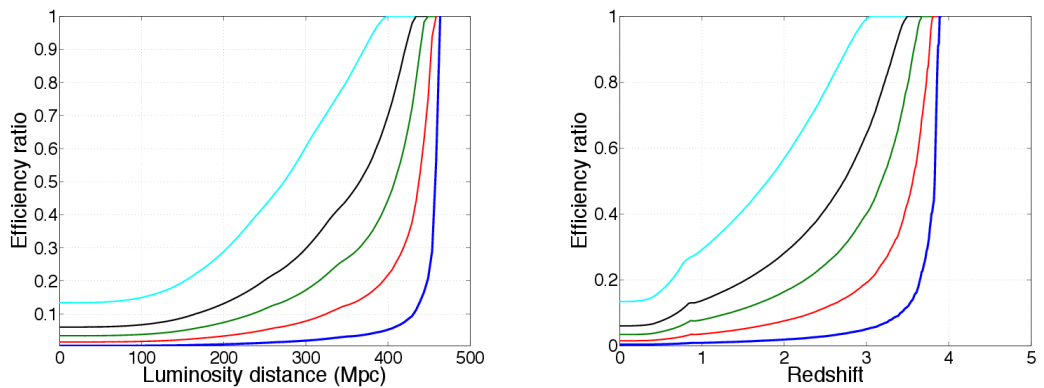


FIGURE 7.7: Ratio of total GW events to those that can be observed as sGRBs, assuming infinite sensitivity, an FOV of 4π and a duty cycle of 100% for the GRB. *Left*— ALV with signal-to-noise ratio threshold of 12. *Right*— ET with signal-to-noise ratio threshold of 8. The behavior is similar for NS-BH. The different lines indicate different values of the beaming angle. From top to bottom, 30, 20, 15, 10, and 5 degrees.

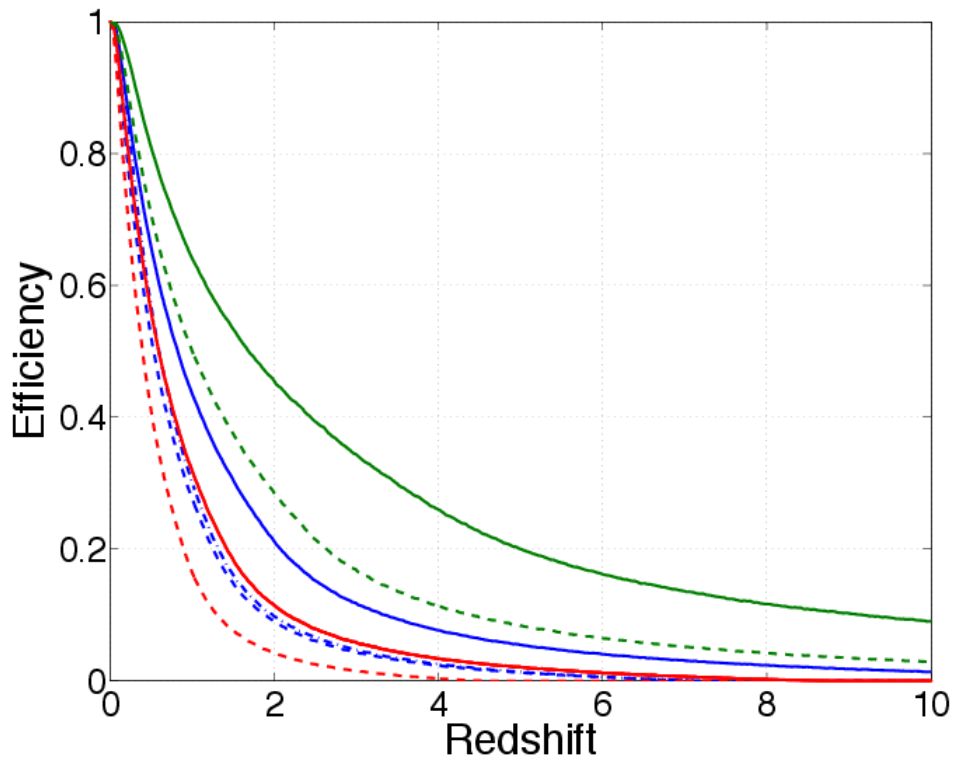


FIGURE 7.8: Detection efficiency of the *Swift* satellite for sGRBs assuming a flux limit of $1.5 \text{ ph s}^{-1} \text{ cm}^{-2}$ (blue lines), a pessimistic value of $2.5 \text{ ph s}^{-1} \text{ cm}^{-2}$ (red lines), corresponding to sGRBs with redshift measurement, and an optimal value of $0.56 \text{ ph s}^{-1} \text{ cm}^{-2}$ (green lines), corresponding to on-axis sources. The continuous lines correspond to a peak luminosity probability distribution with $L_* = 10^{51} \text{ erg/s}$ and $\Delta_1 = 100$, and the dashed line to $L_* = 5 \times 10^{50}$ and $\Delta_1 = 100$. For comparison, we have also indicated the efficiency for a larger value of the low luminosity bound ($L_* = 5 \times 10^{50}$ and $\Delta_1 = 30$) in dash-dotted blue. The efficiency is calculated for an FOV of 4π and a duty cycle of 100%, in order to have an efficiency of 1 at $z = 0$.

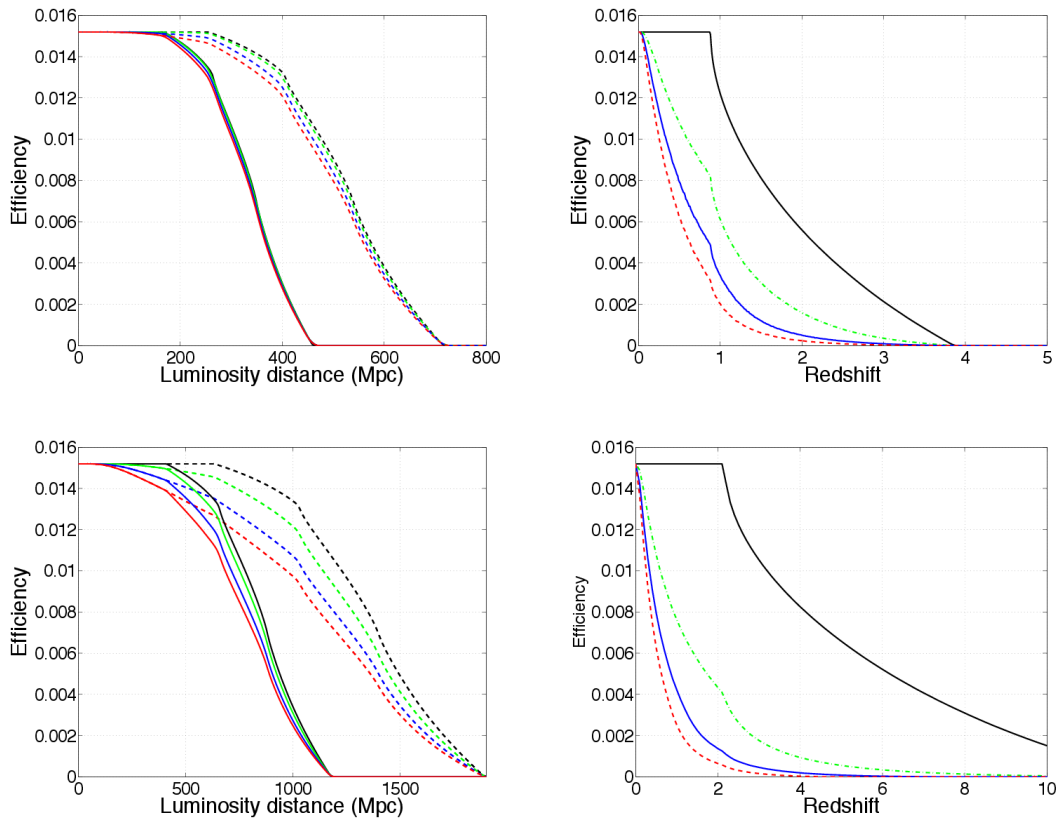


FIGURE 7.9: GW/GRB detection efficiency of BNS (left) and NSBH (right), for ALV (top) and ET (bottom), and the *Swift* satellite sensitivity with a flux limit of $1.5 \text{ ph s}^{-1} \text{ cm}^{-2}$ (continuous blue line) a pessimistic value of $2.5 \text{ ph s}^{-1} \text{ cm}^{-2}$ (dashed red line), corresponding to sGRBs with redshift measurement, and an optimal value of $0.56 \text{ ph s}^{-1} \text{ cm}^{-2}$ (dash-dotted green line), corresponding to on-axis sources. The black curve corresponds to the efficiency for an infinite sensitivity satellite and is shown for comparison. The efficiency is calculated for an FOV of 4π and a duty cycle of 100%.

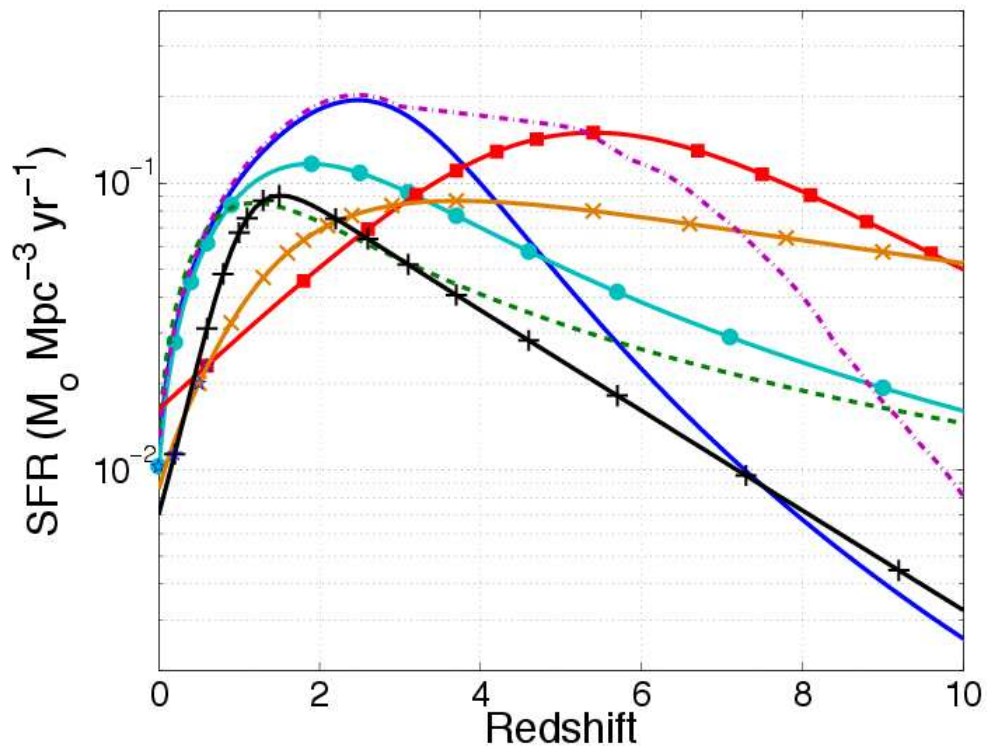


FIGURE 7.10: Cosmic star formation rates (in $M_{\odot} \text{ Mpc}^{-3} \text{ yr}^{-1}$) used in this paper: SFR of [110] (our reference model) in continuous blue, SFR of [197] with light blue dots, SFR of [198] in dashed green, SFR of [199] with red squares, SFR of [200] with orange crosses, SFR of [201] in dot-dashed purple, and the SFR of [202] in black with plus signs.

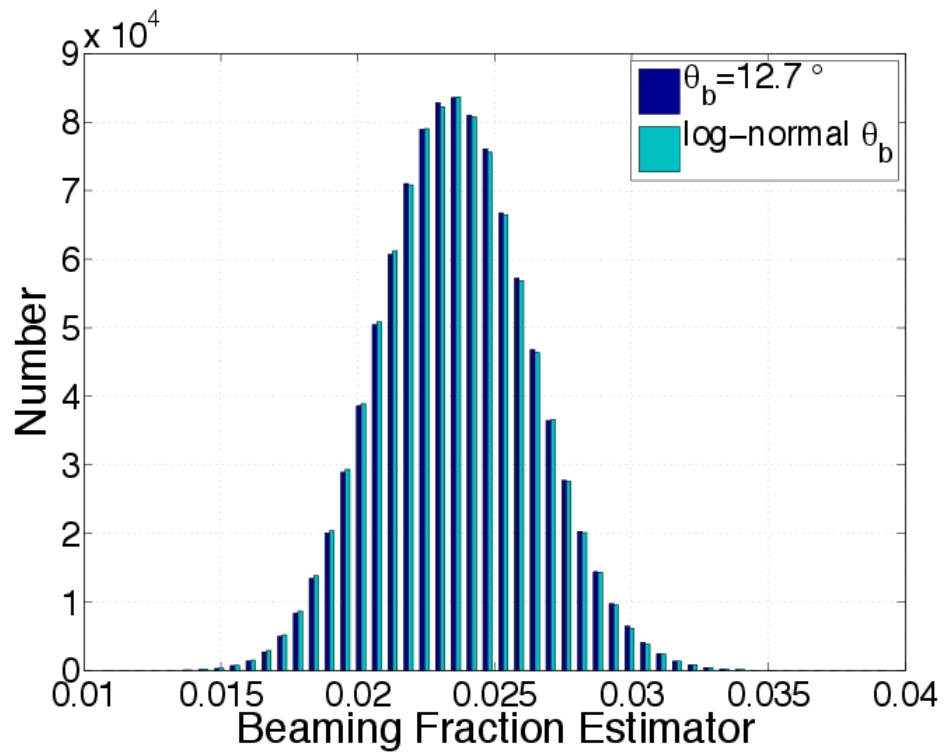


FIGURE 7.11: Histogram of $\hat{\Theta}_B$ from a sample of 10^5 simulations assuming one year of observation, for the log-normal distribution with average value $\mu_{\log \theta_B} = 2.0794$ and standard deviation $\sigma_{\log \theta_B} = 0.69$ (θ_B in degrees) [194] compared to a fixed beaming angle $\theta_B = 12.7^\circ$ giving the same average value of the beaming fraction Θ_B . Here we have assumed a GRB satellite with a FOV of 4π sr, duty cycle of 100% and infinite flux sensitivity.

Chapter 8

Conclusion

The next few years promise to be a very exciting period for gravitational wave physics, with operations of the advanced LIGO [15] detectors beginning in the summer of 2015 and advanced Virgo [16] expected to begin in the spring of 2016. It is hoped that we will make the first direct detection of a GW, originating from either the coalescence of a compact binary or from a burst with a electromagnetic counterpart, shortly after this, as the sensitivity of the detectors continue to be increased over a period of 5 years [104]. The detection of a stochastic gravitational-wave background signal may be achievable within the first few years of operations [80]. In Chapters 3 and 4, I present my work on an astrophysical SGWB, first investigating the statistical properties of a signal produced from the superposition of a large number of unresolvable BNS signals, and then conducting a mock data challenge to test the current analysis pipeline. In Chapters 5, ??, ?? and 6, I show my work as part of the second Einstein Telescope mock data and science challenge that covers the analysis, parameter estimation and application to cosmological measurements, of compact binary coalescence objects and the analysis of an astrophysical stochastic gravitational-wave background. Finally, in Chapter 7, I present an investigation on estimating the expected rate of coincident GWs and sGRBs with both the advanced and third generation of GW detectors.

In Chapter 3 it was shown that considering a stochastic gravitational-wave background constructed from a discrete set of individual GW signals results in a stochastic gravitational-wave background signal that is not isotropic or Gaussian, which are the assumptions that are usually made. However, in order to produce a signal that will be detectable with the advanced detectors, a large enough number of signals need to be considered which produces a stochastic gravitational-wave background that can be treated as isotropic and Gaussian as no bias will be introduced in the analysis. It was also derived that the continuity, or Gaussianity, of the signal should not affect the performance of the standard cross-correlation analysis, all that we need to consider is the total number of GW events, with their respective signal amplitudes, that occur within the observation time [62].

In Chapter 4 we conduct a full mock data and science challenge, investigating the analysis of multiple mock data sets constructed from different populations of CBC events. This consists of several, year-long, data sets, into which populations of BNS and/or BBH signals are injected with high predicted rates [79], along with an observing scenario data set [104], that accounts for

the continuous upgrading of the detectors over a 5.5 year period. For each data set we are able to recover the true amplitude of Ω_{gw} to within 2σ , when using both Gaussian noise and re-coloured initial detector noise. We also perform parameter estimation to recover the parameters for the injected population [119]. Finally, we confirm the theoretical findings of Chapter 3 [62], that the continuity, or Gaussianity, of the signal does not affect the performance of the analysis.

In Chapter 5 we detail the work carried out as part of the second Einstein Telescope mock data and science challenge with a focus on the production and analysis of the mock data. Here we detail the methods by which we produce the mock data, including the use of the population synthesis code, *StarTrack* [111, 112, 123, 124] and then present the results from analysing it with a new, low-latency, analysis pipeline, *gstlal* [125–128]. We show that we are able to analyse data using template waveforms starting from 5Hz, and find that we are able to detect multiple populations of CBC signals that are injected into the data. We are also able to recover the injected signal mass parameters with an accuracy that is a factor of 10 better than what was achieved in the first ET MDSC [18].

In Chapter 6 we present the results from analysing the ET mock data with a cross-correlation pipeline to measure the amplitude of Ω_{gw} . This involves first removing all theoretically detectable signals, which results in the breaking of the source isotropy due to only having one detector location. Because of this a bias is introduced to the analysis which is corrected for by applying the work carried out in Chapter 3. Using this correction we are able to measure Ω_{gw} with an accuracy of 1% [103].

In Chapter 7 we show our work on estimating the expected rate of coincident GW-sGRB detections we'd expect to make with both the second and third generation of GW detectors. For the second generation of detectors, which are about to begin operations, this rate is very small, on the order of a few per 10 years to 1000 years, depending on the size of the opening angle and rate of coalescence. With a third generation detector, such as ET, this rate increases significantly to a few to tens of thousands per year, again depending on the beam opening angle and rate of events. Due to the increased sensitivity of a detector such as ET, the limiting factor is not the detection of the GW signal but of the EM counterpart instead. We also present a method to determine the average size of the opening angle by considering the ratio of detections made in coincidence to the total number of GW detections, accounting for factors such as duty cycle [105].

Work should continue in both of the areas discussed above by conducting more mock data and science challenges with increasing degrees of complexity and sophistication. These will further test our current data analysis pipelines, preparing us for cases that deviate from the simpler models that have already been covered here. This will also help validate a potential detection that we make with the advanced detectors within the next few years and will also highlight any potential areas that would require further development for future generations of gravitational-wave detectors.

Appendix A

Einstein Telescope pre-site selection detector locations technical document

LIGO DCC: *T1400308*

A.1 Introduction

This document describes the calculations made to determine the exact detector locations for the Einstein Telescope (ET) [17, 51, 52], a planned third generation gravitational wave detector. At the time of writing the site location of ET has not yet been determined so in order to be able to run mock data science challenges we have assumed that ET will be placed at Cascina, Italy on the same site as Virgo.

A.2 Detector locations

Starting with the Virgo locations and arm vectors:

```
% Virgo

% Virgo vertex location
V0 = [4.54637409900e+06 8.42989697626e+05 4.37857696241e+06];
% Arm 1 vector
VArm1 = [-0.70045821479; 0.20848948619; 0.68256166277];
% Arm 2 vector
VArm2 = [-0.05379255368; -0.96908180549; 0.24080451708];

% Virgo arm length (m)
VArmL = 3000;

% Virgo arm 1 end station location
```

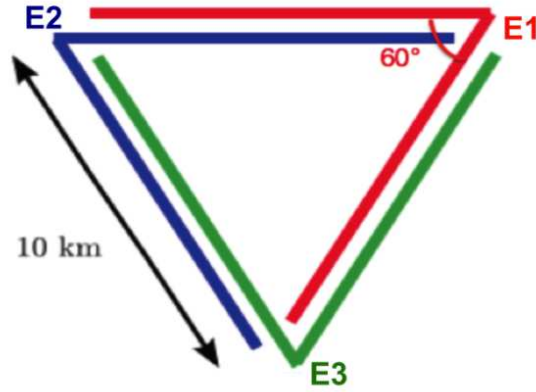


FIGURE A.1: Schematic configuration of the planned GW detector Einstein Telescope.

```
V1(1) = V0(1) + (VArmL * VArm1(1));
V1(2) = V0(2) + (VArmL * VArm1(2));
V1(3) = V0(3) + (VArmL * VArm1(3));
```

```
% Virgo arm 2 end station location
V2(1) = V0(1) + (VArmL * VArm2(1));
V2(2) = V0(2) + (VArmL * VArm2(2));
V2(3) = V0(3) + (VArmL * VArm2(3));
```

We place the central station of E1 at the exact location of the central station of Virgo and aligned it so that the first arms have the same vector. Using this vector we calculate the location of the E2 station using arm lengths of 10km. A diagram of the ET detector configuration is shown in Fig. A.1.

```
% ET

% E1 vertex location (same as Virgo)
E1 = [V0(1) V0(2) V0(3)];
%E1 = [4.54637409900e+06 8.42989697626e+05 4.37857696241e+06];

% E1 arm 1 vector (same as Virgo)
E1Arm1 = VArm1;
%E1Arm1 = [-0.70045821479; 0.20848948619; 0.68256166277];

% ET arm length (m)
ETArmL = 10000;

% E2 vertex location
E2(1) = E1(1) + (ETArmL * E1Arm1(1));
E2(2) = E1(2) + (ETArmL * E1Arm1(2));
E2(3) = E1(3) + (ETArmL * E1Arm1(3));
```

In order to calculate the position of E3 we first calculate the normal to the Virgo/ET plane and then perform a matrix rotation, R , on the E1 arm 1 vector to obtain the E1 arm 2 vector, where

$$R = \begin{bmatrix} \cos\theta + u_x^2(1 - \cos\theta) & u_x u_y(1 - \cos\theta) - u_z \sin\theta & u_x u_z(1 - \cos\theta) + u_y \sin\theta \\ u_y u_x(1 - \cos\theta) + u_z \sin\theta & \cos\theta + u_y^2(1 - \cos\theta) & u_y u_z(1 - \cos\theta) - u_x \sin\theta \\ u_z u_x(1 - \cos\theta) - u_y \sin\theta & u_z u_y(1 - \cos\theta) + u_x \sin\theta & \cos\theta + u_z^2(1 - \cos\theta) \end{bmatrix}, \quad (\text{A.1})$$

and u_i is the vector of the normal to the Virgo/ET plane with $i = x, y, z$. As is shown in Fig. A.1, the angle between the two arms of each detector is 60° .

```
% Normal to Virgo's plane
EinormVec = cross(VArm1, VArm2);

ux = EinormVec(1);
uy = EinormVec(2);
uz = EinormVec(3);

% Plot normal to Virgo-ET plane
Einorm(1) = E1(1) + (1000 * EinormVec(1));
Einorm(2) = E1(2) + (1000 * EinormVec(2));
Einorm(3) = E1(3) + (1000 * EinormVec(3));
%plot3([0 Einorm(1)], [0 Einorm(2)], [0 Einorm(3)], 'b')
plot3([E1(1) Einorm(1)], [E1(2) Einorm(2)], [E1(3) Einorm(3)], '--r', 'LineWidth', 2)

% Calculating rotation matrix for EC
theta = 60;
cosT = cosd(theta);
sinT = sind(theta);

RE1 = [(cosT + ux^2*(1-cosT)) (ux*uy*(1-cosT) - uz*sinT) (ux*uz*(1-cosT) + uy*sinT) ;
        (ux*uy*(1-cosT) + uz*sinT) (cosT + uy^2*(1-cosT)) (uy*uz*(1-cosT) - ux*sinT) ;
        (ux*uz*(1-cosT) - uy*sinT) (uy*uz*(1-cosT) + ux*sinT) (cosT + uz^2*(1-cosT))];

% Apply rotational matrix to E1 arm 1 vector
E1Arm2 = RE1 * E1Arm1;

% E3 vertex location
E3(1) = E1(1) + (ETArmL * E1Arm2(1));
E3(2) = E1(2) + (ETArmL * E1Arm2(2));
E3(3) = E1(3) + (ETArmL * E1Arm2(3));
```

This results in the Cartesian coordinates for each of the three detector sites. We now calculate the arm vectors for both E2 and E3. This is done by simple combinations of the existing arm vectors.

```
% E2 arm vectors
E2Arm1 = -E1Arm1 + E1Arm2;
E2Arm2 = -E1Arm1;

% E3 arm vectors
E3Arm1 = -E1Arm2;
E3Arm2 = -E2Arm1;
```

We next calculate the distance between the Earth centred origin and the E2 and E3 detector locations. With this we can determine the elevations above sea level.

```
% Distance from origin to each detector in meters
E1r = sqrt(E1(1)^2 + E1(2)^2 + E1(3)^2);
E2r = sqrt(E2(1)^2 + E2(2)^2 + E2(3)^2);
E3r = sqrt(E3(1)^2 + E3(2)^2 + E3(3)^2);
```

TABLE A.1: Table of ET detector locations in Earth-centred Cartesian and geodetic coordinates with arm vectors in Earth-centred Cartesian coordinates.

ET 1			
Cartesian (m)	Geodetic	Arm 1 vector	Arm 2 Vector
$x = 4.54637409900 \times 10^6$	Lat = 43.63141444700387	-0.70045821479	-0.39681482542
$y = 8.42989697626 \times 10^5$	Long = 10.5044966111129	0.20848948619	-0.73500471881
$z = 4.37857696241 \times 10^6$	Height (m) = 51.884	0.68256166277	0.54982366052
ET 2			
Cartesian (m)	Geodetic	Arm 1 vector	Arm 2 Vector
$x = 4.53936951685 \times 10^6$	Lat = 43.7162832762563	0.30364338937	0.70045821479
$y = 8.45074592488 \times 10^5$	Long = 10.5457803157726	-0.94349420500	-0.20848948619
$z = 4.38540257904 \times 10^6$	Height (m) = 59.735	-0.13273800225	-0.68256166277
ET 3			
Cartesian (m)	Geodetic	Arm 1 vector	Arm 2 Vector
$x = 4.54240595075 \times 10^6$	Lat = 43.6997564614835	0.39681482542	-0.30364338937
$y = 8.35639650438 \times 10^5$	Long = 10.4238192933064	0.73500471881	0.94349420500
$z = 4.38407519902 \times 10^6$	Height (m) = 59.727	-0.54982366052	0.13273800225

```

% Difference in distance from origin.
E2alt = E2r - E1r;
E3alt = E3r - E1r;
    
```

This assumes that the Earth is spherical and not an oblate ellipsoid.

A.2.1 Results

Finally on order to obtain the longitude, latitude and geodetic height we use the calculator provided at the following site: <http://www.apsalin.com/convert-cartesian-to-geodetic.aspx>.

A.3 Null stream

We now deal with the *null stream*. The null stream is the sum of the three detector streams which results in the removal of GW signals due to the fact that the ET interferometers forms a closed path. For use in data analysis we have placed the theoretical null stream location in the same plane as ET at the centre of the triangle.

```

% Null stream (located on same plane at centre of ET)

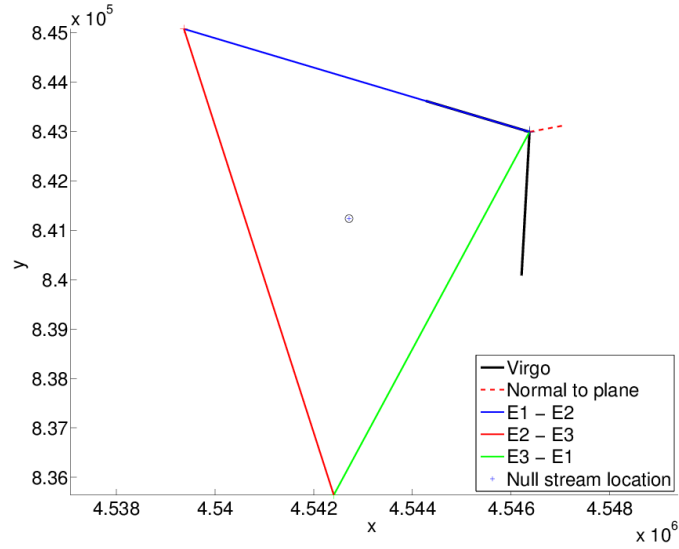
% Calculating rotation matrix
theta2 = 30;
cosT2 = cosd(theta2);
sinT2 = sind(theta2);

RE2 = [(cosT2 + ux^2*(1-cosT2)) (ux*uy*(1-cosT2) - uz*sinT2) (ux*uz*(1-cosT2) + uy*sinT2) ;
        (ux*uy*(1-cosT2) + uz*sinT2) (cosT2 + uy^2*(1-cosT2)) (uy*uz*(1-cosT2) - ux*sinT2) ;
        (ux*uz*(1-cosT2) - uy*sinT2) (uy*uz*(1-cosT2) + ux*sinT2) (cosT2 + uz^2*(1-cosT2))];

% Apply rotational matrix to E1 arm 1 vector
    
```

TABLE A.2: Table of ET *null stream* (theoretical) location in Earth-centred Cartesian and geodetic coordinates

ET <i>null stream</i>	
Cartesian (m)	Geodetic
$x = 4.54271652220 \times 10^6$	Lat = 43.6824960936215
$y = 8.41234646851 \times 10^5$	Long = 10.4913653894584
$z = 4.38268491349 \times 10^6$	Height (m) = 54.502


 FIGURE A.2: Schematic of the Einstein Telescope detector locations in Cartesian Earth centred coordinates. This figure shows the detectors in the $x - y$ plane.

```

E1toE0 = RE2 * E1Arm1;

E0dist1 = 5000 / cosd(theta2);

% EN position
E0(1) = E1(1) + (E0dist1 * E1toE0(1));
E0(2) = E1(2) + (E0dist1 * E1toE0(2));
E0(3) = E1(3) + (E0dist1 * E1toE0(3));
    
```

Finally we perform some checks to ensure that the null stream is located the same distance from each of the ET detectors.

```

% Check distance from center to EB and EC

dE02 = E0 - E2;
dE03 = E0 - E3;

E0dist2 = sqrt(dE02(1)^2 + dE02(2)^2 + dE02(3)^2);
E0dist3 = sqrt(dE03(1)^2 + dE03(2)^2 + dE03(3)^2);

fprintf('Distance check = \n')
distCheck = [E0dist1; E0dist2; E0dist3];
disp(distCheck)

% Check angles
    
```

```
CosTheta1 = dot(E1normVec, E1Arm1)/(norm(E1normVec)*norm(E1Arm1));  
ThetaInDegrees1 = acos(CosTheta1)*180/pi;
```

```
CosTheta2 = dot(E1normVec, E1Arm2)/(norm(E1normVec)*norm(E1Arm2));  
ThetaInDegrees2 = acos(CosTheta2)*180/pi;
```

```
CosTheta3 = dot(E1normVec, E1toE0)/(norm(E1normVec)*norm(E1toE0));  
ThetaInDegrees3 = acos(CosTheta3)*180/pi;
```

```
CosTheta4 = dot(E1normVec, VArm1)/(norm(E1normVec)*norm(VArm1));  
ThetaInDegrees4 = acos(CosTheta4)*180/pi;
```

```
CosTheta5 = dot(E1normVec, VArm2)/(norm(E1normVec)*norm(VArm2));  
ThetaInDegrees5 = acos(CosTheta5)*180/pi;
```

Bibliography

- [1] I. Newton, *Philosophiæ Naturalis Principia Mathematica* (Londini, Jussu Societatis Regiæ ac Typis Josephi Streater. Prostat apud plures Bibliopolas, Anno MDCLXXXVII, 1687).
- [2] J. Kepler, *Astronomia Nova AITIOΛOΓHTOΣ seu physica coelestis, tradita commentariis de motibus stellae Martis ex observationibus G.V. Tychonis Brahe* (Heidelberg: G. Voegelinus, 1609).
- [3] J. Kepler, *Harmonices Mundi* (Lincii Austriae : sumptibus Godofredi Tampachii ..., ex-cudebat Ioannes Plancus, 1619).
- [4] A. Einstein, Sitzungsberichte der Königlich Preussischen Akademie der Wissenschaften (Berlin) **1915 (part 2)**, 778–786, 799–801 (1915).
- [5] A. Einstein, *Annalen der Physik* **49**, 769 (1916).
- [6] A. Einstein, Sitzungsberichte der Königlich Preussischen Akademie der Wissenschaften (Berlin) **1915 (part 2)**, 844 (1915).
- [7] A. Einstein, Sitzungsberichte der Königlich Preussischen Akademie der Wissenschaften (Berlin) **1918 (part 1)**, 154–167 (1918).
- [8] R. A. Hulse and J. H. Taylor, *Astrophys. J.* **195**, L51 (1975).
- [9] J. M. Weisberg and J. H. Taylor, *Astrophys. J.* **576**, 942 (2002).
- [10] J. Weber, *Phys. Rev.* **117**, 306 (1960).
- [11] B. P. Abbott et al. (LIGO Scientific Collaboration), *Rep. Prog. Phys.* **72**, 076901 (2009).
- [12] F. Acernese et al. (Virgo Collaboration), *AIP Conf. Proc.* **794**, 307 (2005).
- [13] B. Willke et al. (LIGO Scientific Collaboration), *Class. Quantum Grav.* **24**, S389 (2007).
- [14] R. Takahashi et al. (TAMA Collaboration), *Class. Quantum Grav.* **21**, S403 (2004).
- [15] J. Aasi et al. (LIGO Scientific Collaboration), *Class. Quantum Grav.* **32**, 074001 (2015).
- [16] F. Acernese et al. (Virgo Collaboration), *Class. Quantum Grav.* **32**, 024001 (2015).
- [17] M. Punturo et al., *Class. Quantum Grav.* **27**, 194002 (2010).

-
- [18] T. Regimbau, T. Dent, W. Del Pozzo, S. Giampanis, T. G. F. Li, C. Robinson, C. Van Den Broeck, D. Meacher, C. Rodriguez, B. S. Sathyaprakash, et al., *Phys. Rev. D* **86**, 122001 (2012).
- [19] C. W. Misner, K. S. Thorne, and J. A. Wheeler, *Gravitation* (W. H. Freeman, 1973).
- [20] R. M. Wald, *General Relativity* (University Of Chicago Press, 1984).
- [21] S. M. Carroll, *Spacetime and Geometry: An Introduction to General Relativity* (Addison-Wesley, 2003).
- [22] J. B. Hartle, *Gravity: An Introduction to Einstein's General Relativity* (Addison-Wesley, 2003).
- [23] M. Maggiore, *Gravitational Waves: Volume 1: Theory and Experiments* (Oxford University Press, 2007).
- [24] B. Schutz, *A First Course in General Relativity* (Cambridge University Press, 2009).
- [25] J. D. E. Creighton and W. G. Anderson, *Gravitational-Wave Physics and Astronomy: An Introduction to Theory, Experiment and Data Analysis* (Wiley-VCH, 2011).
- [26] A. Ashtekar, B. Berger, J. Isenberg, and M. MacCallum, *General Relativity and Gravitation: A Centennial Perspective* (Cambridge University Press, 2015).
- [27] *Introduction to LIGO and gravitational waves*, <http://www.ligo.org/science.php>, accessed: 2015-06-15.
- [28] B. Allen and J. D. Romano, *Phys. Rev. D* **59**, 102001 (1999).
- [29] M. Maggiore, *Physics Reports* **331**, 283 (2000).
- [30] L. P. Grishchuk, *Sov. Phys. JETP* **40**, 409 (1975).
- [31] A. A. Starobinskiĭ, *JETP Lett.* **30**, 682 (1979).
- [32] R. Easther and E. A. Lim, *Journal of Cosmology and Astroparticle Physics* **2006**, 010 (2006).
- [33] N. Barnaby, E. Pajer, and M. Peloso, *Phys. Rev. D* **85**, 023525 (2012).
- [34] R. R. Caldwell and B. Allen, *Phys. Rev. D* **45**, 3447 (1992).
- [35] T. Damour and A. Vilenkin, *Phys. Rev. Lett.* **85**, 3761 (2000).
- [36] T. Damour and A. Vilenkin, *Phys. Rev. D* **71**, 063510 (2005).
- [37] X. Siemens, V. Mandic, and J. Creighton, *Phys. Rev. Lett.* **98**, 111101 (2007).
- [38] S. Ölmez, V. Mandic, and X. Siemens, *Phys. Rev. D* **81**, 104028 (2010).
- [39] S. Ölmez, V. Mandic, and X. Siemens, *Journal of Cosmology and Astroparticle Physics* **2012**, 009 (2012).
- [40] P. Sandick, K. A. Olive, F. Daigne, and E. Vangioni, *Phys. Rev. D* **73**, 104024 (2006).

-
- [41] E. Howell, D. Coward, R. Burman, D. Blair, and J. Gilmore, *MNRAS* **351**, 1237 (2004).
- [42] A. Buonanno, G. Sigl, G. G. Raffelt, H. T. Janka, and E. Müller, *Phys. Rev. D* **72**, 084001 (2005).
- [43] S. Marassi, R. Schneider, and V. Ferrari, *MNRAS* **398**, 293 (2009).
- [44] A. J. Farmer and E. S. Phinney, *MNRAS* **346**, 1197 (2003).
- [45] E. S. Phinney, *Astrophys. J. Lett.* **380**, L17 (1991).
- [46] D. I. Kosenko and K. A. Postnov, *Astron. & Astrophys.* **336**, 786 (1998).
- [47] X. J. Zhu, E. Howell, T. Regimbau, D. Blair, and Z. H. Zhu, *Astrophys. J.* **739**, 86 (2011).
- [48] C. Wu, V. Mandic, and T. Regimbau, *Phys. Rev. D* **85**, 104024 (2012).
- [49] T. Regimbau and J. A. de Freitas Pacheco, *Astrophys. J.* **642**, 455 (2006).
- [50] J. Aasi et al. (LIGO Scientific Collaboration and Virgo Collaboration), *Astrophys. J.* **785**, 119 (2014).
- [51] A. Freise, S. Chelkowski, S. Hild, W. Del Pozzo, A. Perreca, and A. Vecchio, *Class. Quantum Grav.* **26**, 085012 (2009).
- [52] M. Punturo and K. Somiya, *Int. J. Mod. Phys. D* **22**, 1330010 (2013).
- [53] B. P. Abbott et al. (LIGO Scientific Collaboration), *Phys. Rev. D* **79**, 122001 (2009).
- [54] B. P. Abbott et al. (LIGO Scientific Collaboration), *Phys. Rev. D* **80**, 047101 (2009).
- [55] J. Abadie et al. (LIGO Scientific Collaboration and Virgo Collaboration), *Phys. Rev. D* **82**, 102001 (2010).
- [56] J. Abadie et al. (LIGO Scientific Collaboration and Virgo Collaboration), *Phys. Rev. D* **85**, 082002 (2012).
- [57] B. Sathyaprakash and B. F. Schutz, *Living Rev. Relativity* **12**, 2 (2009).
- [58] B. P. Abbott et al. (LIGO Scientific Collaboration and Virgo Collaboration), *Nature* **460**, 990 (2009).
- [59] J. Aasi et al. (LIGO Scientific Collaboration and Virgo Collaboration), *Phys. Rev. Lett.* **113**, 231101 (2014).
- [60] N. Christensen, *Phys. Rev. D* **46**, 5250 (1992).
- [61] B. Allen, in *Relativistic Gravitation and Gravitational Radiation*, edited by J. A. Marck and J. P. Lasota (1997), p. 373.
- [62] D. Meacher, E. Thrane, and T. Regimbau, *Phys. Rev. D* **89**, 084063 (2014).
- [63] C. Cutler, *Phys. Rev. D* **66**, 084025 (2002).
- [64] T. Regimbau and V. Mandic, *Class. Quantum Grav.* **25**, 184018 (2008).

-
- [65] P. A. Rosado, *Phys. Rev. D* **86**, 104007 (2012).
- [66] E. Howell, T. Regimbau, A. Corsi, D. Coward, and R. Burman, *MNRAS* **410**, 2123 (2011).
- [67] S. Marassi, R. Ciolfi, R. Schneider, L. Stella, and V. Ferrari, *MNRAS* **411**, 2549 (2011).
- [68] T. Regimbau and J. A. de Freitas Pacheco, *Astron. & Astrophys.* **376**, 381 (2001).
- [69] B. J. Owen, L. Lindblom, C. Cutler, B. F. Schutz, A. Vecchio, and N. Andersson, *Phys. Rev. D* **58**, 084020 (1998).
- [70] J. L. Houser, J. M. Centrella, and S. C. Smith, *Phys. Rev. Lett.* **72**, 1314 (1994).
- [71] D. Lai and S. L. Shapiro, *Astrophys. J.* **442**, 259 (1995).
- [72] J. S. B. Wyithe and A. Loeb, *Astrophys. J.* **590**, 691 (2003).
- [73] A. H. Jaffe and D. C. Backer, *Astrophys. J.* **583**, 616 (2003).
- [74] M. Enoki, K. T. Inoue, M. Nagashima, and N. Sugiyama, *Astrophys. J.* **615**, 19 (2004).
- [75] E. Thrane, S. Ballmer, J. D. Romano, S. Mitra, D. Talukder, S. Bose, and V. Mandic, *Phys. Rev. D* **80**, 122002 (2009).
- [76] J. Abadie et al. (LIGO Scientific Collaboration and Virgo Collaboration), *Phys. Rev. Lett.* **107**, 271102 (2011).
- [77] E. Thrane and J. D. Romano, *Phys. Rev. D* **88**, 124032 (2013).
- [78] F. Özel, D. Psaltis, R. Narayan, and A. S. Villarreal, *Astrophys. J.* **757**, 55 (2012).
- [79] J. Abadie et al. (LIGO Scientific Collaboration and Virgo Collaboration), *Class. Quantum Grav.* **27**, 173001 (2010).
- [80] D. Meacher, M. Coughlin, S. Morris, T. Regimbau, N. Christensen, S. Kandhasamy, V. Mandic, J. D. Romano, and E. Thrane, *Phys. Rev. D* **92**, 063002 (2015).
- [81] L. P. Grishchuk, *Phys. Rev. D* **48**, 3513 (1993).
- [82] M. Gasperini and G. Veneziano, *Astropart. Phys.* **1**, 317 (1993).
- [83] A. Buonanno, M. Maggiore, and C. Ungarelli, *Phys. Rev. D* **55**, 3330 (1997).
- [84] J. F. Dufaux, D. G. Figueroa, and J. García-Bellido, *Phys. Rev. D* **82**, 083518 (2010).
- [85] T. Regimbau, S. Giampanis, X. Siemens, and V. Mandic, *Phys. Rev. D* **85**, 066001 (2012).
- [86] C. Caprini, R. Durrer, and G. Servant, *Phys. Rev. D* **77**, 124015 (2008).
- [87] C. Caprini, R. Durrer, T. Konstandin, and G. Servant, *Phys. Rev. D* **79**, 083519 (2009).
- [88] C. Caprini, R. Durrer, and G. Servant, *Journal of Cosmology and Astroparticle Physics* **12**, 024 (2009).
- [89] P. Binétruy, A. Bohé, C. Caprini, and J.-F. Dufaux, *Journal of Cosmology and Astroparticle Physics* **6**, 27 (2012).

-
- [90] T. Regimbau, *Res. Astron. Astrophys.* **11**, 369 (2011).
- [91] X. J. Zhu, E. Howell, and D. Blair, *MNRASL* **409**, L132 (2010).
- [92] T. Regimbau and J. A. de Freitas Pacheco, *Astron. & Astrophys.* **447**, 1 (2006).
- [93] C. J. Wu, V. Mandic, and T. Regimbau, *Phys. Rev. D* **87**, 042002 (2013).
- [94] J. C. N. de Araujo and G. F. Marranghello, *General Relativity and Gravitation* **41**, 1389 (2009).
- [95] V. Ferrari, S. Matarrese, and R. Schneider, *MNRAS* **303**, 258 (1999).
- [96] X. J. Zhu, X. L. Fan, and Z. H. Zhu, *Astrophys. J.* **729**, 59 (2011).
- [97] P. A. Rosado, *Phys. Rev. D* **84**, 084004 (2011).
- [98] S. Marassi, R. Schneider, G. Corvino, V. Ferrari, and S. P. Zwart, *Phys. Rev. D* **84**, 124037 (2011).
- [99] X.-J. Zhu, E. J. Howell, D. G. Blair, and Z.-H. Zhu, *MNRAS* **431**, 882 (2013).
- [100] T. Regimbau and S. A. Hughes, *Phys. Rev. D* **79**, 062002 (2009).
- [101] I. Kowalska, T. Regimbau, T. Bulik, M. Dominik, and K. Belczynski, *Astron. & Astrophys.* **574**, A58 (2015).
- [102] V. Mandic, E. Thrane, S. Giampanis, and T. Regimbau, *Phys. Rev. Lett.* **109**, 171102 (2012).
- [103] T. Regimbau, D. Meacher, and M. Coughlin, *Phys. Rev. D* **89**, 084046 (2014).
- [104] J. Aasi et al. (LIGO Scientific Collaboration and Virgo Collaboration), *arXiv* **1304**, 0670 (2013).
- [105] T. Regimbau, K. Siellez, D. Meacher, B. Gendre, and M. Böer, *Astrophys. J.* **799**, 69 (2015).
- [106] K. Belczynski, R. Perna, T. Bulik, V. Kalogera, N. Ivanova, and D. Q. Lamb, *Astrophys. J.* **648**, 1110 (2006).
- [107] E. Berger and other, *Astrophys. J.* **664**, 1000 (2007).
- [108] K. Belczynski and V. Kalogera, *Astrophys. J. Lett.* **550**, L183 (2001).
- [109] T. Bulik, K. Belczynski, and B. Rudak, *Astron. & Astrophys.* **415**, 407 (2004).
- [110] A. M. Hopkins and J. F. Beacom, *Astrophys. J.* **651**, 142 (2006).
- [111] K. Belczynski, V. Kalogera, F. A. Rasio, R. E. Taam, A. Zezas, T. Bulik, T. J. Maccarone, and N. Ivanova, *Astrophys. J. Suppl.* **174**, 223 (2008).
- [112] M. Dominik, K. Belczynski, C. Fryer, D. E. Holz, E. Berti, T. Bulik, I. Mandel, and R. O’Shaughnessy, *Astrophys. J.* **759**, 52 (2012).

-
- [113] S. Osłowski, T. Bulik, D. Gondek-Rosinska, and K. Belczynski, *MNRAS* **413**, 461 (2011).
- [114] P. Ajith et al., *Phys. Rev. D* **77**, 104017 (2008).
- [115] A. Buonanno, B. R. Iyer, E. Ochsner, Y. Pan, and B. S. Sathyaprakash, *Phys. Rev. D* **80**, 084043 (2009).
- [116] E. Thrane, N. Christensen, and R. M. S. Schofield, *Phys. Rev. D* **87**, 123009 (2013).
- [117] E. Thrane, N. Christensen, R. M. S. Schofield, and A. Effler, *Phys. Rev. D* **90**, 023013 (2014).
- [118] D. Coward and T. Regimbau, *New Astron. Rev.* **50**, 461 (2006).
- [119] J. Abadie et al. (LIGO Scientific Collaboration and Virgo Collaboration), *Phys. Rev. D* **85**, 122001 (2012).
- [120] E. Thrane, *Phys. Rev. D* **87**, 043009 (2013).
- [121] B. S. Sathyaprakash et al., *Class. Quantum Grav.* **29**, 124013 (2012).
- [122] J. R. Gair, I. Mandel, M. C. Miller, and M. Volonteri, *Gen.Relativ. Gravit.* **43**, 485 (2011).
- [123] K. Belczynski, V. Kalogera, and T. Bulik, *Astrophys. J.* **572**, 407 (2002).
- [124] K. Belczynski, M. Dominik, T. Bulik, R. O’Shaughnessy, C. Fryer, and D. E. Holz, *Astrophys. J. Lett.* **715**, L138 (2010).
- [125] K. Cannon, A. Chapman, C. Hanna, D. Keppel, A. C. Searle, and A. Weinstein, *Phys. Rev. D* **82**, 044025 (2010).
- [126] K. Cannon, C. Hanna, D. Keppel, and A. C. Searle, *Phys. Rev. D* **83**, 084053 (2011).
- [127] K. Cannon et al., *Astrophys. J.* **748**, 136 (2012).
- [128] K. Cannon, C. Hanna, and D. Keppel, *Phys. Rev. D* **88**, 024025 (2013).
- [129] L. Blanchet, *Living Rev. Relativity* **17**, 2 (2014).
- [130] D. A. Brown, P. Kumar, and A. H. Nitz, *Phys. Rev. D* **87**, 082004 (2013).
- [131] T. Damour, B. R. Iyer, and B. S. Sathyaprakash, *Phys. Rev. D* **62**, 084036 (2000).
- [132] P. D. Welch, *IEEE Trans. Audio Electroacoust* **15**, 70 (1967).
- [133] B. Allen, W. G. Anderson, P. R. Brady, D. A. Brown, and J. D. E. Creighton, *Phys. Rev. D* **85**, 122006 (2012).
- [134] P. R. Brady and S. Fairhurst, *Class. Quantum Grav.* **25**, 105002 (2008).
- [135] C. Van Den Broeck, *J. Phys.: Conf. Ser.* **484**, 012008 (2014).
- [136] J. Aasi et al. (LIGO Scientific Collaboration and Virgo Collaboration), *Phys. Rev. D* **88**, 102002 (2013).

- [137] J. Aasi et al. (LIGO Scientific Collaboration and Virgo Collaboration), *Phys. Rev. D* **90**, 062010 (2014).
- [138] J. Aasi et al. (LIGO Scientific Collaboration and Virgo Collaboration), *Phys. Rev. Lett.* **112**, 131101 (2014).
- [139] A. Buonanno, Y. Chen, Y. Pan, H. Tagoshi, and M. Vallisneri, *Phys. Rev. D* **72**, 084027 (05).
- [140] A. Buonanno, Y. Chen, and M. Vallisneri, *Phys. Rev. D* **67**, 104025 (2006).
- [141] A. Buonanno, Y. Chen, Y. Pan, and M. Vallisneri, *Phys. Rev. D* **74**, 029902 (2006).
- [142] Éanna É. Flanagan and T. Hinderer, *Phys. Rev. D* **77**, 021502 (2008).
- [143] J. S. Read, C. Markakis, M. Shibata, K. Uryu, J. D. E. Creighton, and J. L. Friedman, *Phys. Rev. D* **79**, 124033 (2009).
- [144] T. Hinderer, B. D. Lackey, R. N. Lang, and J. S. Read, *Phys. Rev. D* **81**, 123016 (2010).
- [145] F. Pannarale, L. Rezzolla, F. Ohme, and J. S. Read, *Phys. Rev. D* **84**, 104017 (2011).
- [146] M. Hannam, P. Schmidt, A. Bohé, L. Haegel, S. Husa, F. Ohme, G. Pratten, and M. Pürrer, *Phys. Rev. Lett.* **113**, 151101 (2014).
- [147] P. Schmidt, F. Ohme, and M. Hannam, *Phys. Rev. D* **91**, 024043 (2015).
- [148] B. Barr et al., LIGO DCC (2012), URL <https://dcc.ligo.org/LIGO-T1200046/public>.
- [149] S. Nissanke, D. E. Holz, S. A. Hughes, N. Dalal, and J. L. Sievers, *Astrophys. J.* **725**, 496 (2010).
- [150] W. D. Pozzo, *Phys. Rev. D* **86**, 043011 (2012).
- [151] S. R. Taylor and J. R. Gair, *Phys. Rev. D* **86**, 023502 (2012).
- [152] C. Messenger and J. Read, *Phys. Rev. Lett.* **108**, 091101 (2012).
- [153] S. Babak and others (Challenge-1B participants), *Class. Quantum Grav.* **25**, 184026 (2008).
- [154] N. F. Fotopoulos (LIGO Scientific Collaboration), *J. Phys.: Conf. Ser.* **122**, 012032 (2008).
- [155] E. E. Flanagan, *Phys. Rev. D* **48**, 2389 (1993).
- [156] D. Eichler, M. Livio, T. Piran, and D. N. Schramm, *Nature* **340**, 126 (1989).
- [157] E. Berger, *Annual Review of Astronomy and Astrophysics* **52**, 43 (2014).
- [158] L.-X. Li and B. Paczyński, *Astrophys. J. Lett.* **507**, L59 (1998).
- [159] S. Rosswog, *Astrophys. J.* **634**, 1202 (2005).
- [160] N. R. Tanvir, A. J. Levan, A. S. Fruchter, J. Hjorth, R. A. Hounsell, K. Wiersema, and R. L. Tunnicliffe, *Nature* **500**, 547 (2013).
- [161] E. Berger, W. Fong, and R. Chornock, *Astrophys. J. Lett.* **774**, L23 (2013).

- [162] V. V. Usov, *Astrophys. J.* **389**, 635 (1992).
- [163] B. Zhang, Y. Z. Fan, J. Dyks, S. Kobayashi, P. Meszaros, D. N. Burrows, J. A. Nousek, and N. Gehrels, *Astrophys. J.* **642**, 354 (2006).
- [164] A. Corsi and P. Mészáros, *Astrophys. J.* **702**, 1171 (2009).
- [165] B. Zhang, B. B. Zhang, F. J. Virgili, et al., *Astrophys. J.* **703**, 1696 (2009).
- [166] B. F. Schutz, *Nature (London)* **323**, 310 (1986).
- [167] N. Dalal, D. E. Holz, S. A. Hughes, and B. Jain, *Phys. Rev. D* **74**, 063006 (2006).
- [168] B. S. Sathyaprakash, B. F. Schutz, and C. Van Den Broeck, *Class. Quantum Grav.* **27**, 215006 (2010).
- [169] W. Zhao, C. V. D. Broeck, D. Baskaran, and T. G. F. Li, *Phys. Rev. D* **83**, 023005 (2011).
- [170] R. Salvaterra, M. Della Valle, S. Campana, et al., *Nature* **461**, 1258 (2009).
- [171] K. Siellez, M. Boër, and B. Gendre, *MNRAS* **437**, 649 (2013).
- [172] L. P. Singer, S. B. Cenko, M. M. Kasliwal, et al., *Astrophys. J. Lett.* **776**, L34 (2013).
- [173] J. Aasi, J. Abadie, B. P. Abbott, et al. (LIGO Scientific Collaboration and Virgo Collaboration), *Astrophys. J. Suppl.* **211**, 7 (2014).
- [174] N. Ivanova, C. O. Heinke, F. A. Rasio, K. Belczynsk, and J. M. Fregeau, *MNRAS* **386**, 553 (2008).
- [175] A. Sadowski, K. Belczynski, T. Bulik, N. Ivanova, F. Rasio, and R. O’Shaughnessy, *Astrophys. J.* **676**, 1162 (2008).
- [176] D. Wanderman and T. Piran, *MNRAS* **448**, 3026 (2015).
- [177] D. Guetta, T. Piran, and E. Waxman, *Astrophys. J.* **619**, 412 (2005).
- [178] D. Guetta and T. Piran, *Astron. & Astrophys.* **435**, 421 (2005).
- [179] C. Hopman, D. Guetta, E. Waxman, and S. Potegies Zwart, *Astrophys. J. Lett.* **643**, L91 (2006).
- [180] D. Guetta and S. L., *Astron. & Astrophys.* **498**, 329 (2009).
- [181] B. N. R., B. J. S., and P. D., *Astrophys. J.* **711**, 495 (2010).
- [182] E. J. Howell, D. M. Coward, G. Stratta, B. Gendre, and H. Zhou, *MNRAS* **444**, 14 (2014).
- [183] Z. B. Zhang, D. Y. Chen, and Y. F. Huang, *Astrophys. J.* **755**, 55 (2012).
- [184] S. Ghosh and S. Bose, *arxiv* **1308**, 6081 (2013).
- [185] A. M. Soderberg, E. Berger, M. Kasliwal, et al., *Astrophys. J.* **650**, 261 (2006).
- [186] W. Fong, E. Berger, Margutti, R., et al., *Astrophys. J.* **756**, 189 (2012).

-
- [187] A. Nicuesa Guelbenzu, S. Klose, A. Rossi, et al., *Astron. & Astrophys.* **531**, L6 (2011).
- [188] D. M. Coward, E. J. Howell, T. Piran, et al., *MNRAS* **425**, 2668 (2012).
- [189] D. B. Fox and P. & Mészáros, *New J. Phys.* **8**, 199 (2006).
- [190] D. Grupe, D. N. Burrows, S. K. Patel, et al., *Astrophys. J.* **653**, 462 (2006).
- [191] A. von Kienlin, C. Meegan, W. Paciesas, et al., *Astrophys. J. Suppl.* **211**, 13 (2014).
- [192] D. Band, J. Matteson, L. Ford, et al., *Astrophys. J.* **413**, 281 (1993).
- [193] L. Z. Kelley, I. Mandel, and E. Ramirez-Ruiz, *Phys. Rev. D* **87**, 123004 (2013).
- [194] A. Goldstein et al., arXiv **1101**, 2458 (2011).
- [195] A. Lien, T. Sakamoto, N. Gehrels, D. M. Palmer, S. D. Barthelmy, C. Graziani, and J. K. Cannizzo, *Astrophys. J.* **783**, 24 (2014).
- [196] J. Grindlay, S. Portegies Zwart, and S. McMillan, *Nature Physics* **2**, 116 (2006).
- [197] M. A. Fardal, N. Katz, D. H. Weinberg, and R. Davé, *MNRAS* **379**, 985 (2007).
- [198] S. M. Wilkins, N. Trentham, and A. M. Hopkins, *MNRAS* **385**, 687 (2008).
- [199] V. Springel and L. Hernquist, *MNRAS* **339**, 312 (2003).
- [200] K. Nagamine, J. P. Ostriker, M. Fukugita, and R. Cen, *Astrophys. J.* **653**, 881 (2006).
- [201] L. Tornatore, S. Borgani, K. Dolag, and F. Matteucci, *MNRAS* **382**, 1050 (2007).
- [202] P. Madau, L. Pozzetti, and M. Dickinson, *Astrophys. J.* **498**, 106 (1998).
- [203] L. S. Finn and D. F. Chernoff, *Phys. Rev. D* **47**, 2198 (1993).
- [204] M. Dominik, E. Berti, R. O’Shaughnessy, I. Mandel, K. Belczynski, C. Fryer, D. Holz, T. Bulik, and F. Pannarale, arXiv **1405**, 7016 (2014).
- [205] C. E. Petrillo, A. Dietz, and M. Cavaglia, *Astrophys. J.* **767**, 140 (2013).
- [206] H.-Y. Chen and D. E. Holz, *Phys. Rev. Lett.* **111**, 181101 (2013).
- [207] A. Dietz, *Astron. & Astrophys.* **529**, A97 (2011).